UNIVERSIDAD DE ANTIOQUIA

High Temperature Behavior of Calcium Aluminate Cement Pastes

John Fernando Zapata Mesa

Universidad de Antioquia

Facultad de Ingeniería, Doctorado en Ingeniería de Materiales

Medellín, Colombia

2020

High Temperature Behavior of Calcium Aluminate Cement Pastes

John Fernando Zapata Mesa

This thesis is presented as a partial requirement to apply for the title of Materials Engineering Doctor

Advisor

Dr. Henry Alonso Colorado Morales

Co - Advisor

Dr. Maryory Astrid Gómez Botero

Line of research: New Materials

Research groups

Cements, Ceramics and composites – CCComposites
Centro de Investigación, Innovación y Desarrollo de Materiales – CIDEMAT

Universidad de Antioquia
Facultad de Ingeniería, Doctorado en Ingeniería de Materiales
Medellín, Colombia
2020

ACKNOWLEDGMENT

I thank my wife Adriana for her love, support, and company. Thank you very much for your continuous teaching, for your patience and understanding, for the wonderful years you have given me. Thank you very much to my daughter María José, her existence gives my life many joys, satisfactions, and purposes.

To my mother María Lucila, who filled me with love, she taught me to dream and pursue those dreams and she always has me in her prayers. Thanks to my father Jesús Antonio for the good teaching that today, I still carry with me.

I Want to thank my brothers, Omar, Diana, and Francisco for believing in me, for the love they have always expressed me and made me feel. Thank you very much for the motivation you generate. Omar for his brilliance with his work at CERN, in the world of science and his spirit of solidarity. Diana for her tenacity, dedication to the family and fighting spirit, Francisco with his humbleness, wisdom and the nobleness that characterizes him, thank you very much.

My childhood friends Dairo Gallego, Wilson Vargas and Alveiro Cadavid, because since childhood they have been there on the different paths traveled in life.

A very special thanks to the Institución Universitaria de Envigado, its directors and the teamwork headed by President Dr. Blanca Libia Echeverri. Dean of the Engineering Faculty, Engineer Jonier Rendón Prado and the head of Basic Sciences and mathematics, Gladys Adriana Betancur Jaramillo, for the constant support and backing in the associated administrative processes to carry out this doctoral thesis.

To my coworkers, Paula Tamayo, Betsy Estrada, Maribel Arroyave, Sobeida Giraldo, Natalie Ortiz, Erica Correa, and Julián Mauricio Granados, for sharing part of their lives with me, for all the moments that we have shared in recent years.

To my thesis advisors, Dr. Henry Alonso Colorado, and Dr. Maryory Astrid Gómez, for their constant support, dedication and always being there, attentive to the evolution of the processes and the review of results. Thank you very much for your patience and understanding. Thank you both very much for putting all your efforts to make me a good researcher. It has been very rewarding and an honor for me to have you as my thesis directors.

To the family psychiatrist, Dr. Carlos Herrera, for his love, fraternity, solidarity and his permanent support in moments of dispersion.

Finally, I thank the universe because it is within me and I within it.

DEDICATION

To my grandparents Francisco and Otilia who are in heaven and to my daughters, María José on earth and Daniela in heaven.

who have given me so much love and purpose in this life.

SUMMARY

Calcium aluminate cements (CAC) are important materials today, as they cover a good number of applications in civil engineering, refractory industry and materials science, which is mainly due to their excellent high temperature mechanical properties, strength to corrosion, erosion wear, among others.

The inherent brittleness and lack of ductility of these cements, particularly make them susceptible to failures mainly by thermal shock and slow outflow. In order to understand and elucidate the micro mechanisms that govern outflow damages and / or high temperatures, it is necessary to know the high temperature behavior of calcium aluminate cement pastes, the transformations of their phases, and their types and mechanisms of damage, complex phenomena related to factors such as chemical composition, water / cement ratio and alumina content.

Calcium aluminate cements are the basis for the manufacture of many refractory ceramics, advanced ceramics, and functional materials with gradients used in many different applications. Therefore, this proposal is intended to contribute to the understanding of the behavior of pure calcium aluminate cement paste and added with silica, for different alumina contents, subjected to high temperatures and using different water/cement ratio (W/C).

In order to improve knowledge in this topic, once the calcium aluminate cement paste samples have been manufactured, they were exposed to high temperatures and analyzed using techniques such as scanning electron microscopy, infrared transformation spectroscopy of Fourier, X-ray diffraction, X-ray fluorescence, among others. Then, to be able to establish mathematical models that allow the damage to be quantified and the micro-mechanisms that govern this behavior to be revealed.

AUTHOR'S CONTRIBUTION STATEMENT

The following publications were derived from this thesis:

1. **Structure property relational and Weibull analysis of calcium aluminate cement pastes**
   John F. Zapata, Maryory Gómez, and Henry A. Colorado. "Structure-property relation and Weibull analysis of calcium aluminate cement pastes." Materials Characterization 134 (2017): 9-17. ISSN: 1044-5803. DOI: http://dx.doi.org/10.1016/j.matchar.2017.10.010.
2. **Characterization of two calcium aluminate cement pastes**
   John F. Zapata, Maryory Gómez, and Henry A. Colorado. "Characterization of two calcium aluminate cement pastes." Advances in High Temperature Ceramic Matrix Compo sites and Materials for Sustainable Development; Ceramic Transactions, Volume CCLXIII 263 (2017): 491-503. ISSN: 1042-1122. https://doi.org/10.1002/9781119407270.ch45
3. **Calcium aluminate cements subject to high temperature**
   John F. Zapata, Maryory Gómez, and Henry A. Colorado. "Calcium Aluminate Cements Subject to High Temperature." Advances in Materials Science for Environmental and Energy Technologies VI: Ceramic Transactions 262 (2017): 97-105. ISSN: 1042-1122.
   DOI: 10.1002/9781119423799.ch10
4. **Cracking in calcium aluminate cements pastes induced by different exposure temperatures**
   Zapata, John F., Maryory Gómez, and Henry A. Colorado. "Cracking in Calcium Aluminate Cement Pastes Induced at Different Exposure Temperatures." Journal of Materials Engineering and Performance 28.12 (2019): 7502-7513.
   DOI: https://doi.org/10.1007/s11665-019-04466-5
5. **Effect of high temperature and additions of silica on the microstructure and properties of calcium aluminate cement pastes.**
   Zapata, John F., Henry A. Colorado, and Maryory A. Gomez. "Effect of high temperature and additions of silica on the microstructure and properties of calcium aluminate cement pastes." Journal of Sustainable Cement-Based Materials (2020): 1-27. https://doi.org/10.1080/21650373.2020.1737593
6. **Calculation of activation energies of calcium aluminate cement pastes added with micro silica subjected to high temperatures**
   Submitted to publish
7. **Calcium aluminate cements with silica contents under high temperature compression tests**
   Submitted to publish

The articles were rewritten in a consistent format throughout the thesis. The reference numbers in the manuscripts were adjusted accordingly.

OTHER ACADEMIC PRODUCTS AND PARTICIPATION IN INTERNATIONAL EVENTS

Chapter of the book

1. **Calcium aluminate cements subject to high temperature**. Advances in Materials science for environmental and energy technologies VI. In: United States: ISBN: 9781119423768 ed: J Wiley and Sons, v., p.97 - 105, 2017.
2. C**haracterization of two calcium aluminate cement pastes.** Advances in High Temperature Ceramic Matrix Composites and Materials for Sustainable Development. In: United States ISBN: 9781119406433 ed: J Wiley and Sons, v., p.482 - 492 ,2017.
3. **High Temperature Cracking Damage of Calcium Aluminate Cements.** TMS 2018 147th Annual meeting & Exhibition Supplemental proceedings. In: United States. ISBN: 978-3-319-72525-3 ed: Springer Verlag Publishing Company, v., p.553 - 563 ,2018.

Participation in international conferences

1. TMS Annual Meeting & Exhibition of the Minerals, Metals and Materials Society (2020) 149th: San Diego, California USA.
2. TMS Annual meeting & Exhibition (2018): Phoenix Convention Center. Phoenix, Arizona. USA.
3. MS & T. Materials Science & Technology (2016). Salk Lake City Salt Lake City International Congress.
4. 9th International Conference on High Temperature Ceramic Matrix Composites (HTCMC-9) & Global Forum on Advanced Materials and Technologies for Sustainable Development (GFMAT 2016) - Toronto Marriot Downtown Eaton Center Hotel, Toronto, Canada.
5. International Materials Congress (2015): Paipa Hotel Convention Center. Boyacá – Colombia.
6. 41 congreso ALAFAR Refractarios: Innovación a altas temperaturas (2018) Medellín. Hotel Marriot. Antioquia-Colombia.

CONTRIBUTIONS OF THIS THESIS

This thesis presents 4 main contributions to the study of the behavior of calcium aluminate cement pastes subjected to high temperatures:

The first contribution was to establish a methodology to quantify the damage of calcium aluminate cement pastes.

The methodology consists:

- first of taking high-resolution photographs of the cracks generated by the effect of temperature. The total length of the crack was defined with the only parameter of damage.
- Subsequently digital image processing is done with the ImageJ software, which allows measuring the length of the cracks, considering different scaling, changing tones, among others.
- Then a statistical analysis is performed to find the probability of damage curves and a Monte Carlo simulation and finally the data is fitted to a deterministic phenomenological model.

The implementation and development of this methodology is detailed in Chapter 5.

The second contribution of this thesis, is a consequence of implementing the methodology mentioned in number 1, was to establish a deterministic phenomenological model that provides the amount of damage suffered by aluminate cement pastes when they are subjected to a determined temperature, taking into account count, the alumina content, the water to cement ratio and the temperature. The model is as follows:

$$\delta_j^i = 8\omega k_R 10^{-5} T^2 - 0.1364\omega k_R T + 66.28\omega k_R$$

The details of its interpretation, meanings and implementation are developed in Chapter 5.

The third contribution of this thesis was to establish another methodology to quantify the damage but this time, the damage generated by creep. The methodology consists of:

i. Obtain the experimental creep strain curves.
ii. Fit the experimental curves by non-linear regression methods to the theta projection method and estimate its 4 parameters.
iii. With the values of the parameters the amount of damage is determined.

iv. This total damage is compared with the amount of damage obtained with the methodology set out in number 1 to establish the amount of damage due exclusively to creep.

The implementation and results of this methodology are detailed in chapter 8.

The fourth contribution is a consequence of implementing the methodology mentioned in numeral 3 and consists of establishing the phenomenological models of creep strain and the micro-mechanisms that govern this strain, using the Nabarro-Herring models in addition. The strain models obtained are:

CACP51-0wt% silica

$$\epsilon = 0.9558(1 - e^{-0.9980t}) + 0.9503(e^{0.0998t} - 1)$$

CACP51-10wt% silica

$$\epsilon = 0.0490(1 - e^{-0.9371t}) + 0.8505\ (e^{0.0685t} - 1)$$

CACP51-20wt% silica

$$\epsilon = 0.4131(1 - e^{-0.7936t}) + 0.7508\ (e^{0.0373t} - 1)$$

CACP71-0wt% silica

$$\epsilon = 1.0221(1 - e^{-0.7090t}) + 0.814031(e^{0.0931t} - 1)$$

CACP71-10wt% silica

$$\epsilon = 0.0473(1 - e^{-0.4791t}) + 0.7917(e^{0.0939t} - 1)$$

CACP71-20wt% silica

$$\epsilon = 0.8119(1 - e^{-0.9458t}) + 0.7693(e^{0.0940t} - 1)$$

and the established creep micro-mechanisms are: sliding Rachinger, in all formulations. The operational details of these results are developed in Chapter 8

NOMENCLATURE

Symbol	Chemical formula	Name
C	CaO	Calcium oxide
A	Al_2O_3	Alumina
F	Fe_2O_3	Iron oxide
S	SiO_2	Coesite
H	H_2O	Water
W	Fe_5SiO_8	Wadsleyite
Wu	FeO	Wustite
T	TiO_2	Titanium oxide
	Nomenclature for the derived anhydrous cement powder	
CA	$CaAl_2O_4$	Monocalcium aluminate (Krotite)
CA_2	$CaAl_4O_7$	Monocalcium dialuminate Grossite
CA_6	$CaAl_{12}O_{19}$	Hibonite
$C_{12}A_7$	$Ca_{12}Al_{14}O_{33}$	Mayenite
C_4AF	Ca_2AlFeO_5	Tetra calcium ferroaluminate
C_5A_3	$Ca5Al_6O_{14}$	Pseudo-mayenite
CF	$CaFe_2O_4$	Calcium Ferrites
P	$CaTiO_3$	Perovskite
CF_2	$CaFe_4O_5$	Calcium Ferrites
C_2F	$CaFe_4O_6$	Calcium Ferrites
C_6AF_2	$Ca_6Al_2Fe_4O_{15}$	Calcium Ferrites
CT	$CaTiO_3$	Calcium titanium
C_2S	Ca_2SiO_4	Bi-calcium silicate
CAS_2	$CaO.\ Al_2O_3.\ 2SiO_2$	Anorthite
C_2AS	$Ca_2Al_2SiO_7$	Gehlenite
C_2FS_3SiO	$Ca_2Fe_2Si_4O_{12}$	Hedenbergite
CSH	$CaSi(O_2H)_2$	Calcium silicate hydrate
	Nomenclature for the hydrate phases	
CAH_{10}	$CaAl_2O_{14}H_{20}$	Monocalcium aluminate decahydrate
C_3AH_6	$Ca_3[Al(OH)_6]_2$	Katoite- Hydrogarnet
C_2AH_8	$Ca_2Al_2O_{13}H_{16}$	Dicalcium aluminate octahydrate
AH_3	$Al(OH)_3$	Gibbsite-Bayerite
C_2ASH_8	$Ca_2Al_2Si_8O_{16}$	Stratlingite
	AlO_3	Nordstrandite

wt%	: Weight by percentage
CAC 51wt%	: Calcium Aluminate Cement Powder with 51 wt% of Alumina
CAC 71wt%	: Calcium Aluminate Cement Powder with 71 wt% of Alumina
CACP 71-nwt%	: Calcium aluminate cement paste with 71 wt% of alumina and n wt% of silica
CACP 51-nwt%	: Calcium aluminate cement paste with 51 wt% of alumina and n wt% of silica
[71-n-T]	: CAC71-nwt% - T°C in FTIR analysis
[51-n-T]	: CAC51-nwt% - T°C in FTIR analysis
(COD Number)	: Code database COD (Crystallography Open Database)
α	: Degree of conversion

k_0	: Pre-exponential (frequency) factor.
β	: Constant heating rate
$f(\alpha)$	: Reaction model
$T_{\alpha,i}$	: Temperature (for a given conversion value)
T_m	: Temperature at point of the thermogram at which the reaction rate is maximum
x	: Volume fraction
Q	: Activation energy
R	: Gas constant

ABBREVIATIONS

CAC	: Calcium Aluminate Cement
CACP	: Calcium Aluminate Cement Paste
W/C	: Water/Cement ratio
CP	: Cement Portland
SEM-EDS	: Scanning Electron Microscopy with Energy Dispersive X-ray Spectroscopy
TGA	: Thermal Gravimetric Analysis
XRD	: X-ray Diffraction
FTIR	: Fourier Transform Infrared Spectroscopy
XRF	: X-ray Fluorescence
TPM	: Theta Projection Model
FWHM	: Full Width at Half Maximum

Content

LIST OF TABLES

LIST OF FIGURES

1. CHAPTER 1: INTRODUCTION

1.1 GENERAL FEATURES

Calcium aluminate cements (CAC), also called high alumina cements (HAC) or aluminous cement (AC), are the most important type of non-Portland cement or special cement. Even so, the volume used each year is only about one thousandth compared to the use of Portland Cement, since they are considerably more expensive (four to five times), therefore, it is not economical to use them as a simple substitute for Cement Portland [1].

The CAC is manufactured industrially from mixtures of limestone and high Al_2O_3 materials (bauxites, laterites, alumina obtained by Bayer process, among others) or alumina. The quality of these cements depends on the content of impurities (iron, silicon, magnesium, alkali oxides) present in the raw materials and the more or less oxidizing or reducing nature of the furnace atmosphere in which it melts or clinkerizes, which can compromise its use in certain refractory applications. Its use is justified in cases where special properties are required of a concrete or mortar, either as the main binder phase or as a component of a mixed binder phase. Some of the properties that can be achieved through the use of CAC are [2]:

1. Fast hardening.
2. Strength to high temperatures and temperature changes.
3. Strength to chemical attack, particularly acids.
4. Strength to impact and abrasion.

Nowadays almost all the production of the different types of CAC is used in the manufacture of refractory concretes [3]. CACs are also widely used in combination with other mineral binders (for example, Portland cement, calcium sulfate, lime) and additives to produce a range of specialized mortars for applications such as repair, floor leveling, adhesives and tile grout. Traditional concrete use is usually where severe conditions, such as extreme temperatures, exposure to harsh chemicals, mechanical abrasion or impact, must be faced, often in industrial situations and where these severe conditions are combined with a need for a rapid return to the solicitation [1,4].

Calcium aluminates (CA) are also widely used in the steel industry due to their relatively low density, hardness, straightness, etc. [5]. The CA has received considerable attention as a material for (implants) bone grafting application due to its unique combination of physical, mechanical, bioactive and biocompatible properties [6,7]. CA-based glasses have technological importance in the application of optical devices [8,9].

In this thesis, an experimental study of CACP is carried out, with different alumina contents and water / cement ratios subjected to temperatures of 500, 800 and 1000 ° C, to know its behavior in its microstructural phases and against damage. The influence of silica, at high temperatures, on the formation of phases and mechanical properties is also analyzed, such as the creep behavior at high temperature of some formulations, and the activation energies of some dehydration processes are also calculated.

In this work, the chapter 2 deals with processes, properties and characteristics of CACs such as:

1. Anhydrous phases
2. Hydration process
3. Conversion process
4. CACP high temperature behavior

A general description of the methods and models in non-isothermal analysis and a state of the art in ceramic materials and phases of calcium aluminate cement is provided.

Chapter 3. In this chapter is described the methodology and the experimental program used to carry out this research.

Chapter 4. In this chapter is described the results of the characterization of the CAC and CACP used in this investigation, carried out with different techniques, laser granulometric, X-Ray Fluorescence (XRF), X-ray diffraction (XRD), Scanning Electron Microscopy-Energy Dispersive X-ray spectroscopy (SEM –EDS), and Fourier transform infrared (FTIR), compression tests.

Chapter 5, the damage is analyzed in CACP when subjected to high temperatures, a methodology to quantify the damage is implemented and the values are related to factors such as:

1. Temperature
2. Water/Cement ratio (W/C)
3. Alumina content

Chapter 6 is analyzed the damage and high temperature behavior in CACP 51wt%, added with silica to know its influence on the amount of damage and the transformation of the phases, using TGA test.

Chapter 7, the kinetic of the CACP 71wt% when is subjected to high temperature are analyzed and modeled, using thermal analysis methods with techniques non-isothermal.

Chapter 8, results of high temperature creep analysis, micro mechanisms and damage analysis are established.

Chapter 9, it’s about, general conclusions and some recommendations

1.2 OBJECTIVES

1.2.1 GENERAL OBJECTIVE

Conduct an experimental study of CACP, with different alumina contents and water /cement ratios subjected to temperatures of 500, 800 and 1000°C, to know their behavior in their microstructural phases and against damage.

1.2.2 SPECIFIC OBJECTIVES

1. Determine the characteristics of the microstructure, mechanical properties and chemical composition to know the initial conditions of the starting calcium aluminate cement.

2. To evaluate the effect of temperatures (500, 800 and 1000 °C) on CACP, for different water/cement ratios, on the microstructure.

3. Quantify the damage occurred at temperatures (500, 800 and 1000 °C) in CACP for different water/cement ratios.

4. Propose a phenomenological mathematical model that describes the behavior at temperatures (500, 800 and 1000 °C) in calcium aluminate cement pastes in relation to the microstructure, type of cement and the water/cement ratio.

2. CHAPTER 2: THEORETICAL CONSIDERATIONS AND STATE OF THE ART

2.1 INTRODUCTION

The CAC is a hydraulic cement that is formed by reaction of lime and alumina, either by a sintering process, or by fusion (clinker). More appropriately [10]:

Calcium aluminate cements are obtained by fusing or sintering of a mixture of suitable proportions of aluminous and calcareous materials and milling the resulting product to fine powder.

The main mineral phases present in the CACs are calcium mono aluminate (CA), calcium dialuminate (CA_2), dodecalcium heptaaluminate ($C_{12}A_7$) and alpha-alumina (α-Al_2O_3). All CAC properties depend only on their mineralogical phase composition. Until the early 1950s, commercially available CACs contained large amounts of Fe_2O_3 and SiO_2 as impurities. The presence of these oxides limited the use to relatively low temperature applications. In the late 1950s, higher-purity calcium aluminate cements were obtained which expanded the use of refractory concretes and higher temperature applications. A CAC classification comprising only three groups based on alumina content and purity; low purity, intermediate purity and high purity, which is given in Table 1.

Table 1. CAC classes based on impurities [11].

Phase: wt%	Low purity	Intermediate purity	High purity
SiO_2	4.5-9.0	3.5-6.0	0.0-0.3
Al_2O_3	39-50	55-66	70-90
Fe_2O_3	7-16	1-3	0.0-0.4
CaO	35-42	26-36	9-28

The specific gravity of the CACs varies between 3.00 and 3.25 kg/m^3 and is also largely controlled by the iron content. It is reasonable to assume an apparent density is 1.44 g/cm^3, but as with all cements, values between 1.12 and 1.74 g/cm^3 can be obtained, according to the method applied. The specific surface area measured by the British Standard method can vary between 2.500 and 4.000 cm^2/gr.

2.2 RAW MATERIALS

Calcium aluminate cements are prepared by mixing, melting or cooking and subsequent cooling and milling of mixtures of calcareous and aluminous materials [11]. Lime is mainly used and it is often used hydrated due to its easy availability and purity factors. Hydrated lime is calcium hydroxide with the chemical formula of $Ca(OH)_2$. In hydrated lime, a

sufficient amount of water has already been added at the manufacturing stage to fully hydrate it. As for the aluminous materials, different types are used in the production of CACs that contain Al_2O_3 depending on the quality or purity. The requirements for the final product and the cost are as follows:

- Calcined alumina (for high purity CAC)
- White fused alumina and
- Reactive alumina

The calcined alumina offers plasticity, better rheological properties and plays a significant role in fluency. [11]. The calcined alumina is aluminum oxide that has been heated to temperatures above 1.050 °C to expel almost all chemically combined products with water. In this way, alumina has a high chemical purity, high density and a high melting point (slightly above 2.050 °C). White molten alumina is produced by melting calcined alumina above 2040 °C in an electric arc furnace. It has a very high chemical purity (> 99% Al_2O_3), high refractoriness, abrasion resistance, as well as inert, but very expansive chemicals. Reactive alumina is the term normally given to a relatively high purity alumina and a small crystal size (<1 mm) is sintered in a completely dense body at temperatures lower than alumina low in soda, medium in soda or alumina of ordinary soda. "Reactive" alumina powders are normally supplied after intensive grinding that breaks the agglomerates produced after calcination [11].

2.3 ANHYDROUS PHASES

The properties of the constituent minerals of CACs as their typical chemical composition in their anhydrous phase are shown in

Table 2.

Table 2. Properties of the constituent minerals of CAC [12].

Mineral	Chemical composition (wt%)				Tm (°C)	Density (g/cm^3)	Crystal structure	Formation Enthalpy [kJ/mol]
	CaO	Al_2O_3	Fe_2O_3	SiO_2				
C	99.8	–	–	–	2570	3.32	Cubic	–
$C_{12}A_7$	48.6	51.4	–	–	1405-1495	2.69	Cubic	–
CA	35.4	64.6	–	–	1600	2.98	Monoclinic	-2323 [13]
CA_2	21.7	78.3	–	–	1750-1765	2.91	Monoclinic	- 4023 [14]
C_2S	65.1	–	–	34.9	2066	3.27	Monoclinic	–
C_4AF	46.2	20.9	32.9	–	1415	3.77	Orthorhombic	–

C_2AS	40.9	37.2	−	21.9	1590	3.04	Tetragonal	−
CA_6	8.4	91.6	−	−	1830	3.38	Hexagonal	−
Al_2O_3	−	99.8	−	−	2051	3.98	Rhombohedral	

A fundamental difference of CACs with PCs is the content of Al_2O_3 and SiO_2. For CAC the SiO_2 content is < 15% preferably < 5% and for Portland cement it is > 18%. For CAC the content of Al_2O_3 is > 30% and for PC < 6%. Other important differences between these cements is shown in Table 3.

Table 3. CAC and PC modules

Modulus	PC (wt%)	CAC (wt%)
Hydraulic module $\frac{\%CaO - 0.7\%SO_3}{\%SiO_2 + Al_2O_3 + Fe_2O_3}$	1.7-2.3	0.55-0.8
Silicon module $\frac{\%SiO_2}{\%Al_2O_3 + Fe_2O_3}$	1.6-3.2	0.08-0.35
Flux module $\frac{\%Al_2O_3}{\%Fe_2O_3}$	0.6-2.5	2.9

2.4 CAC HYDRATION PROCESS

Hydration is an exothermic process and at the same time highly dependent on experimental factors such as [15–17]:

- Agitation (homogeneity)
- Temperature
- W/C
- Time
- Cement reactivity (particle size)
- RH: Relative humidity of the environment
- Alumina content
- Content of minority phases
- Crystallinity of main phases
- pH (alkalinity. Presence of alkalis)
- Porosity

The influence of these factors often hinders the identification and quantification of all the phases present and the understanding of hydration itself, a fact that is confirmed by the existence of a large number of scientific papers on the subject, which makes its understanding many times confusing the physical and chemical processes involved during hydration are not yet well-known [18–23].

Several approaches to describe the nature and formation of hydrates during the early stage have been reported in the literature [21,24,25]. Conductivity and pH measurements, generally performed in dilute systems, allow hydration to be described as a solution and a precipitation process [24,25].

Hydration products and their phases are responsible for the formation of the hydraulic bond and the mechanical properties in green of refractory ceramics. However, these hydrated phases, when are heat treated, decompose, generating products that crystallize in the form of highly reactive non-hydrated calcium aluminates, responsible for the formation of ceramic bonding (sintering process) at temperatures significantly lower than those needed if starting from the same aluminates of calcium [26–29].

The main hydraulic phase of all CACs is the CA phase. Of all the influencing factors the temperature is the most important, the hydration products depend significantly on the curing temperature [19,24,30]. According to several studies, the initial hydration product that emerges within the temperature range between 0 and 15°C is predominantly CAH_{10}, while between 15°C and 35°C the predominant phases are CAH_{10}, C_2AH_8 of hexagonal morphology and amorphous AH_3 [23,31–34]. CA hydration is primarily responsible for the early development of resistance, while CA_2 hydration contributes after the main CAC hydration reaction has already been exceeded [35].

When the CaO/Al_2O_3 ratio exceeds the unit, small amounts of C_2AH_8 are also found as a result of CA_2 hydration or CAH_{10} conversion (see section 2.3) [36].
After longer periods of hydration, the amorphous phases can become crystalline phases, such as CAH_{10}, C_2AH_8 /$C_2AH_{7.5}$ and AH_3 [1,30,37–39]. In the temperature range between 35 and 90 °C, however, the only stable phases of CAC are C_3AH_6, called Hydrogarnet, Hydrogrossular or Katoite, together with aluminum hydroxide, AH_3, known as Gibbsite, which is precipitated [30,40,41].

In white CACs, rich in Al_2O_3, calcium mono dialuminate (CA_2) is the second major phase that emerges [31]. CA_2 tends to react very slowly within the first 48 hours. For this reason, in many previous studies, CA hydration alone has been intensively investigated. For a long time, hydration of CA_2 was an open problem [42] and it was even assumed that CA_2 was inert. Then, different researchers reported the hydraulic reactivity of CA_2 [43–45], although the reported reactivity was lower than the reactivity of CA. Chudak et al [46], also

investigated pure CA_2 with 70% by weight of Al_2O_3, and described a slow hydration of CA_2 for several days.

Negro et al [47], concluded that the solubility of CA_2 is much lower than that of CA. This could explain the very low hydration reaction of CA_2. Edmonds et al [48] reported the hydraulic activity of CA_2 in Secar 71, which begins after 28–48 hours, lasts several months. AH_3 was observed by Song et al [16], to precipitate during CA_2 hydration at room temperature. Equations (1) summarizes the hydration reactions of CA and equations (2) summarizes the hydration reactions of CA_2 [3,19].

$$\begin{aligned} CA + 10H &\xrightarrow{< 15°C} CAH_{10} + \text{hot} \\ CA + 11H &\xrightarrow{\sim 30°C} C_2AH_8 + AH_3 + \text{hot} \\ 3CA + 12H &\xrightarrow{> 35°C} C_3AH_6 + 2AH_3 + \text{hot} \end{aligned} \quad (1)$$

$$\begin{aligned} CA_2 + 13H &\xrightarrow{< 15°C} CAH_{10} + AH_x + \text{hot} \\ 2CA_2 + 17H &\xrightarrow{\sim 30°C} C_2AH_8 + 3AH_x + \text{hot} \\ 3CA_2 + 21H &\xrightarrow{> 35°C} C_3AH_6 + 5AH_3 + \text{hot} \end{aligned} \quad (2)$$

It should be noted that, in contrast to Portland cement, calcium hydroxide $Ca(OH)_2$ (slaked lime) is not formed at normal temperatures under any circumstances, which is a reason why the CAC is resistant to sulfate and dilute acid attack. However, if lime is added to the aluminous cement, either in the form of slaked lime or combined as Portland cement, C_2AH_8 is rapidly formed, resulting in very rapid setting and reduced final strength [49]. The pH of the aqueous phase of the CAC pastes is approximately 12. This value does not change due to the conversion of hexagonal aluminate to cubic, but it does change significantly when the cubic phases are carbonated, pH 7-8 as in all carbonated concrete. Table 4 shows some properties of the hydrated phases.

Table 4. Densities, molar masses of the hydrated phases and enthalpy of formation [10,50,51].

Hydrated Phase	Density [g/cm^3]	Molar mass [g/mol]	Formation enthalpy [kJ/mol]
CAH_{10}	1.72	338.1	-
C_2AH_8	1.96	358.2	-5433 [52,53]
AH_3	2.44	156.0	-2578 [52]
C_3AH_6	2.52	378.3	-

2.5 PHASES OF THE HIDRATION PROCESS

1. **CA hydration**:

   Equations
   (1) show the hydration products resulting from exposure of CA with water. At temperatures below 15 °C, CAH_{10} of hexagonal morphology is fundamentally formed and as the temperatures rises above 15 °C, CAH_{10} hydrate crystallizes at C_2AH_8 preserving hexagonal morphology and amorphous gels of composition AH_x and small amounts AH_3 crystalline. At temperatures above 35 °C, C_2AH_8 dissolves and recrystallizes in the form of cubic C_3AH_6 and crystalline AH_3 is formed in considerable quantity.

2. **CA_2 hydration**:

   Equations (2) show the main hydration products that result from CA_2 coming into contact with water. Pure CA_2 reacts slowly with water, at temperatures below 15 °C, forming CAH_{10}, AH_3 (crystalline gibbsite) and aluminum hydroxide gel, with small amounts of C_2AH_8. Note that the hydration products of CA_2 are the same as those of CA, except for the small amounts of AH_3 (crystalline gibbsite), aluminum hydroxide gel and C_2AH_8 that are generated in small quantities at temperatures below 15 °C. In the presence of pure CA, CA_2 hydrates at a moderate speed [54–58]. Freitas et al [59] when studying the hydration of pure CA_2 pastes at 60 ºC with a ratio of W/C=3, they conclude that depending on the temperature the hydration of calcium dialuminate is not a slow process as stated in the literature.

3. **$C_{12}A_7$ hydration or Mayenite**:

   This compound hydrates faster than CA and CA_2. At temperatures below 15 °C, its main reaction product is a mixture of aluminum hydroxides gel, CAH_{10} and C_2AH_8 which, depending on time and temperature, become cubic C_3AH_6, while amorphous aluminum hydroxide crystallizes in the form of AH_3 [60,61]. Due to the high proportion of C/A (CaO/Al_2O_3) that may be required to form Mayenite, this calcium aluminate forms a smaller amount of aluminum hydroxide gel and crystalline gibbsite than the other calcium aluminates.

4. **Hydration of calcium aluminate phase mixtures:**

In the hydration of the CACs the presence and quantity of one phase can significantly affect the hydration kinetics of another. This is due not only to the exothermic nature of the hydration reactions of calcium aluminates, which increases the temperature of the mixtures, but also to the physical and chemical properties of the hydroxylic layer formed on the surface of aluminate particles of calcium that blocks the diffusion of water. In the literature there are several investigations that try to establish the behavior during the hydration of mixtures of different calcium aluminates, but there are conflicting results in this regard [21,54,57,62,63].

2.6 CAC CONVERSION PROCESS

According to the phase equilibrium [64] CAH_{10} and C_2AH_8/$C_2AH_{7.5}$ are thermodynamically metastable and hexagonal morphology phases, they have a higher solubility than stable phases and above 35 °C they are converted to the C_3AH_6 phase of cubic morphology. Equations (3) summarizes the conversion reactions:

$$3C_2AH_8 \rightarrow 2C_3AH_6 + AH_3 + 9H \quad (3)$$
$$3CAH_{10} \rightarrow C_3AH_6 + 2AH_3 + 18H$$

It is noted that the conversion reactions (3), produce a considerable reduction in the volume of solid products, the water released is 27 wt.% of CAH_{10} and 15 wt.% of C_2AH_8. The released water is incorporated into the available spaces (pores) or creates them. Since the reactions occur after the cement has set and hardened, the overall dimensions, which are essentially constant, are stabilized, so the change in density (see Table 4) has to be compensated by an increase in porosity. This increase in porosity, consequently, reduces its mechanical properties, and the possibility of development of micro cracks. The increased porosity also leads to an increase in permeability, so that the paste, mortar or concrete become more susceptible to chemical attack by dissolved salts, acids or alkalis in groundwater [40,65]. Porosity increases depending on external conditions (such as humidity and temperature), the conversion process can last up to several years [51] and additionally is accompanied by the release of free water, which contributes to the decrease in resistance caused by a greater porosity [51]. In refractory applications, the conversion to (C_3AH_6) does not play any role because the hardened mold will always be heated before use.

The process of converting the stable meta phases to the stable phases in the presence of water is a chemical reaction process, that is, the reaction proceeds at a rate that varies exponentially with temperature. The easiest way to express this is to estimate the time required at any temperature for the chemical reaction to have traveled half the way, as shown in Table 5 [49,50,66].

Table 5. Chemical test on CACP with W/C = 0.26

Time required for semi-conversion (conservation under constant humidity conditions)	Temperature (°C)
30 years	18
10 years	23
1 years	33
90 days	40
28 days	45
7 days	52
3 days	55
1 days	60

It should be taken into account that the change in resistance is not necessarily proportional to the degree of chemical conversion. The speed and extent of the conversion are greatly affected by the presence of moisture. The conversion of small laboratory samples is much slower in air with normal humidity than in water and can finish completely in totally dry air, regardless of temperature, so fundamentally humidity and temperature are the factors that catalyze or not, the conversion process. It should be noted that the conversion is not invariably accompanied by a drop in resistance. CAC paste exposed to the effect of seawater, showed by mineralogical examination to have undergone almost a complete conversion after about 30 years. However, the converted concrete still maintained its original strength and has resisted the action of seawater. Therefore, it seems that the conversion may not result in a decrease in resistance if the reaction has occurred quite slowly [66].

To express the degree of conversion in quantitative terms, a definition is required. For laboratory work, the degree of conversion is expressed in the equation (4):

$$\frac{\text{Weight } C_3AH_6 * 100}{\text{Weight } C_3AH_6 + \text{Weight } CAH_{10}} \quad (4)$$

Since the C_3AH_6 in the CAC is decomposed by carbonation and the amounts of C_3AH_6 and AH_3 are not very different (at 50% conversion there will be no errors greater than 4% using the above equation or the one that follows), it can be used equation (5) [67]:

$$\frac{\text{Weight } AH_3 * 100}{\text{Weight } AH_3 + \text{Weight } CAH_{10}} \quad (5)$$

The degree of conversion can be analyzed, using DRX, using the reflection of 14Å for CAH_{10} and reflection 2.82Å for gibbsite AH_3. The phenomenon of the conversion should not only refer to the passage of hexagonal hydrated aluminates to the cubic form, accelerated by high temperature and humidity, but also to the stiffening of the alumina gel when passing to crystallized gibbsite, of greater density, with the consequent increase in porosity and decrease in volume. It is difficult to assign a correct percentage of participation in the phenomenon of conversion to each of the two agents that motivate it.

2.7 NON-ISOTHERMAL ANALYSIS

The study and modeling of micro mechanisms that govern solid state reactions and high temperature kinetics is of fundamental importance to characterize various physical and chemical phenomena in organic, inorganic and metallic systems. Adequate modeling provides valuable qualitative and quantitative information on thermal properties, and most importantly, kinetic information on phase transformations [68], crystallization of metal glasses [69], solid state precipitation [70,71], decomposition [72], quasicrystalline structure of amorphous metals and alloys [73] and structural changes associated with nanomaterials [74].

The modeling of the kinetic micro mechanisms due to the behavior with the temperature in the solid state reactions, is established by theoretical considerations about the limiting step of the reaction, which involves aspects such as the diffusion of products of the decomposition of the reactants through a growing layer of reaction products, and considerations on the progress geometry of the reaction, size and shape of grain [75–78]. In this way, the researcher's task is to select among the types of models the ones that best fit mathematically, the one that most likely can describe the physical reality in correspondence with the phenomenology of the process and of the solid studied, with the use of the appropriate experimental procedures, methods and techniques for this purpose.

The kinetic study of thermally activated reactions can be performed both in an isothermal regime (constant sample temperature); as non-isothermal, when the sample temperature varies, and usually increases with constant (linear) heating rate [79–81]. The merits of the isothermal methods are: their computational and procedural simplicity, greater experimental accuracy of the results, but also has some experimental drawbacks. The biggest problems of the isothermal study are [76,82]:

1. If the sample undergoes a considerable reaction when the temperature has not yet reached the preset value, the results obtained by this method are questionable, because some degradation may occur during the preheating period, particularly when the reaction start temperature is considerably lower than the temperature of isothermal tests. In isothermal methods, some reactions take place, totally or partially, before reaching the working temperature;

2. There is uncertainty when setting the reaction start temperature;
3. It is necessary to use considerable quantities of samples, in addition to tedious work and long periods of time;
4. The evolution or consumption of heat during the process (exothermic or endothermic reactions) can significantly differentiate the temperature of the sample respect to the control, the situation is especially serious due to the fact that, under isothermal conditions, for a typical process in solid state, the degree of reaction tends to be maximum at the beginning of the transformation. This causes uncertainty in the experiment since the temperature at which to refer the reaction rate is doubtful.

Non-isothermal heating (following a linear temperature program) solves these problems. The new technologies for development of devices, of regulation and control of high precision for the measurement of changes in temperature, mass and heat, in the market of scientific instrumentation have motivated that conventional isothermal methods are displaced by non-isothermal and even now, they are more popular for the kinetic study of heterogeneous or solid state reactions [75,76,78,83,84].

The use of non-isothermal methods for the calculation of the kinetic parameters of the reactions instead of the conventional isothermal methods is fully justified [75,81,85–90].. The non-isothermal method (in particular, the one based on non-isothermal TG data) has several advantages [91,92].

1. The complex dependence of the speed of the reaction with the temperature, which makes the analytical treatment of the data complicated and prone to errors of low and/or over estimation.
2. The kinetics can be established in a complete temperature range continuously, in the entire temperature range in which the reaction takes place, without any temperature ranges not covered, as is the case with isothermal methods.
3. It is possible to obtain a lot of information with a single sample, that is, the thermal parameters, such as the temperature of the maximum decomposition rate, the characteristic temperature and the kinetic parameters.
4. The determination of the kinetic and thermodynamic parameters using a single sample eliminates the problem derived from different samples, that is, errors from sample to sample are avoided.

The main disadvantages of non-isothermal methods are:

1. The possibility of overlooking a possible change of mechanism during the course of the reaction.
2. Greater susceptibility to procedural factors.
3. The existence of temperature gradients in the reacting substances, which increase with the grain size, the degree of packaging and with the heating rate [88]. This causes the surface of the sample to react more quickly (because it is at a higher temperature)

than the interior, thus obtaining a non-uniform reaction rate. This difficulty can be reduced by working with small masses and mild heating rates [93–95].

Knowing the dynamics and the mechanisms that govern the high-temperature behavior of ceramic materials is essential for its design, the understanding of its failure mechanisms and its performance properties. In this chapter a review of the main mathematical models associated with the high temperature behavior of ceramic materials investigated by thermal analysis methods is made. Its classification, its scope, advantages and sales when modeling solid state reactions in these materials. The differential and integral models are reviewed in some detail.

2.8 HETEROGENEOUS SOLID-STATE REACTIONS

Heterogeneous solid-state reactions occur when two phases, A and B come into contact and react to form one or several phases of different product C and/or D. A and B can be chemical elements or compounds. A study of solid state reactions has three aspects namely [96,97].

- Phenomenological,
- Kinetic and
- thermodynamics.

The phenomenological study deals with the qualitative observation of the phenomena that occur during the solid-state reaction. The thermodynamic approach involves the study of equilibrium states, while the kinetics is related to the reaction rate and the mechanism of decomposition. This review focuses mainly on phenomenological and kinetic aspects.

Solid state reactions can be classified as [98]:

1. $A(solid) \rightarrow B(solid) + C(gas)$
2. $A(solid) + B(solid) \rightarrow C(solid) + D(gas)$
3. $A(solid) + B(solid) \rightarrow C(solid) + D(solid)$
4. $A(solid) \rightarrow B(solid) + C(liquid)$
5. $A(solid) + B(gas) \rightarrow C(solid)$

The common aspect of these reactions is that they involve an interface between the reactant and the solid product, which gives rise to a special, particular kinetics, which has features common to all types of reactions indicated. In solid state reactions: a solid that is stable at ordinary temperature, to undergo decomposition with a measurable velocity, it would need energy, in the form of heat. In heating, a solid may undergo physical and / or chemical changes, which may include [98]:

1. Phase changes,
2. Sintering,
3. Fusion and
4. Thermal decomposition

The activation energy is defined as the difference between the internal energy of the system in the transition state and that of the initial state, it is that minimum amount of energy required to initiate a chemical reaction, phase transformation or activation of some mechanism [75,99]. Thermal stimulus activation of a heterogeneous reaction is one of the most common methods to study the kinetics of a process. The most commonly used experimental techniques to study thermally activated mechanisms are thermal analysis methods. Mackenzie [100] has classified these methods as

1. Thermo-gravimetric analysis or thermogravimetry (TGA) - (TG)
2. Differential thermogravimetry (DTG)
3. Determination of isobaric change in weight
4. Differential thermal analysis (DTA)
5. Differential scanning calorimetry (DSC)
6. Dilatometry
7. Analysis of evolved gases (EGA)

However, these methods of thermal analysis alone are not sufficient for a complete, more accurate and consistent analysis of the nature of the process. For this reason, it is necessary to complement thermal analysis techniques with characterization methods. For the chemical and mineralogical composition, such as:

1. X-ray diffraction (XRD)
2. X-ray fluorescence (XRF)
3. Fourier-transform infrared spectroscopy (FTIR) and microwave
4. Dynamic reflectance spectroscopy
5. Steam phase chromatography
6. Mass spectrometry (MS).
7. Electron paramagnetic resonance (EPR)
8. Nuclear magnetic resonance (NMR).

For the morphology analysis characterization methods are used such as: scanning and transmission electron microscopy (SEM and TEM). Thus, while thermal analysis methods can provide important determinations to the global kinetics of a thermally activated mechanism, the complementary techniques allow to deepen the analysis of the reaction mechanism and reach coherent and well-supported conclusions of the phenomenon that limits the speed of the process studied [76,77].

2.9 CONCLUSIONS

- The use of non-isothermal methods for the calculation of the kinetic parameters of the reactions instead of the conventional isothermal methods is fully justified. [75,81,85–90]
- The difficulties of non-isothermal methods can be reduced by working with small masses and mild heating rates [93–95].

3. CHAPTER 3: EXPERIMENTAL PROGRAM AND METHODOLOGY

3.1 METHODOLOGY

This thesis was developed in two main phases:

I. **Experimental phase**: in this phase via a characterization program: chemical, mineralogical, thermal, morphological (micro structural) and mechanical, an experimental study of the CACs is carried out in its anhydrous and hydrated phase, before and after subjecting the pastes to high temperature, particularly at 500°C, 800°C and 1000°C, (samples subjected to constant stress (creep) and without stress) with the idea of thoroughly knowing the starting raw materials and obtaining information particularly on the behavior at these temperatures, at microstructural level, on the micro mechanisms that govern these behavior, related to factors such as:

a. Temperature
b. Water/Cement ratio (W/C)
c. Alumina content
d. Micro silica content.

The temperatures of 500, 800 and 1000 ° C were selected based on a review of the state of the art. At 500°C, the amorphousity is decreased and some peaks characterizing monocalcium aluminate are detected [101,102].

Micro silica containing bonding systems, which can contain zeolitic calcium aluminate silicate hydrates, begins dehydration at temperatures above 500°C and then develop gehlenite and/or anorthite. Additionally, the pores filled with fine SiO_2 and possibly the precipitation of the partially suspended silica contribute to strength development in the temperature range of 500-1000°C [103].

At 800 ° C the formation of $C_{12}A_7$ and CA_2 begins (pH 7, 8 and 10) and in the range from 900 to 1100 ° C the formation of CA [38,104].

Structure of the formed CAC stone hydrates and the contours of the crystal forms of hydrates remain unchanged after dehydration, which finishes in heating the CAC stone at 800 ºC [38].

when the cement stone is heated at the temperature of 1000 ºC - the amount of fine particles and pores increase highly. at this temperature, the reactions in solid state materials proceed and as a result the amount of $C_{12}A_7$ is decreasing, while the amount of CA and CA_2 are increasing [38].

II. **Mathematical modeling phase:**

In this phase a mathematical modeling is made from the data and the experimental curves obtained in Phase I. The study and modeling of micro mechanisms that govern solid state reactions and/or high temperature kinetics is of fundamental importance for characterize various physical and chemical phenomena. Proper modeling provides valuable qualitative and quantitative information on thermal properties, and most importantly, kinetic information on phase transformations, decomposition by dehydration or other reactions.

The kinetic study of thermally activated reactions was performed in a regime non-isothermal, when the temperature of the sample varies, and increases with a constant (linear) heating rate. Creep mechanisms were established using theta projection methods

As indicated above, the general objective of this experimental study is conducting an experimental study of CACP, with different alumina contents and water/cement ratios subjected to temperatures of 500, 800 and 1000°C, to know their behavior in their microstructural phases and against damage.

Therefore, different CAC powder types were used. Different pure CACPs were prepared and added with silica to be subjected to a program of different temperatures to carry out a thermal analysis of the behavior of their phases. The characteristics of the materials used in this study are given in the following sections and details of the experimental study will be discussed in the following sections.

3.2 MATERIALS

Two types of CAC powders were investigated. Details of chemical composition are presented below.

CHEMICAL COMPOSITION OF RAW CAC POWDERS

Sample	Chemical Composition (wt%)								
	Al_2O_3	CaO	SiO_2	TiO_2	Fe_2O_3	K_2O	P_2O_5	ZrO_2	MoO_3
CAC 51wt%	52.12	37.82	5.25	1.87	1.81	0.128	0.108	0.086	0.052
CAC 71wt%	71.09	28.38	0.238	–	–	–	–	–	–

The distribution of granulometry of the CAC powder was determined by laser diffraction, which showed an average grain size of 4 μm.

Samples of CACP 51 and 71 wt% were fabricated with W/C = 0.4 and additions of high purity micro silica (SiO_2) with 10 wt% and 20 wt%. The micro silica presents a 99.98 and 98.9% purity, granulometry of 2 μm and 0.16 μm, respectively, was obtained from a Colombian natural source.

Details of the manufacturing conditions and dimensions of the specimens studied in this study, such as the mechanical, chemical, and morphological characterization of CAC powders and manufactured CACPs, were published in the Journal "Materials Characterization" and are shown in the Chapter 4.

3.3 SAMPLE MANUFACTURING PROGRAM

The designs of experiments carried out in this study are described in the form of tables that are presented in each chapter corresponding to the particular analysis carried out, distributed as follows:

- Chapter 4. Corresponds to the Characterization of raw materials and manufactured samples.

FORMULATIONS FABRICATED FOR CEMENT PASTE SAMPLES

Samples	Cement type	Temperature (°C)	Water/cement (W/C)
1	CAC 51wt%	20	0.4
2	CAC 51wt%	20	0.5
3	CAC 71wt%	20	0.4
4	CAC 71wt%	20	0.5

- Chapter 5. Behavior with the temperature CACP 51 and 71 wt% pure, without additions of silica.

CEMENT PASTE SAMPLES FABRICATED FORMULATIONS

No	Cement type	Temperature (°C)	Water/Cement (W/C)
1	CAC 51wt%	20	0.25, 0.3, 0.4
2	CAC 51wt%	20	0.25, 0.3, 0.4
3	CAC 51wt%	20	0.25, 0.3, 0.4
4	CAC 71wt%	20	0.25, 0.3, 0.4,
5	CAC 71wt%	20	0.25, 0.3, 0.4,
6	CAC 71wt%	20	0.25, 0.3, 0.4,

- Chapter 6. Behavior with CACP temperature 51wt added with silica.

FORMULATIONS FABRICATED FOR CEMENT PASTE SAMPLE WITH ADDITIONS OF SILICON OXIDE

Formulations

No	CEMENT	W/C	SiO_2 wt%	T (°C)
1	CAC 51wt%	0.4	0	20
2			10	
3			20	

- Chapter 7. Behavior with the temperature CACP 71wt added with silica.
  FORMULATIONS FABRICATED FOR CEMENT PASTE SAMPLE WITH ADDITIONS OF SILICON OXIDE

Formulations				
No	CEMENT	W/C	SiO_2 - wt%	T (°C)
1	CACP 71wt%	0.4	0	20
2			10	
3			20	

- Chapter 8. Creep behavior of CACP 51 and 71 wt% added with silica.

  FORMULATIONS FABRICATED FOR CEMENT PASTE SAMPLES WITH ADDITIONS OF SILICON OXIDE

Sample	W/C	SiO_2 (wt%)	T (°C)
CACP 51wt%	0.4	0	20
CACP 51wt%	0.4	10	20
CACP 51wt%	0.4	20	20
CACP 71wt%	0.4	0	20
CACP 71wt%	0.4	10	20
CACP 71wt%	0.4	20	20

3.4 EXPERIMENTAL TESTS

MECHANICAL CHARACTERIZATION

3.4.1 POROSITY, DENSITY AND ABSORPTION TESTS

Porosity, density and absorption were established under the tests and requirements established in the international standard ASTM C 642-97 for CACP. The mass measurements required by this standard were performed with a Mettler Toledo AB204 balance with a sensitivity of 0.1 mg.

3.4.2 GRANULOMETRY TESTS

The distribution of granulometry of the CAC powder was determined by laser diffraction. DTP - LÁSER - MS 3000 - MALVERN

3.4.3 COMPRESSION TESTS

The compression tests were conducted in a universal Shimadzu Autograph apparatus at a crosshead speed of 1mm/min.

CHEMICAL AND MINERALOGICAL CHARACTERIZATION

3.4.4 X-RAY FLUORESCENCE (XRF) TESTS

XRF tests were conducted in a Thermal spectrometer model OPTIM'X.

3.4.5 X-RAY DIFFRACTION (XRD) TEST

XRD characterization were done in a X'Pert PRO diffractometer with Cu Kα radiation of 1.5406 Å)

3.4.6 FOURIER TRANSFORM INFRARED SPECTROSCOPY (FTIR)

Fourier Transform Infrared Spectroscopy (FTIR) measurements were collected with a Shimadzu IR Tracer-100 apparatus. The scanning range was between 400 and 4000 cm^{-1}. The test is performed Attenuated total reflection (ATR).

TESTS FOR MICROSTRUCTURAL AND MORPHOLOGICAL ANALYSIS

3.4.7 SCANNING ELECTRON MICROSCOPY (SEM)

A JEOL JSM – 6490 Scanning electron microscopy (SEM) was used to observe the microstructure. The scanning was performed between 2θ of 5 to 70°, with a step size of 0.02°. Secondary electrons were used for a better definition of the surface texture.

THERMAL TESTS

3.4.8 HEATING TESTS

Heating tests were done in a Nabetherm GmbH 30-3000 °C LT 9/12P330 with air atmosphere

3.4.9 THERMAL GRAVIMETRIC ANALYSIS (TGA)

Tests for thermal gravimetric analysis (TGA) were performed in an TGA Q500 V20.8 Build 34. InstrSerial 0500-1190. Temperature range: (25ºC to 1000ºC). Control gases flow: Scale: N_2 → 10 ml/min Oven (optional): O2 → 90 ml /min; N2 → 90 ml/min; Synthetic air → 90 ml / min. Purge gas conditions Gas Purity Composition Moisture Nitrogen 99.995% N_2. Oxygen 99.980% O_2. Synthetic air 99.995% 20% O2 in N2 less than 3ppm H_2O, at a rate of 10, 15 and 20°C/min. For the thermal study, these heating speeds were chosen based on the review of the state of the art, with the precise aim of comparing with other nearby studies and also to establish that results depend on these heating speeds. Also, because at higher speeds it would be more of interest if one wanted to study the effects of thermal shock and not the behavior of a continuous increase in temperature. [105–110]

3.4.10 CREEP TESTS

High temperature compression tests were done in a self-made machine shown in the Figure. This equipment has an external sensor that measures the strains at a micrometric scale with the following functions and characteristics:
a) Zero setting at any position, b) ON/OFF button, c) Metric/Inch system interchange at any position, d) With data output interface. Characteristics: e) Power: One 1.5v SR44 battery, f) Operating temperature: 0°C ~ 40°C, g) Storage temperature: -20°C ~ 70°C, h) Relative humidity: ≤ 80%.

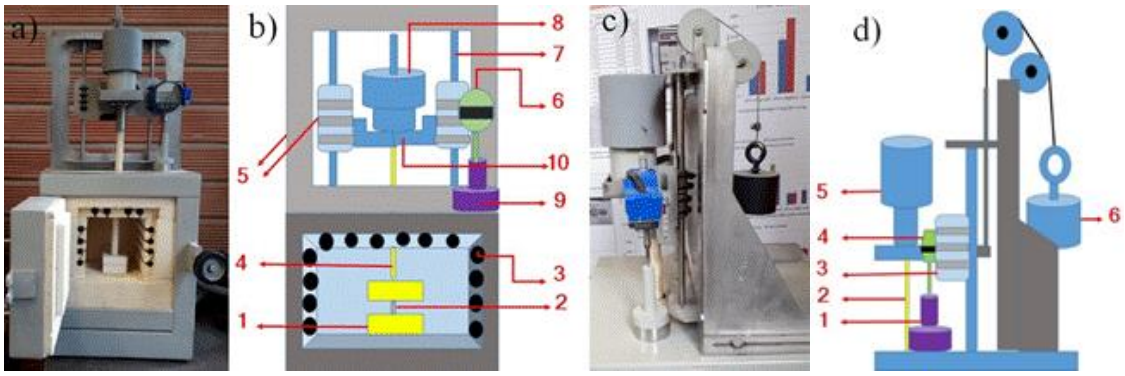

1. Alumina support with high melting point. 2. Sample submitted to creep tests. 3. Resistance generating high temperature. 4. Alumina rod. 5. Load slip train. 6. strain sensor. 7. Iron rod - sliding channel. 8. Weight that generates the stress of the test. 9. Support for sensor displacement needle. 10. Metallic load support of high temperature compression tests.

3.5 SOFTWARE AND SIMULATION TOOLS

3.5.1 HIGHSCORE PLUS

HighScore Plus. Version: 3.0 (3.0.5). Date: 30-01-2012. Produced by: PANAlytical B.V. Almelo, The Netherlands © 2012 PANAlytical B.V. All rights reserved. Licensed to: Universidad de Antioquia. License number: 10004909.

XRD test results were processed in this software. The software was used for phase identification and its chemical and mineralogical composition, phase quantification by the Rietveld method. Determine crystallite size and micro strains using the Williamson-Hall model.

3.5.2 MATLAB

R2016a licensed to Institución Universitaria de Envigado.
This software was used to make a program that fits the experimental curves with the creep curves using numerical nonlinear regression techniques. The parametric mathematical model of the theta projection method was implemented to fit the experimental curve.

3.5.3 EXCEL

Excel 2019. licensed to Institución Universitaria de Envigado.
This software was used to graph the curves and calculate the Weibull parameters from Weibull distribution in the damage analysis:

$$P_r(\sigma) = 1 - V_E \left(\frac{\sigma}{\sigma_0}\right)^m$$

σ : Applied stress
σ_0 : Characteristic stress
m : Weibull module
V_E : Effective volume
P_r : Fracture probability

This software was also used to generate some curves as:

- Density, porosity and absorption vs formulation.
- Compressive strength.
- Damage probability.
- Length crack vs formulation.
- Loss of Strength, Amount of Damage, Loss of Density, Crystallite Size and Micro strain vs formulation.
- Minimum creep rate, life time, activation energy creep and stress exponent vs formulation.

3.5.4 ORIGINLAB

OriginLab 2019- Trial version.

This software was used to reproduce the graph of the curves that are presented in the different chapters of this thesis, particularly the curves generated by XRD and FTIR tests.

3.5.5 RISK SIMULATOR

Risk simulator 2019. licensed to Institución Universitaria de Envigado.

This software was used to perform the Monte Carlo simulation in the damage analysis of the material. To perform the Monte Carlo simulation, the input data was associated with the Weibull distribution. The mathematical models used by the RISK Simulator are as follows:

Correlation coefficient:

$$r_{x,y} = \frac{n\sum x_i y_i - \sum x_i \sum y_i}{\sqrt{n\sum x_i^2 - (\sum x_i)^2}\sqrt{n\sum y_i^2 - (\sum y_i)^2}}$$

Where x and y represent the input data

Weibull distribution:

$$f(x) = \frac{\alpha}{\beta}\left[\frac{x}{\beta}\right]^{\alpha-1} e^{-\left(\frac{x}{\beta}\right)^{\alpha}}$$

Mean:

$$\beta\Gamma(1+\alpha^{-1})$$

Standard deviation:

$$\beta^2[\Gamma(1+2\alpha^{-1}) - \Gamma^2(1+\alpha^{-1})]$$

Asymmetry:

$$\frac{2\Gamma^3(1+\beta^{-1}) - 3\Gamma(1+\beta^{-1})\Gamma(1+2\beta^{-1}) + \Gamma(1+3\beta^{-1})}{[\Gamma(1+2\beta^{-1}) - \Gamma^2(1+\beta^{-1})]^{3/2}}$$

Excess kurtosis =:

$$\frac{-6\Gamma^4(1+\beta^{-1}) + 12\Gamma^2(1+\beta^{-1})\Gamma(1+2\beta^{-1}) - 3\Gamma^2(1+2\beta^{-1}) - 4\Gamma(1+\beta^{-1})\Gamma(1+3\beta^{-1}) + \Gamma(1+3\beta^{-1})}{[\Gamma(1+2\beta^{-1}) - \Gamma^2(1+\beta^{-1})]^2}$$

α is a form factor

β is a central location scale factor

Γ is the gamma function

Entry requirements: $\alpha \geq 0.05$, $\beta > 0$.

3.5.6 IMAGEJ

ImageJ 1.52v. Wayne Rasband. National Institute of Health, USA.
http://imagej.nih.gov/ij. JAVA 1.8.0_112 (64-bit). 3770K of 2987 MB (< 1%).
ImageJ is in the public domain.
This software was used to perform digital image processing and estimate the number and length of cracks in material damage analysis.

3.5.7 TA UNIVERSAL ANALYSIS

TA Instruments. Universal Analysis 2000.Version 4.5A Build 4.5.0.5.
Copyrigh©1998-2007 TA Instruments-Waters LLC. All rights reserved
Universidad de Antioquia.
This software was used to process the results of the TGA tests, calculate and graph the DTG curves as well as calculate the temperature intervals where changes are registered in the thermal reaction processes.

4. CHAPTER 4: STRUCTURE – PROPERTY – RELATIONS AND WEIBULL ANALYSIS OF CAC PASTES

Structure property relational and Weibull analysis of calcium aluminate cement pastes
Zapata, John F., Maryory Gomez, and Henry A. Colorado. "Structure-property relation and Weibull analysis of calcium aluminate cement pastes." Materials Characterization 134 (2017): 9-17. ISSN: 1044-5803. https://doi.org/10.1080/21650373.2020.1737593

4.1 INTRODUCTION

This chapter presents a complete characterization of the raw materials used in this thesis in its different compositions of CAC51wt%, CAC71wt%, CACP51wt% and CACP71wt%, including the quantification of their microstructure with XRD by Rietveld refinement, SEM, XRF, and FTIR. Density tests were also included. Additionally, a complete mechanical characterization by Weibull analysis is presented and curves were built with twenty samples per composition.

4.2 EXPERIMENTAL

Two types of CAC powders were investigated as shown in Table 6, from results obtained by X-ray fluorescence in a XRF Thermal spectrometer model OPTIM'X. Thus, cement raw powders were of two types, the first type has 52.12 wt% Al_2O_3, in this chapter will be known as CAC 51wt%. The second cement raw powder has 71.09 wt% Al_2O_3, named in this chapter as CAC 71wt%. Details of all other chemical components are presented in Table 6.

Table 6. Chemical composition of raw CAC powders

Sample	**Chemical Composition (wt%)**								
	Al_2O_3	**CaO**	**SiO_2**	**TiO_2**	**Fe_2O_3**	**K_2O**	**P_2O_5**	**ZrO_2**	**MoO_3**
CAC 51wt%	52.12	37.82	5.25	1.87	1.81	0.128	0.108	0.086	0.052
CAC 71wt%	71.09	28.38	0.238	–	–	–	–	–	–

In Table 7 is shown 2 types of cement paste samples fabricated in this research using two types of CAC powder with 0.4 and 0.5 W/C. Pastes were mixed mechanically while kept at 20°C. In order to avoid carbonation processes and interaction with environment, cement paste was poured in closed containers to air, and later removed from molds after 48 hours of curing. Sample dimensions were 19 mm diameter and 22 mm height.

Table 7. Formulations fabricated for cement paste samples

Samples	Cement type	Temperature (°C)	Curing time (hour)	Water/cement (W/C)
1	CACP 51wt%	20	48	0.4
2	CACP 51wt%	20	48	0.5
3	CACP 71wt%	20	48	0.4
4	CACP 71wt%	20	48	0.5

The compression tests were conducted in a universal Shimadzu Autograph apparatus at a cross head speed of 1mm/min. Sample dimensions were 19 mm diameter and 22 mm height. XRD characterization was done in a X'Pert PRO diffractometer with Cu Kα radiation of 1.5406 Å) for both cement raw powders and for the fabricated samples. The scanning was performed with 2θ between 5 and 70˚, with a step size 0.02°.

A JEOL JSM – 6490 Scanning electron microscopy (SEM) was used to observe the microstructure of the powders and cured cement samples. Secondary electrons were used for a better definition of the surface texture. Particle size distribution was also verified and the corresponding curves were draw.

Fourier Transform Infrared Spectroscopy (FTIR) measurements were collected with a Shimadzu IR Tracer-100 apparatus. The scanning range was between 400 and 4000 cm-1. The test is performed Attenuated total reflection (ATR).

Density tests, the density of water was taken to be 1.0 g/cm3. A set of 8 samples per composition was tested, and tests were conducted over some of the cylinders used for compression tests.

4.3 RESULTS

In *Figure 1* is shown XRD data for raw CAC powders with a) CAC 51wt.%, b) CAC 71wt%. It can be seen that the CAC 51wt% and 71wt% presents as the main phase calcium aluminate (CA) showing its peak of higher intensity in the angle 30.06. Additionally, the CAC 51wt% presents two secondary phases: Wadsleyite with a main peak in the angle 35.44 and a secondary peak in the angle 33.36; and Coesite with its main peak in the angle 28.933. Figure 1a for CAC 51wt%, most peaks corresponds to calcium aluminate, while the diffractogram shown in *Figure 1*b for CAC 71wt%, presents the contribution of two phases, CA and CA_2 [111]. Both XRD patterns look very similar. The CA_2 shows its peak main peak at 25.4˚

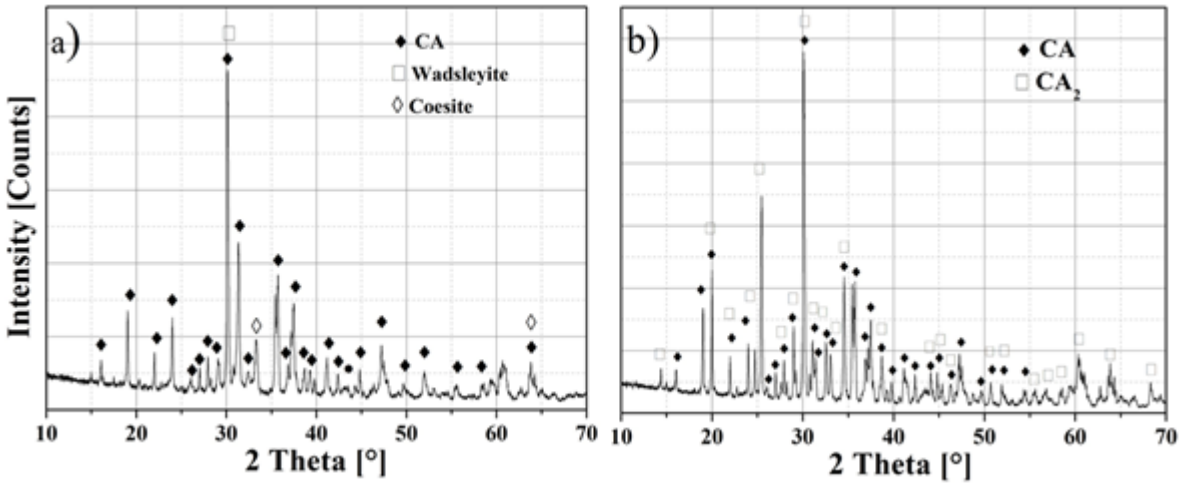

Figure 1. XRD for raw CAC powders with a) CAC 51wt%, b) CAC 71wt%.

The phases identified from these diffractograms are shown in Table 8.

Table 8. XRD analysis of raw cement powder for CAC (before hydration)

Sample	**Composition (wt%)**	**Phases**			
	Al_2O_3	(CA)	Wadsleyite	Coesite	(CA_2)
CAC 51wt%	51	$CaAl_2O_4$	Fe_5SiO_8	SiO_2	
CAC 71wt%	71	$CaAl_2O_4$	–	–	$CaAl_4O_7$

Wadsleyite (Fe_5SiO_8) and Coesite (SiO_2) were formed in crystalline form in CAC 51wt% (see Figure 1a), because the CAC 51wt% contains 5.25 wt% of SiO_2 and 1.81 wt% of Fe_2O_3 (see Table 6). The CAC 71wt% does not contain Fe_2O_3 and practically does not contain SiO_2, for that reason, these phases were not formed in this cement, (see Figure 1b).

Figure 2 shows the test results for raw powder XRD from CAC by Rietveld refinement: CAC 51wt% contains 95% CA, 2.6% Wadsleyite, and 2.1% Coesite, while CAC 71wt% contains 58.3% CA and 41.7% Grossite (CA_2).

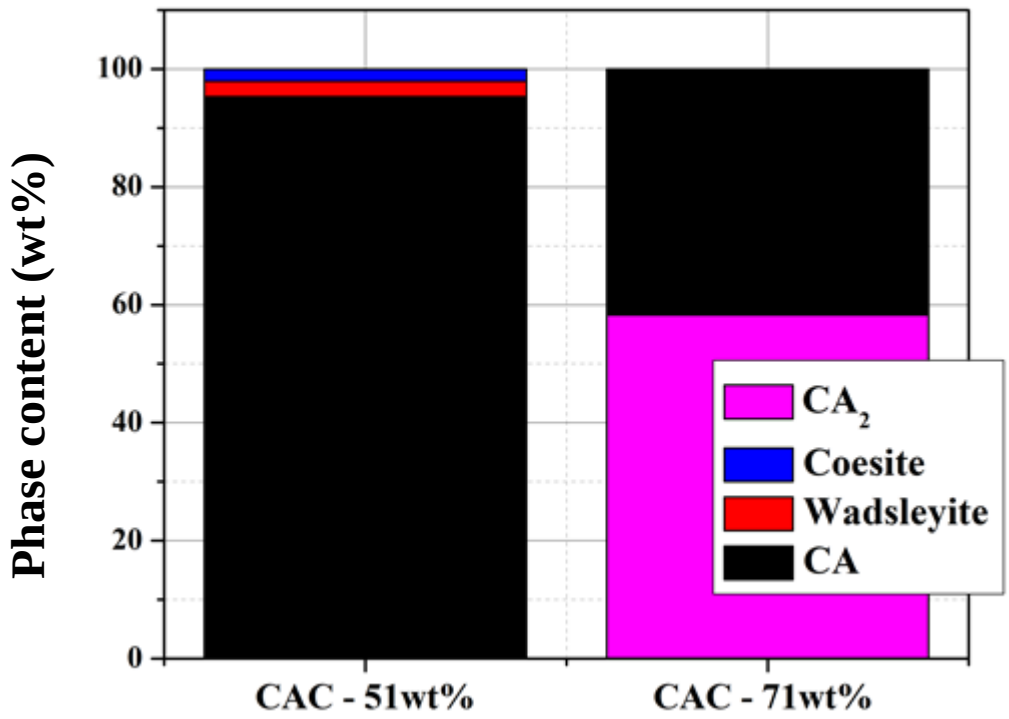

Figure 2. XRD Analysis using Rietveld refinement for CAC Powder.

The Rietveld refinement of the CAC 51wt% powder did not detect phases containing TiO_2, K_2O, P_2O_5, ZrO_2, MoO_3, which implies that these phases can be classified as an impurity due to the low content recorded by the XRF tests, see Table 6.

Figure 3 shows the SEM analysis results for raw powder from CAC. Figure 3a, CAC51 wt%, the arrow indicates calcium aluminate grains, which is the major mineral, in Figure 3b, CAC 71wt%, the arrow indicates calcium aluminate grains, which is the mineral phase that is formed for these contents of cements. There is concordance with the phases identified by XRD and XRF.

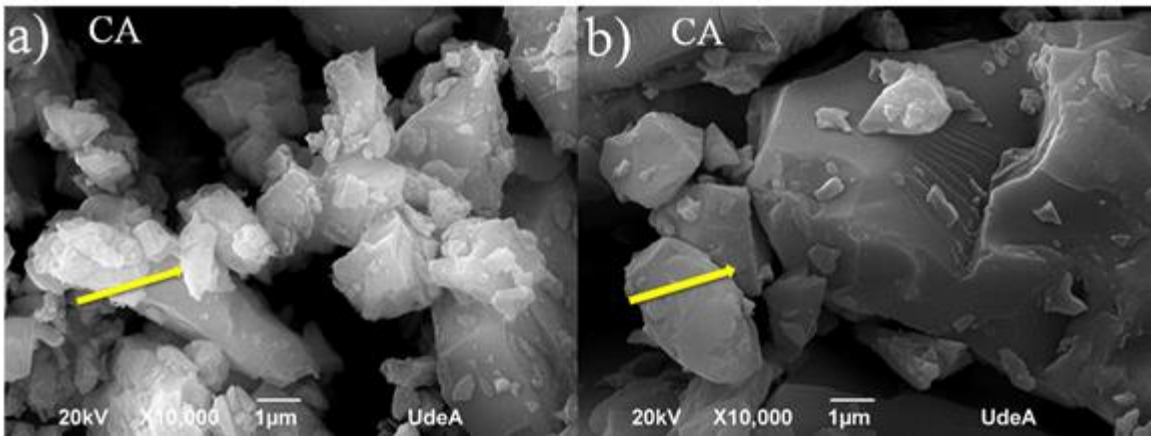

Figure 3. SEM raw powder cements a) CAC51 wt% Al_2O_3, b) CAC71 wt% Al_2O_3.

Figure 4 shows that calcium aluminate (CA) and dodecalcium heptaaluminate ($C_{12}A_7$) (Mayenite) has been formed in both cements. Both compounds of Mayenite and CA have common spectral features, but exhibit fingerprints that uniquely identifies each one of them. Characteristic transmittance bands of calcium aluminate cement powder phases reported in the literature and found in this work are summarized in the Table 9.

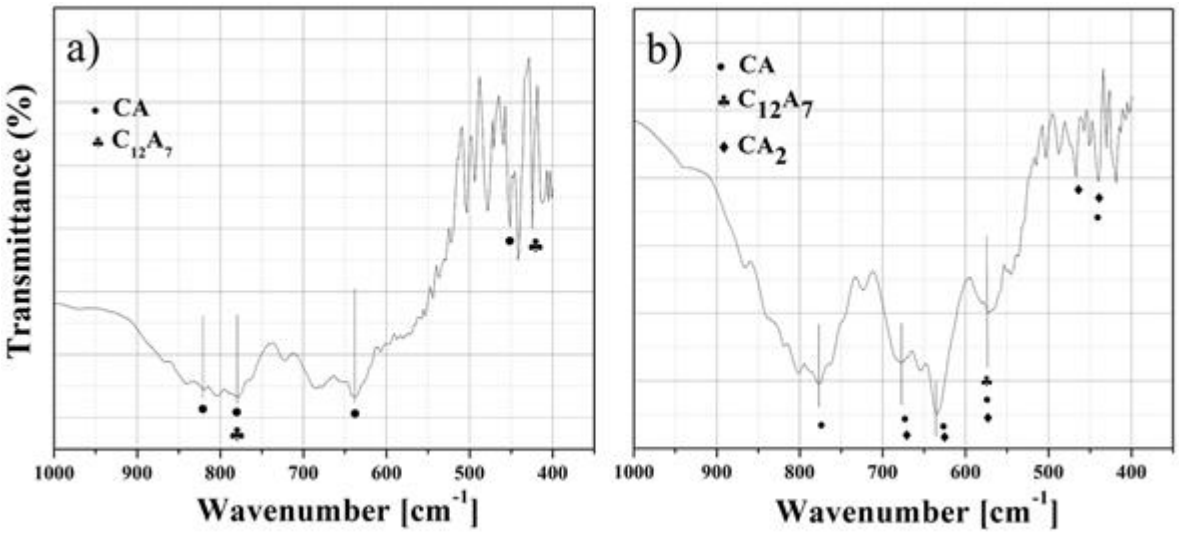

Figure 4. FTIR test results for raw powder a. CAC 51wt%, b. CAC 71wt%.

$C_{12}A_7$ appears because the ratio $Al_2O_3/CaO < 4$, for CAC 52% cement $Al_2O_3/CaO = 52.12/37.83 = 1.37$ and for CAC 71% cement $Al_2O_3/CaO = 71.09/28.38 = 2.50$ (see Table 6) [41].

$C_{12}A_7$ has a simple spectrum that is attributed to a cubic unit cell with polyhedral at lattice positions [112]. In this instance, the polyhedral arise from tetrahedral-coordinated aluminum with oxygen, the aluminum oxygen band stretches from which fall in the 700-900 cm^{-1} range [113]. Furthermore, the AlO_4 tetrahedral in $C_{12}A_7$ contain one non-bridging oxygen (NBO) atom that exhibits an infrared absorption near 855 cm^{-1} [113]. Such AlO_4 tetrahedral with at least one non-bridging oxygen are known as non condensed [114]. According to Tarte [114], the band at 855 cm^{-1} should be assigned to a condensed tetrahedral aluminum unit (where all comers are shared and no non-bonding oxygens exist), but this strong band is the only spectral feature that differs between $C_{12}A_7$ and CA, the latter of which is known to have all condensed tetrahedral. Furthermore, a non-bridging corner in a polyhedron has a strong extinction coefficient since the non-bridging oxygen, with a negative charge, is highly polarizable. Thus, the 855 cm^{-1} band should be properly assigned to non-bridging tetrahedral units in $C_{12}A_7$. The narrowness of the 855 cm^{-1} band is an indication of a uniform Al-O. It can be observed that only high alumina cements form CA_2. The deep reasons why this occurs are explained in Chapter 5.

Table 9. Characteristic absorbance bands of calcium aluminate cement powder phases

Phase	Fundamental vibration (cm^{-1})	Reference
CA	840, 805, 780, 730, 720, 680, 640, 570, 540, 450, 420	[115,116]
	CAC 51wt%: 804, 778, 451. CAC 71wt%: 776, 67, 640, 573, 420	This work
$C_{12}A_7$	850, 780, 610, 575, 460, 410	[115,116]
	CAC 51wt%: 413. CAC 71wt%: 573	This work
CA_2	945, 920, 860, 840, 810, 745, 680, 660, 640, 575, 540, 440, 422	[115]
	CAC 71wt%: 677, 640, 573, 440, 420	This work

Figure 5 shows the results of XRD tests. a) CACP 51wt% - W/C = 0.5, b) CACP 71wt% - W/C = 0.5, c) CACP 51wt% - W/C = 0.4, d) CACP 71wt% - W/C = 0.4.

It can be seen in the Figure 5a, presents as the main phase of CAH_{10}, showing its peak of higher intensity in the angle 39.35 and a secondary peak in the angle 17.32. Additionally, presents two secondary phases, one of C_2AH_6 showing its peak of higher intensity in the angle 39.35 and a secondary peak in the angle 17.32 and another phase is AH_3 showing its peak of higher intensity in the angle 31.02 and a secondary peak in the angle 21.24. Figure 5b, presents as the main phase of CAH_{10} showing its peak of higher intensity in the angle 39.35 and a secondary peak in the angle 17.32. Additionally, presents three secondary phases, C_2AH_6, AH_3 and C_3AH_8. All showing its peak of higher intensity in the angle 18.42. Figure 5c, presents as the main phase of CAH_{10}, showing its peak higher intensity in the angle 39.43. Additionally, presents two secondary phases, one of C_2AH_6 and another phase of AH_3, both showing its peak higher intensity in the angle 18.60.

Finally, the Figure 5d, presents as the main phase of CAH_{10}, showing its peak higher intensity in the angle 39.43. Additionally, presents three secondary phases, C_2AH_6, AH_3 and C_3AH_8 showing their peaks of higher intensity in the angles of 18.70; 32.18 and 18. 70 respectively. The phases identified from these diffractograms are shown in Table 10.

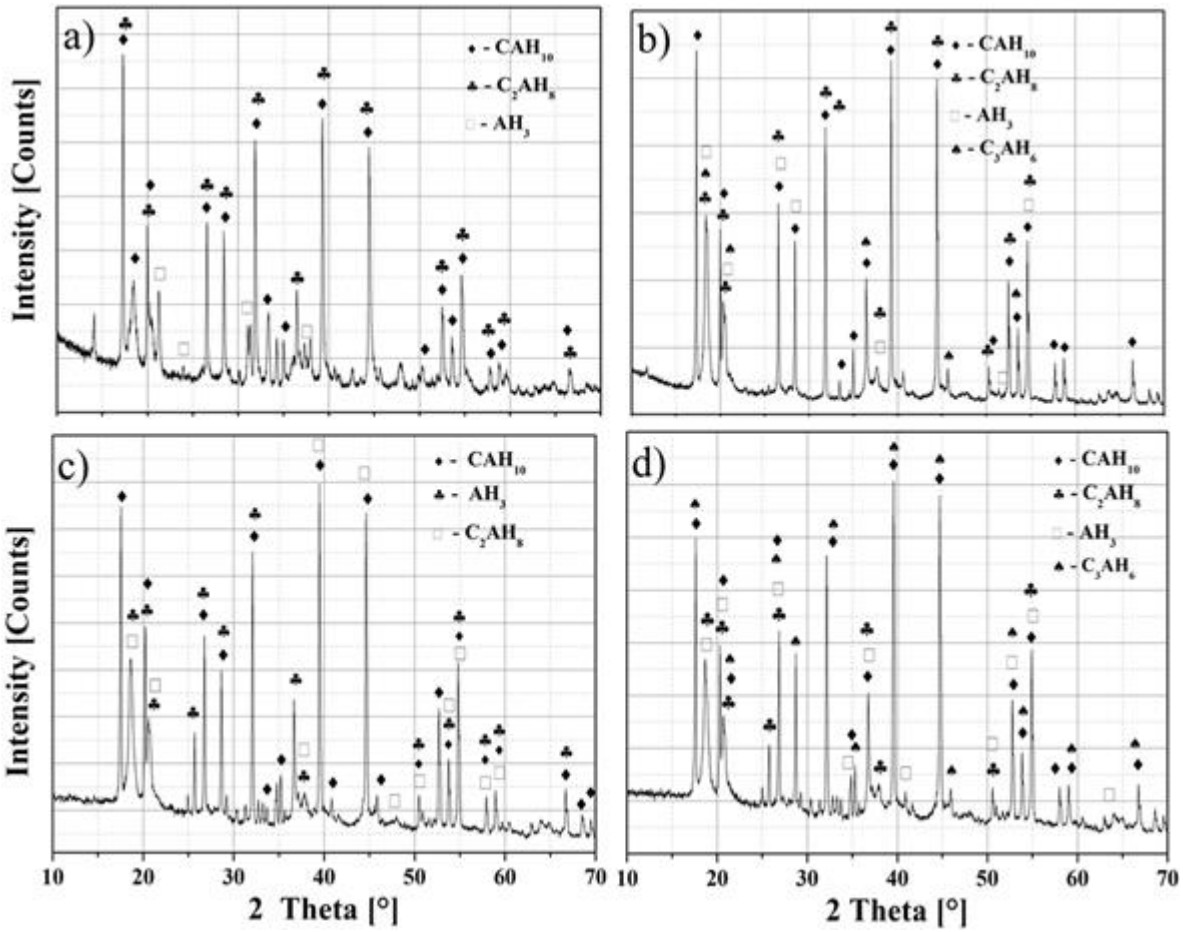

Figure 5. XRD: CACP-51wt%. a) W/C=0.5, c) W/C=0.4. CACP-71wt%: b) W/C=0.5, d) W/C=0.4.

Table 10. XRD Analysis for Calcium Aluminate Cement Paste

Sample			Phases			
See Figure 6	wt% Al_2O_3	W/C	CAH_{10}	C_2AH_8	AH_3	C_3AH_6
I	51	0.5	$CaAl_2O_{14}H_{20}$	$Ca_2Al_2O_{13}H_{16}$	$Al(OH)_3$	–
II	71	0.5	$CaAl_2O_{14}H_{20}$	$Ca_2Al_2O_{13}H_{16}$	$Al(OH)_3$	$Ca_3[Al(OH)_6]_2$
III	51	0.4	$CaAl_2O_{14}H_{20}$	$Ca_2Al_2O_{13}H_{16}$	$Al(OH)_3$	–
IV	71	0.4	$CaAl_2O_{14}H_{20}$	$Ca_2Al_2O_{13}H_{16}$	$Al(OH)_3$	$Ca_3[Al(OH)_6]_2$

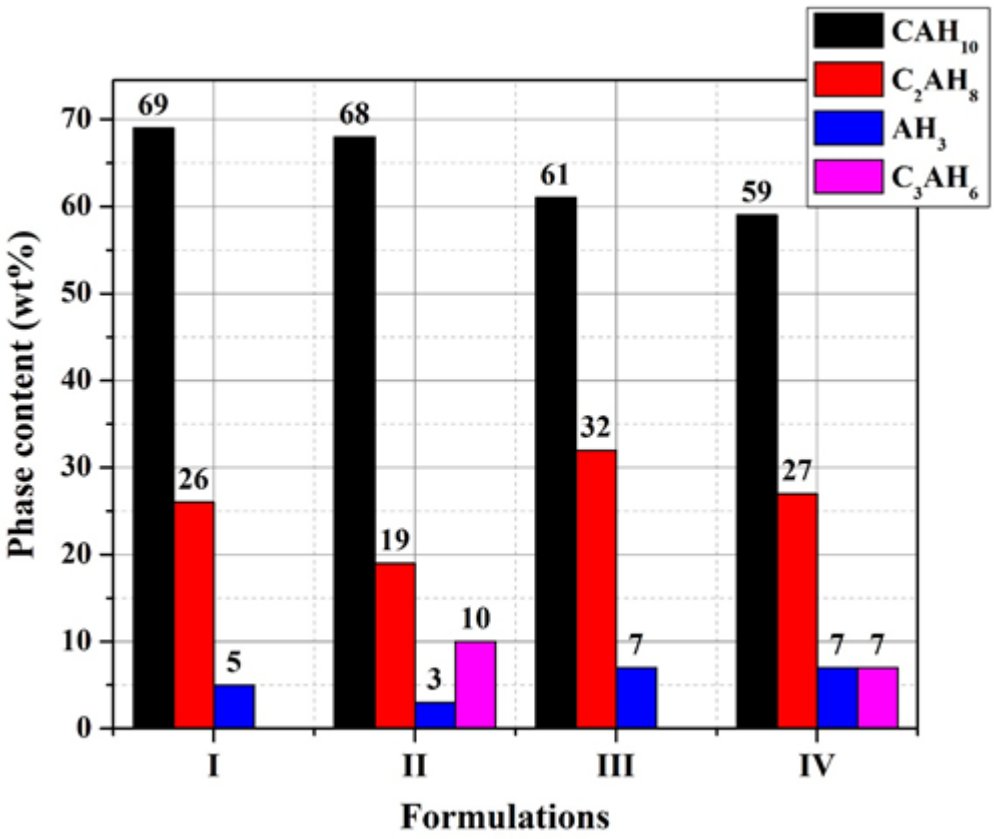

Figure 6. XRD Analysis using Rietveld refinement for Calcium Aluminate Cement Pastes.

The usual crystalline form of AH_3 from the hydration or conversion of CAC is gibbsite. It has been indicated [117] that an acid environment favors the crystallization of the gibbsite, a neutral CAH_{10} and a basic C_3AH_6. In a high pH of the solution would favor C_3AH_6 formation more than gibbsite formation, as can be seen in formulation II and IV in Figure 6. However, it must be considered that C_3AH_6, as its ages, can become AH_3. This may explain that it is normally the gibbsite that is normally found in the cement paste [117].

CACP-51wt% and CACP-71wt% and W/C=0.5 were analyzed by SEM and presented in Figures 7a and 7b and with W/C=0.4, presented in Figure 7c and 7d. As can be observed in all formulations, the phases were formed in the form of hexa-aluminates, this is fundamentally due to the temperature of hydration in our study is 20 °C. The arrow indicates calcium aluminate decahydrate in the form of CAH_{10} (Figure7a, 7b and 7d) and C_2AH_8 (Figure 7c). This is in agreement with the phases identified by XRD.

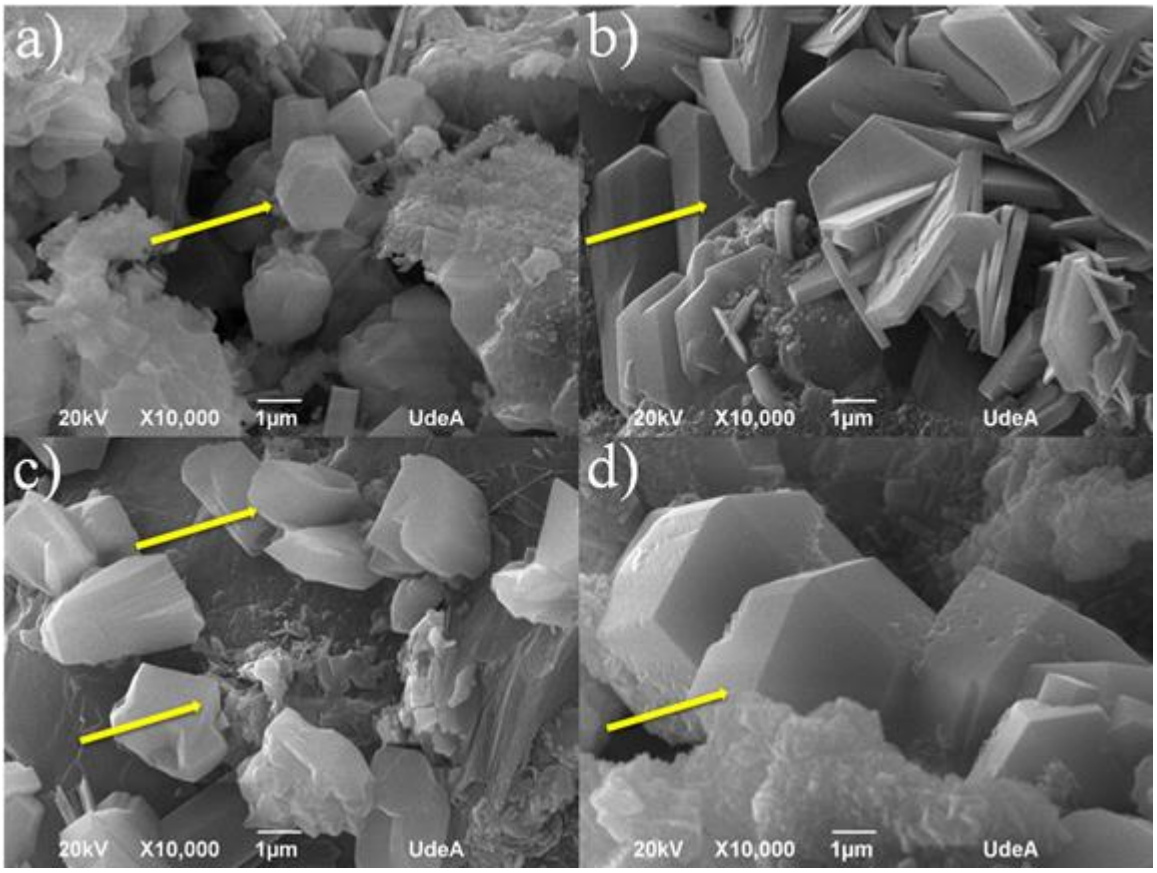

Figure 7. SEM images CACP 51wt%:
a) W/C=0.5, c) W/C=0.4. CACP 71wt%: b) W/C=0.5, d) W/C=0.4

Figure 8 shows the results of FTIR tests for CACP and characteristic transmittance bands reported in the literature. Figure 8 reveals the formation phases of CAH_{10}, C_2AH_8 and C_3AH_6. In general, is observed that all the formulations several have identical hydrated phases, this mainly because all the formulations were hydrated at the same temperature of 20 ° C.

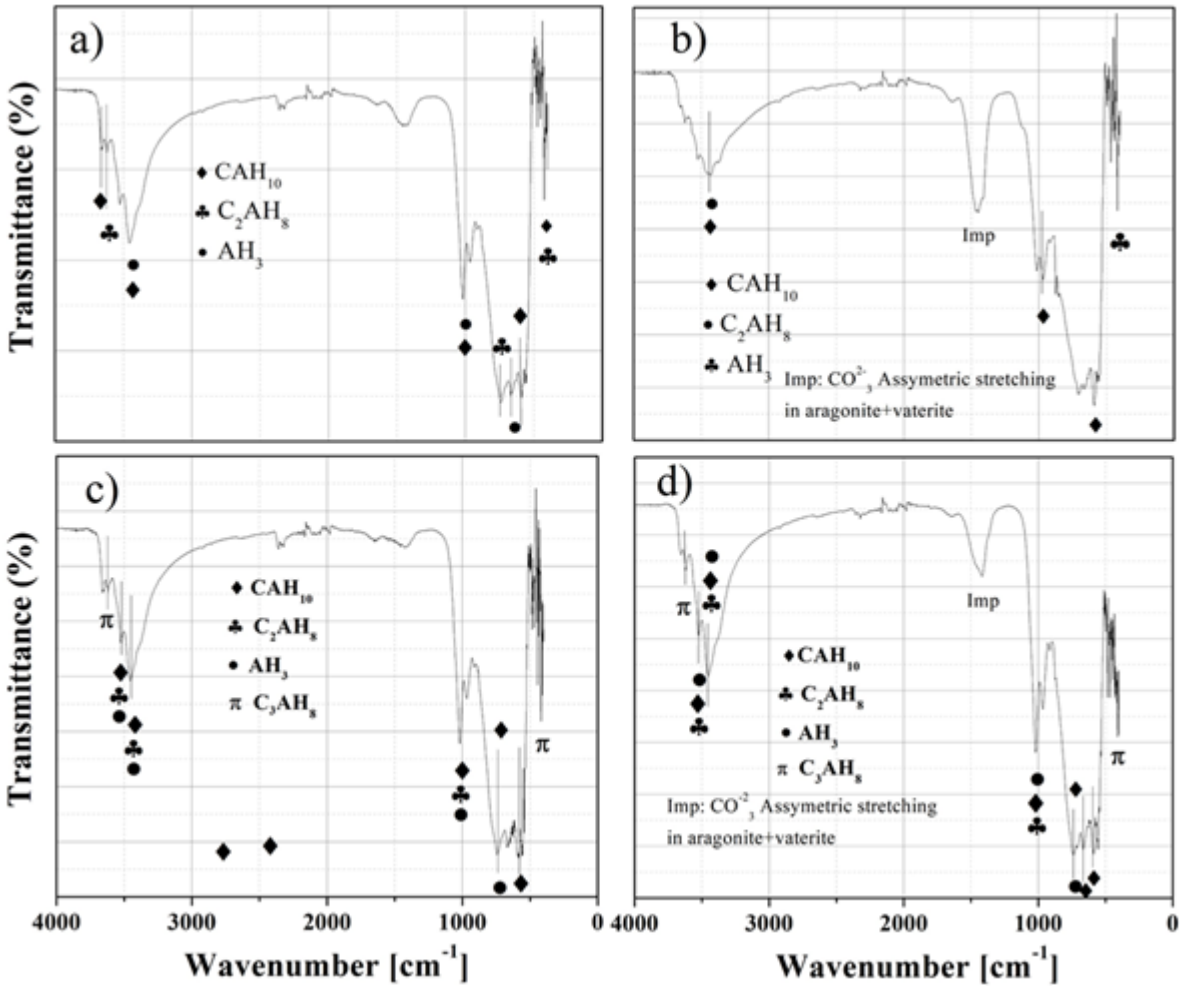

Figure 8. FTIR test results for CACP. CACP 51wt%:
a) W/C=0.4, b) W/C=0.5. CACP 71wt%: c) W/C=0.4, d) W/C=0.5

Figure 9 shows a relation of the bands of most interest, according to some authors and in this work.

Table 11. Characteristic transmittance bands of CACP phases

Phase	Fundamental vibration (cm^{-1})	Reference
CAH_{10}	3500, 3460 – 3380, 1100 – 850, 556, 524, 520, 420	[118,119]
	420 (CACP51wt%-W/C=0.4), 3439 (CACP51wt%-W/C=0.5), 3451 (CACP 71wt% A-W/C=0.4)	This work
	3680–3600, 3680–3520, 3475–1600, 1145–1115, 1020–970, 775–730, 670–590, 565–535, 425–415	[120]

CAH_{10}	3653, 1019, 587 (5104), 962, 586 (CACP51wt%-W/C=0.5), 3525, 1026, 740, 585 (CACP 71wt% A-W/C=0.4). 3518 (CACP 71wt% A-W/C=0.5)	This work
C_2AH_8	3465, 1100–850, 535–520 (Overlapping bands) 530-420	[115,120,121]
	420 (CACP51wt%-W/C=0.4), 3658 (CACP51wt%-W/C=0.5)	This work
C_2AH_8	3670, 3665, 3540, 3495, 1650, 1015, 910, 740, 595 – 535, 524, 420	[115,119,121,122]
	739, 420 (CACP51wt%-W/C=0.4), 740 (CACP 71wt% A-W/C=0.4), 1015, 743 (CACP 71wt% A-W/C=0.5)	This work
C_3AH_6	3670, 3600-3400, 700, 524, 412, 400	[115,120,121]
	3665	[121]
AH_3	3620, 3521, 3455, 3380,1020, 668, 560, 450	[120]
	3361, 3378, 3428, 3518. 3616, 1020, 967	[113]
	3685, 3613, 3520, 3445, 3390, 3372	[114]
	3630, 3530, 3475	[121]
	3457, 1019, 663 (CACP51wt%-W/C=0.4), 3439 (CACP51wt%-W/C=0.5), 3525, 3451, 1026 (CACP 71wt% A-W/C=0.4), 3616, 3518, 3455 (CACP 71wt% A-W/C=0.5)	This work

Part of the water contained in the hydrated hexagonal calcium aluminates, CAH_{10}, is weakly bounded [115]. Frequently, CAH_X, C_2AH_z and C_4AH_Y take values of X=10, Y=8, and Z=13. These molecules can lose small amounts of water without significantly changing their structure. This type of bond is involved in transformation from the hexagonal forms.

In the case of CAH_{10} which is the main hydration phase at 20 °C, the FTIR represent these variations of water losses without changing the structure, mainly in the zones corresponding to O-H stretching vibrations (between 3000-4000 cm^{-1}) and bend vibrations H-O-H (Between 1,600 -1,700 cm^{-1}), [123]. See Table 11 and Figure 8.

Figure 8 also shows a very intense and wide band for the CAH_{10} phase for all the formulations studied in this work, which is associated with O-H valence vibrations in the region of 3525-3653 cm^{-1}, with its maximum absorption at 3653 cm^{-1}. At 1026 cm^{-1} (CACP 71wt%-W/C = 0.4), see Figure 8b, and at 1019 cm^{-1} (CACP 51wt%-W/C = 0.5), see Figure 8c, a weak band appears. This is associated with the bend vibrations H-O-H. The absorption at these frequencies is due to carbonates produced by atmospheric CO_2 contamination [115].

The region of the spectrum corresponding to the region 1200-400 cm^{-1} presents bands of very low intensity, which in this case may indicate little crystallinity. However, bands can be

identified at 420 (CACP 51wt%-W/C = 0.4), see Figure 8a; and 1026, 740, 585 (CACP 71wt% -W/C=0.4), see Figure 8c.

In the case of C_2AH_8 which is the second main hydration phase at 20 ° C presents absorption band very intense bands at 3658 (CACP 51wt%-W/C=0.5) as shown in Figure 8c for the vibrations O-H of water molecule. The region of the spectrum corresponding to the region 1.200-400 cm^{-1} presents bands of very low intensity: At 739 and 420 for the CACP 51wt% - W/C =0.4. And at 740 for the CACP 71wt%- W/C =0.4; 1015, 743 (CACP 71wt%- W/C =0.5).

AH_3 shows an intense and characteristic peak at 3457 cm^{-1} (CACP 51wt%- W/C =0.4), 3439 cm^{-1} (CACP 51wt% - W/C =0.5), 3525 cm^{-1} (CACP 71wt% - W/C =0.4), 3616 cm^{-1} (CACP 71wt% - W/C =0.5). Figure 8.

Bayerite shows an intense and characteristic peak at 3455 cm^{-1} (CACP 71wt% - W/C =0.5) Figure 8d and the CAH_{10} shows an intense and characteristic peak 3623 cm^{-1} (CACP 51wt%- W/C =0.4), 3525 cm^{-1} (CACP 71wt% - W/C =0.4) Figure 8c. Figure 9 shows compression strength and density results for the CACP samples. As can be observed, CACP has an average density of 1.9 g/cm^3 and higher alumina content gives higher strengths, ranging from 14 to 35 MPa after 28 days of curing.

Figure 9a is a summary of the mean compression strength for all formulations investigated (see Table 12), showing that samples with CACP 71wt% - W/C =0.4 has the better results, which is expected since both higher alumina contents and lower W/C contribute to better strength results. Samples with CACP 51wt% do not show significant differences in compression tests. Density tests in Figure 9b shows that as water contents increases, density decreases, and as alumina content increases, density decreases as well. This last result is obtained because samples with CACP 71wt% (C_3AH_6), which decreases the strength of the samples and increases the porosity [51].

Table 12. Formulations

I	II	III	IV
CACP 51wt%-W/C=0.4	CACP 51wt%-W/C=0.5	CACP 71wt%-W/C=0.4	CACP 71wt%-W/C=0.5

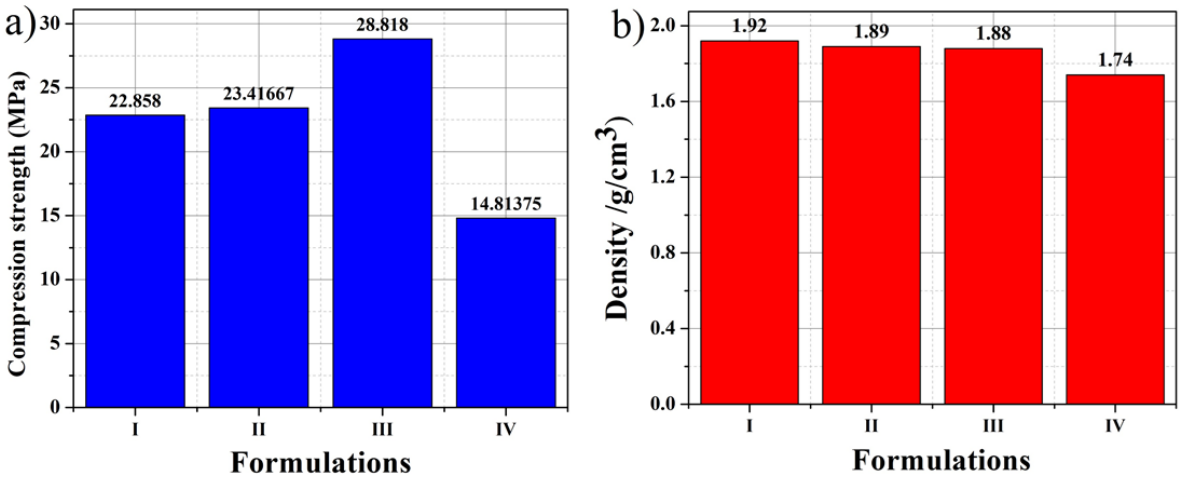

Figure 9. Mechanical tests: a) Compression strength, b) Density.

Figure 10 shows the Weibull analysis results for CACP samples (see Table 13). Weibull distributions from Figure 10a, revealed a compression change from about 10 to 45 MPa, with Weibull moduli ranging between 2.7 and 3.8, which is typical for cement-based materials (see Figure 10c) [124].

There are some curve overlaps, but in general, as the alumina content increased, the strength increased. The Weibull curve with CAC 71wt% - W/C=0.4 showed disruptive results, as it is separated from all others by about 5 to 10 MPa. The corresponding linear equations used to obtain the modulus are presented in Figure 10b, and the corresponding slope and the Weibull moduli as a function of the cement paste composition are plotted in Figure 10c. Upon optimization of the manufacturing processes or the use of chemical admixtures, these values can be increased, and the corresponding compression strength variation decreased (Weibull modulus increased).

Table 13. CACP samples

51A-04W	51A-05W	71A-04W	71A-05W
CACP 51wt%-W/C=0.4	CACP 51wt%-W/C=0.5	CACP 71wt%-W/C=0.4	CACP 71wt%-W/C=0.5

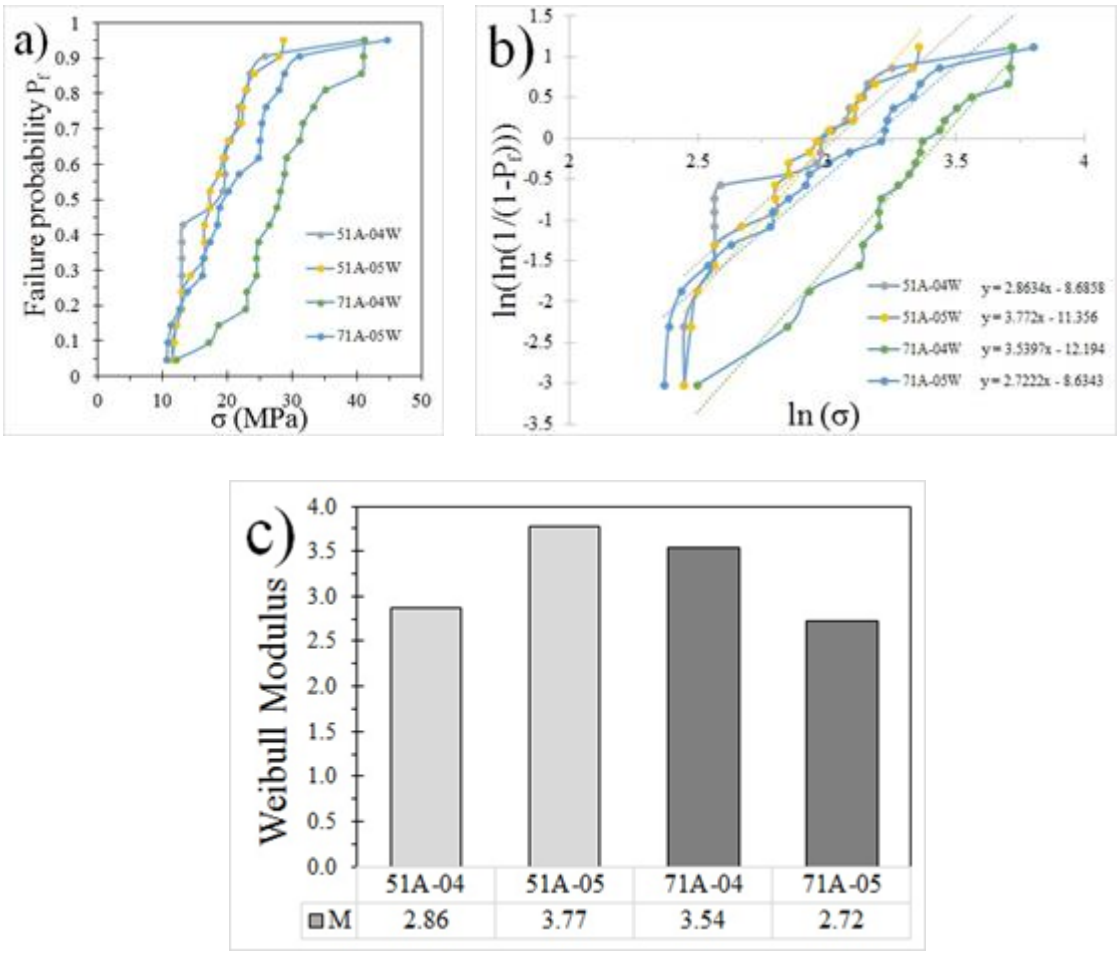

Figure 10. Weibull statistics results for compression strength tests.

4.4 DISCUSSION

This paper has presented a complete characterization of CAC and CACP, and more specifically in the microstructure and mechanical behavior. In this last part, Weibull distributions over the compression tests showed a high variability on results, which is certainly reflected in the Weibull modulus. CAC are very reactive when compared with traditional hydraulic cements, which is shown in the significant impact of temperature of phase formation and in the conversion phenomena [125]. This high reactivity leads in an early strength, which is very useful in many applications because can reduce manufacturing time, which is a significant factor when construction and building materials are selected [126].

Although is well known that this cement has a bad reputation after the Spain issue with the massive construction with CAC, nowadays is accepted that keeping a low W/C ratio, the processing temperature, and pH, the conversion reaction can be avoided [111,125]. Therefore, many applications and even CAC modifications could move cement industry towards the use of CAC for specific applications [125].

The CO_2 emissions associated with the manufacture of hardened concrete objects or structures can be divided in three main contributions [127]:

- The CO_2 emissions associated with the raw materials (cement, aggregates, water, etc.)
- The CO_2 emissions associated with the production of the energy used in concrete mixing.
- The CO_2 emissions associated with the delivery of both the raw materials and the fresh concrete and the placing and finishing of the concrete.

The clinker of Portland cement (PC) is the highest producer of CO_2 when is compared to other hydraulic cements [127], including CAC. These emissions are due to the high content of basic calcium content, which is usually derived from limestone calcination, resulting in the release of one mole of "fossil CO_2" per mole of CaO in the clinker [127]. The current global cement and concrete standards allow the use of various "supplementary cementitious materials" (SCM) as substitutes for cement and concrete clinker [127] in order to reduce CO_2 footprint, such as the alumina-rich pozzolans present in CAC cements, and therefore these cements can be tailored to reduce CO_2 emissions [127].

Thus, aluminous cements are a strong candidate for reducing CO_2 emissions in cement industry. Therefore, CAC cements are not only good for refractory and structural applications because of their high early resistance and because of its high resistance to chemical attacks, but also they are beneficial because they are more environmentally friendly [125]. The complex microstructure presented in this paper as the phases shown in Figure 7 reveal a great opportunity to modify these materials for the environmental challenges that environment today is requiring from cement and other building materials industries.

4.5 CONCLUSIONS

At higher W/C, higher compression resistance was obtained, which is associated to as much formed Hydrogarnet. The higher compression was about 25MPa which enables this material for it is used in a variety of civil constructions. The Hexagonal hydrated phases found via XRD and SEM were CAH_{10} and (C_2AH_8).

5. CHAPTER 5: CRACKING IN CALCIUM ALUMINATE CEMENTS PASTES INDUCED AT DIFFERENT EXPOSURE TEMPERATURES

Zapata, John F., Maryory Gomez, and Henry A. Colorado. "Cracking in Calcium Aluminate Cement Pastes Induced at Different Exposure Temperatures." Journal of Materials Engineering and Performance 28.12 (2019): 7502-7513. https://doi.org/10.1007/s11665-019-04466-5

5.1 INTRODUCTION

There is a lack of research about the behavior of calcium aluminate cements during high-temperature conditions. Recently, Wasim, et al [128] investigated CAC concrete (the study was limited to CA-50 calcium aluminate cement mixed with limestone crushed sand as fine and coarse aggregate respectively) exposed to 23, 200, 400, 600 and 800 °C. In this study, CAC concrete was compared to traditional ordinary Portland cement (OPC). When the materials were exposed to high temperatures, their compression strength decreases. However, CAC concrete showed a lower loss of compression strength when compared to traditional concrete if the temperature is kept below 600 °C. For higher temperatures, the deterioration in strength was similar for both materials. Similarly, the modulus of elasticity also decreased in both materials as the exposure temperature increased. Regarding the modulus of elasticity, at temperatures below 400 °C, the CAC concrete showed worse performance when compared with traditional PC concrete. This is mostly attributed to the increase in the porosity because of the conversion reaction described below. However, at temperatures over 400 °C, CAC concrete showed significant improvements of 32 and 44% for 600 and 800° C, respectively. This improvement is mostly attributed to the higher contents of alumina in the CACs.

Another important study on the behavior of CAC at high temperature was carried out by Cardoso et al [30]. When CAC pastes were heated up, the free and bonded water was removed and the corresponding dehydration followed equations 1 to 4 [30]. Following the sequence equations, firstly, unbounded water from the AH_3 gel (which has an amorphous structure) was removed at 100 °C, while CAH_{10} was dehydrated at about 120 °C. Later, C_2AH_8 was dehydrated at 200 °C, and similarly gibbsite was dehydrated at 300 °C. For CAC 71wt% and water to cement ratio (W/C) of 1.0, the crystalline hydrate C_3AH_6 started to decompose at 300 °C. Table 14 summarizes both the dehydration temperatures and reactions. These reactions and results [30] have been confirmed by Antonovič et al [38], who also established that after the dehydration process $C_{12}A_7$ is formed at temperatures between 500 and 800 °C. At 1000 °C, $C_{12}A_7$ is converted to CA or to CA_2. Further investigation [19] over the dehydration process of C_2AH_8 have revealed a very complex process which has been explained as a three steps phenomena of losing molecules: three molecules at 110 °C, one molecule at 170 °C, and four molecules at 300 °C.

$$CAH_{10} \rightarrow C_2AH_8 + AH_3 \quad (6)$$

$$C_2AH_8 + AH_3 \rightarrow C_3AH_6 + 2AH_3 \quad (7)$$

$$C_3AH_6 + 2AH_3 \rightarrow C_{12}A_7 + CA + H \quad (8)$$

$$C_3AH_6 + 2AH_3 + A \rightarrow CA + H \quad (9)$$

Regarding the damage generated in cements caused by high temperature in cements, previous research shows two main approaches that relate fracture to temperature changes: the thermoplastic and the energy balance approaches. In the thermoplastic approach, a fracture will occur if the resulting thermal stresses overcome the fracture strength of the material. The stresses appear in the material after a decrease in temperature [3,129–132]. The energy balance approach, has been studied by Hasselman [132], who found that the fracture that occurs due to thermal changes result in a critical stress that initiates damage.

This critical stress depends on the elastic energy stored in the material at the time the damage is initiated [133]. The main problems with the models that are generated in these two approaches is that as temperature changes, they assume constant values for some of the key material properties, such as the Poisson ratio, Young's modulus and thermal conductivity. These models do not consider the phase-dependent properties involved in many systems for which temperature causes a complex interaction between the phases [133].

Table 14. CAC behavior with the increase in temperature [38]

Temperature range (°C)	Dehydration reaction
60 - 120	$AHx \rightarrow A + xH$
110 - 170	$3CAH_{10} \rightarrow C_3AH_6 + 2AH_3 + 18H$
170 - 240	$3C_2AH_8 \rightarrow 2C_3AH_6 + AH_3 + 9H$
210 - 300	$AH_3 \rightarrow A + 3H$
240 – 370	$7C_3AH_6 \rightarrow C_{12}A_7H + 9CH + 32H$
≈ 450	$CH \rightarrow C + H$
≈750	$C_{12}A_7H \rightarrow C_{12}A_7 + H$
≈900	$C_{12}A_7 + 5A \rightarrow 12CA$

Additionally, Lu and Fleck [134] analyzed the thermal shock in fragile solids using a fracture criterion which is based on the stress on a plate. The plate contained a distribution of defects (such as pore distribution) and an intensity factor criterion, which had a dominant crack aligned in the thickness direction. Collin and Rowcliffe [135] investigated the thermal shock in fragile materials using an indentation method, which generates cracks that grow as a function of temperature and allows the thermal shock to be predicted. Bahr et al. [136,137] investigated patterns of cracks related to thermal shock.

Jenkins [138] used an energy minimization method to determine the cracks separation and penetration due to temperature changes. Bourdin et al. [139] used a variational approach to describe fracture as a function of temperature, which included the growth and propagation of cracks, and presented predicting algorithms that calculate cracks induced by thermal stresses [140] in fragile materials. It is well understood that if complex materials such cements are

subjected to significant temperature changes, they can experience not only physical changes (such as shrinkage and cracking), but also complicated phase transformations and chemical deterioration.

These multivariable problems have been poorly explored mainly due to their extreme complexity, which is shown by the limitations in the available theories. These limitations have also been described before for more simple refractory ceramic materials such as bauxites, magnesia and alumina [141]. Such complexities have meant that most research is carried out in the form of experimental studies using statistic methodologies, and in some cases, using digital image analysis. On the other hand, multiple techniques have been used successfully to quantify the damage in concrete and derived materials regardless of whether this damage is generated by temperature changes or by other reason. These include two-dimensional techniques such as acoustic waves [142,143] and optical and electron microscopies [12,144]. Three dimensional techniques such as computer tomography using different scales [145,146], have been used on concrete to detect micro-cracks and carry out pore structure characterization [147,148] or to study damage evolution [145,149].

To date, no quantitative analysis has been conducted for crack patterns induced by thermal shock in CACs [142]. Therefore, the main purpose of the present investigation is to contribute to the literature on crack generation and quantification for CACs, using an experimental approach combined with numerical analyses of crack patterns, induced by temperature. The mixture of these experimental and numerical analyses aims to optimize a simple and inexpensive methodology for further study multivariable complex systems that includes cementitious materials, concrete, and ceramic composites exposed to high temperatures.

Previously, alternative methodologies developed to evaluate crack damage in traditional cements with additives after exposure to high temperatures have shown crack damage reduction. One case used the addition of PFA (pulverized fuel ash) to evaluate damage in combination with tensile and compressive tests[150]. Other example is using nano kaolin as additive, and the high temperature properties also improved [151]. The main contribution of this study is the use of a new methodology to quantify calcium aluminate cement paste (CACP) damage caused by exposure to high temperatures. It will evaluate how alumina content, W/C, and temperature affect CACP damage at high temperatures. Digital image processing was used to quantify the damage by taking into the account factors such as temperature (500, 800 and 1000 °C), for CACP 51wt% (CACP with 51wt% alumina) (wt% weight percentage) and CACP 71wt% (CACP with 71wt% alumina) and W/C = 0.25, 0.3 and 0.4. Weibull distribution analysis and Monte Carlo simulations were used as well. As explained before, there is a lack of research in the literature regarding quantification of the damage of these cements when submitted to high temperatures.

5.2 MATERIALS AND METHODS

The following characterizations were used in this research in order to quantify the microstructure of CAC: SEM, FTIR, XRF and XRD. Two types of CAC powders were investigated: CAC 51wt% and CAC 71wt%. The composition of these powders was obtained

in a XRF Thermo spectrometer Model OPTIM'X. Details of all chemical components are presented in Table 15.

Table 15. Chemical composition of raw CAC powders

Samples	Chemical Composition (wt%)								
Cement type	Al_2O_3	CaO	SiO_2	TiO_2	Fe_2O_3	K_2O	P_2O_5	ZrO_2	MoO_3
I. CAC 51wt%	52.12	37.82	5.25	1.87	1.81	0.128	0.108	0.086	0.052
II. CAC 71wt%	71.09	28.38	0.238	-	-	-	-	-	-

These two types of CAC were fabricated with three water to cement ratio (W/C): 0.25, 0.3, and 0.4, as summarized in Table 16. All cement pastes were made at 20 °C and were kept closed to air contact for 48 h (in order to avoid pre-carbonation), and then released from their molds and put in water for hydration. Thereafter, samples were removed from the water and left to dry in the air for 24 h.

Table 16. Cement paste samples fabricated formulations

Samples	Cement type	Temperature (°C)	Water/cement (W/C)
1	I, II	20	0.25, 0.3, 0.4
2	I, II	500	0.25, 0.3, 0.4
3	I, II	800	0.25, 0.3, 0.4
4	I, II	1000	0.25, 0.3, 0.4,

Sample dimensions were 19 mm in diameter and 22 mm in height. XRD characterization was done in an X'Pert PRO diffractometer with Cu K_α radiation of 1.5406 Å. The scanning was performed between 2θ of 5 to 70°, with a step size of 0.02°. For the XRD interpretation. A JEOL JSM – 6490 scanning electron microscopy with energy-dispersive x-ray spectroscopy (SEM-EDS) was used to observe the microstructure of powders and cured cementitious samples. Secondary electrons were used for a better definition of the surface texture. Fourier Transform Infrared Spectroscopy (FTIR) measurements were conducted in a Shimadzu IRTracer-100, with a scanning range 400-4100 (cm^{-1}): Samples were heated up from 20 °C to 500 °C, 800 °C, and 1000 °C, at a temperature ramp of 14°C/min. After being exposed for 1h to these temperatures in a furnace Nabetherm GmbH 30-3000 °C LT 9/12P330 with air atmosphere, these samples were slowly cooled down up to 20 °C at a temperature ramp of 0.5°C/min. Then, macro-photography was used to register the surface of samples in order to evaluate the macro and micro damage. Six (6) samples were analyzed per composition, but only one is presented in the optical images. For the crack analysis, ImageJ software was used to quantify the crack lengths and their distribution. In addition, a Monte Carlo simulation was used to analyze the damage, where the modeling variable was the crack length for each sample composition after exposure to high temperature. These results were fitted to a Weibull distribution [152,153], using the Risk software. The variability range of the crack length was

defined as being not over a 10% of the initial crack length. A total of 1000 simulations were conducted with the same software for each manufactured composition

5.3 RESULTS

The FTIR and XRD tests showed that the main hydrated phases at 20 °C are CAH_{10} (Monocalcium aluminate decahydrate), C_3AH_6 (Katoite), C_2AH_8 (Dicalcium aluminate octahydrate) and AH_3 (Gibbsite). These results, those from of the characterization of the raw materials used and those from the hydrated phases have seen presented before [31].

5.3.1 HIGH TEMPERATURE BEHAVIOR

Figure 11a, b, c, and d shows photographs of CACP 51wt% and CACP 71wt% samples made and W/C of 0.25, 0.3 and 0.4. These samples were subjected to 20, 500, 800 and 1000 °C. Cracks appeared for all W/Cs, and the higher temperature produced a higher damage. In general, it can also be observed that at 500 °C is hard to see the damage differences based on the alumina contents. However, at 800 °C, samples with lower alumina contents (CACP 51wt%) present more cracks than samples with higher alumina contents (CACP 71wt%), although the latter samples show a single larger crack, probably due to a concentrated damage.

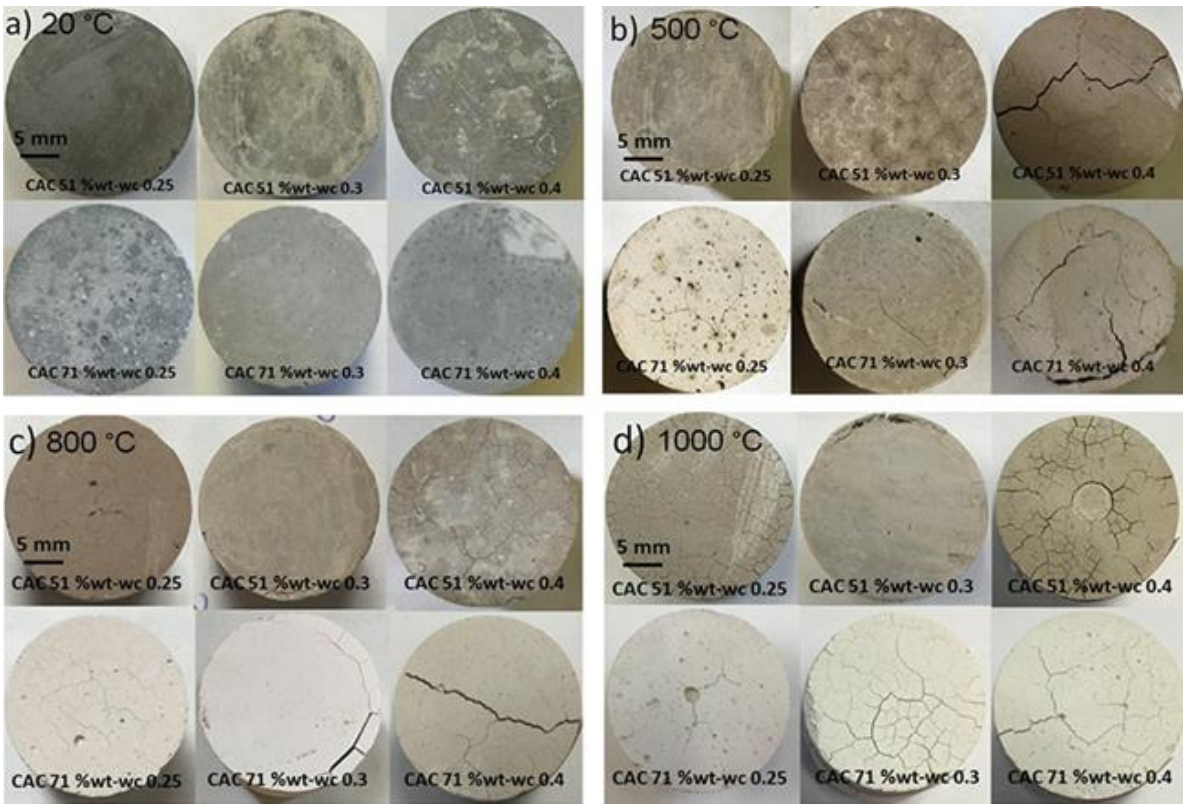

Figure 11. Images of CACP exposed to:
a) 20°C, b) 500 °C, c) 800 °C, and d) 1000°C. The scale bar is the same (5mm) for all pictures.

This general trend was also observed at 1000°C, which suggests that even though alumina content decreases the amount of cracks, less alumina gives a better thermal stress distribution, as shown by the fact that no single cracks (catastrophic cracks) pass through the whole sample. Another observation is that for the same temperature but at higher W/Cs, more damage is present. This can be explained by the higher porosity in the samples generated for higher W/Cs. In addition, there is a loss in strength associated with the phase conversion process driven by exposure to high temperatures [51].

Figure 12 shows XRD data for CACP subjected to 1000 °C: Figure 12a, shows the diffractogram for samples of CACP 51wt% Al_2O_3 with W/C = 0.25. As can be seen, the main phase is the Gehlenite, with its peak of greatest intensity located at an angle of 36.67º, and an abundance shown by Rietveld's analysis of 48.4%. The phase the abundance results in all the formulations investigated in this study and subjected to a heat of 1000 °C, given by Rietveld analysis, are shown more specifically in Figure 13, for the notation of the formulations see Table 17.

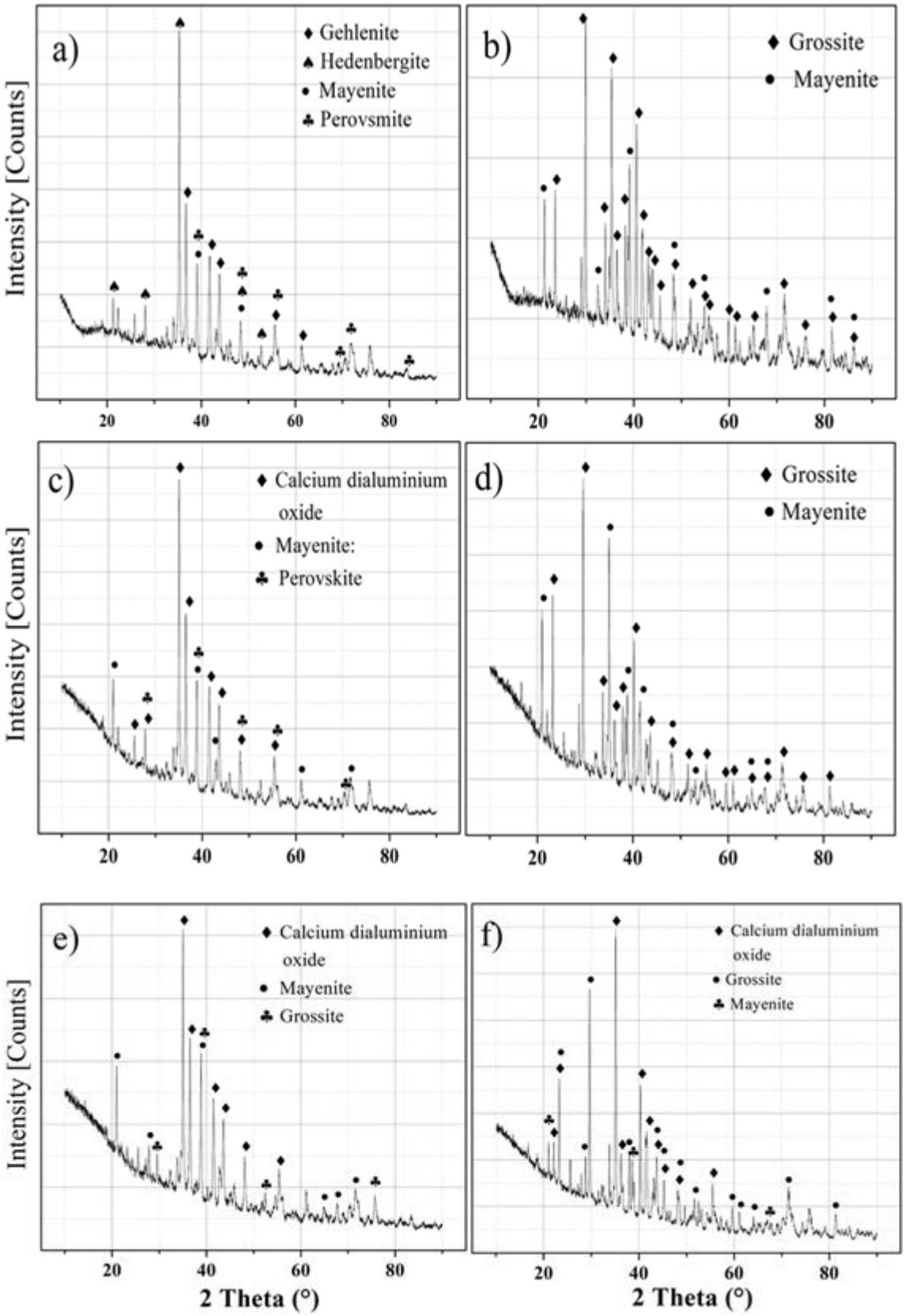

Figure 12. XRD for CACP subjected to 1000°C. CACP 51wt%:

W/C: a) 0.25, c) 0.3, e) 0.4: CAC 71wt%: W/C: b) 0.25, d) 0.3 and f) 0.4.

A main phase of hedenbergite, with its peak of greatest intensity located at an angle of 35.34º and an abundance of 37.7%, can also be observed. Two minor phases are present in this diffractogram: one of mayenite, identified with its peak of greatest intensity at an angle of 21.13º and an abundance of 12.7%, and the other of perovskite, identified with its peak of greatest intensity at an angle of 39.17º and an abundance of 1.2%.

In Figure 12b, for CACP 71wt% Al_2O_3- W/C = 0.25, only two phases were identified. The Grossite as the most abundant with a value 79.7% given by the Rietveld analysis (see Figure 13) and the highest intensity peak located at an angle of 29,71º. Mayenite was also identified with an abundance of 20.3% and a peak of greatest intensity located at an angle of 21.09º.

In Figure 12c, for CACP 51wt% Al_2O_3-W/C=0.3, the main phase calcium dialuminium oxide (CA_2), showing its peak of greatest intensity at an angle 35.068º and an abundance of 80.2%. There is a second intermediate phase (Mayenite) with its peak of greatest intensity at an angle de 20.962º, and an abundance of 16.3% and a minority phase (Perovskite) with its peak of greatest intensity at an angle of 38.943º and an abundance of 3.5%.

In Figure 12d, for CACP 71wt% Al_2O_3-W/C=0.3, the main phase (Grossite) showing its peak of greatest intensity at an angle of 29.607º and an abundance of 71.5% and there is a secondary phase (Mayenite) with a main peak at an angle of 20.986º and an abundance of 28.5%.

In Figure 12e, for CACP 51wt% Al_2O_3 -W/C=0.4, the main phase is calcium dialuminium oxide (CA_2), showing its peak of greatest intensity at a angle of 35.068º and an abundance of 68.6%. There is a second intermediate phase (a polymorphism of mayenite) with a main peak at a angle of 20.986º and an abundance of 25.8%, and a minority phase (Grossite) with a main peak at a angle of 29.607º and an abundance of 5.6%.

In Figure 12f, for CACP 71wt% Al_2O_3-W/C=0.4, the main phase calcium dialuminium oxide (CA_2), showing its peak of greatest intensity at an angle of 35.068° and an abundance of 50.6%. There is a second intermediate has (Grossite) with a main peak at an angle of 29.607° and an abundance of 45.8% and a minority phase (Mayenite) with a main peak at an angle of 21.061° and an abundance of 3.6%.

The phases identified from these diffractograms are shown in Table 18. CACP 51wt% and CACP 71wt%- Al_2O_3 and W/C= 0.4 were exposed to 20 °C and then analyzed by SEM, see Figure 14. It can be observed in Figure 14 the regular hexagonal and cubic geometries of the hydrated phases, which mainly correspond to CAH_{10} (Monocalcium aluminate decahydrate), C_3AH_6 (Katoite), and some AH_3 (Gibbsite) [31].

CACP 51wt% and CACP 71wt% -Al_2O_3 and W/C= 0.25, 0.3 and 0.4, also were exposed to 1000 °C for an hour, and then analyzed by SEM, as prepresented in Figure 15. In these samples, approximately the same phases appeared, and most of them were anhydrides (also see Table 18).

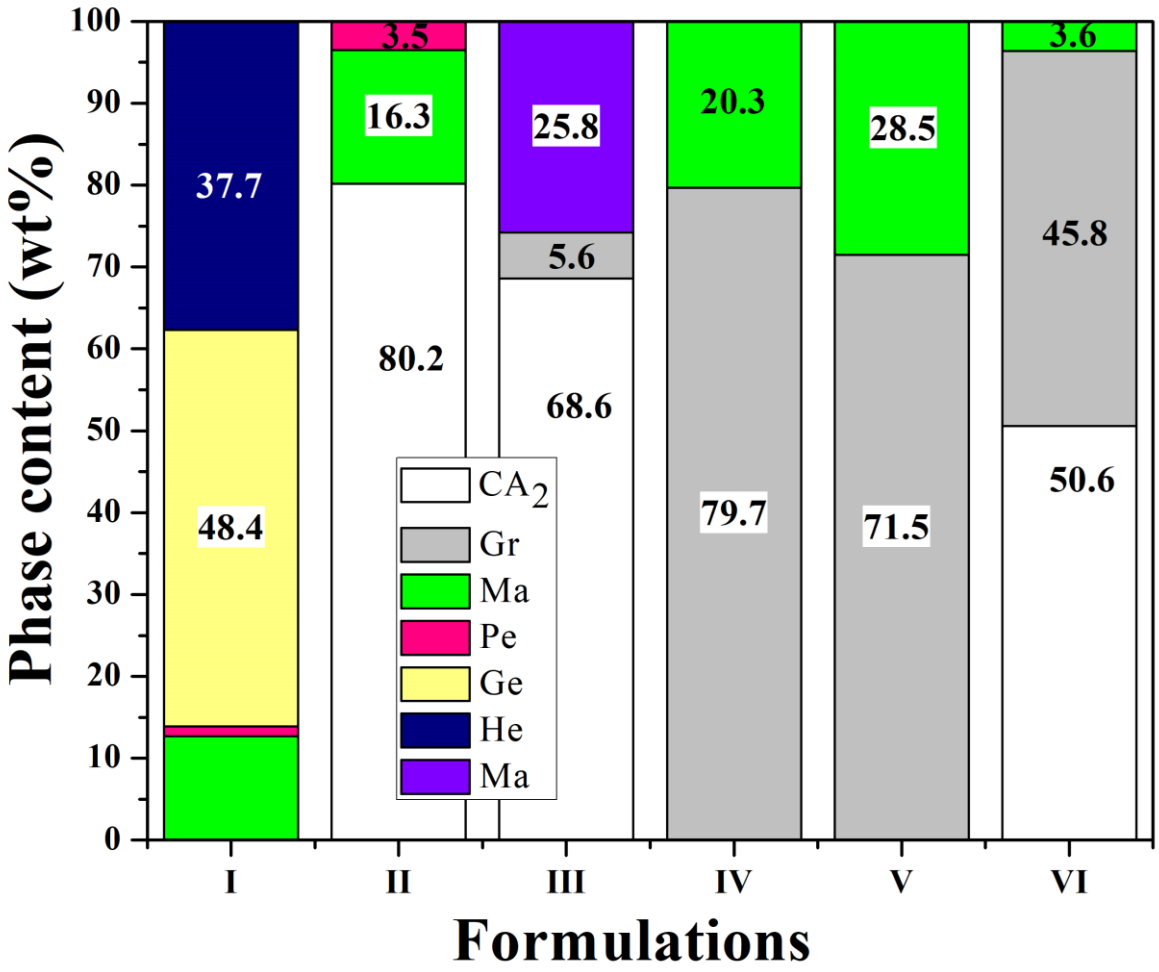

Figure 13. XRD Analysis using Rietveld refinement for CACP subjected to 1000°C. The acronyms are: Ma (Mayenite), He (Hedenbergite), Ge (Gehlenite), Pe (Perovskite), Gr (Grossite).

Table 17. Notation for formulations of the Figure 13

	CACP 51wt% - Al_2O_3			CACP 71wt% - Al_2O_3		
	I	II	III	IV	V	VI
W/C	0.25	0.3	0.4	0.25	0.3	0.4

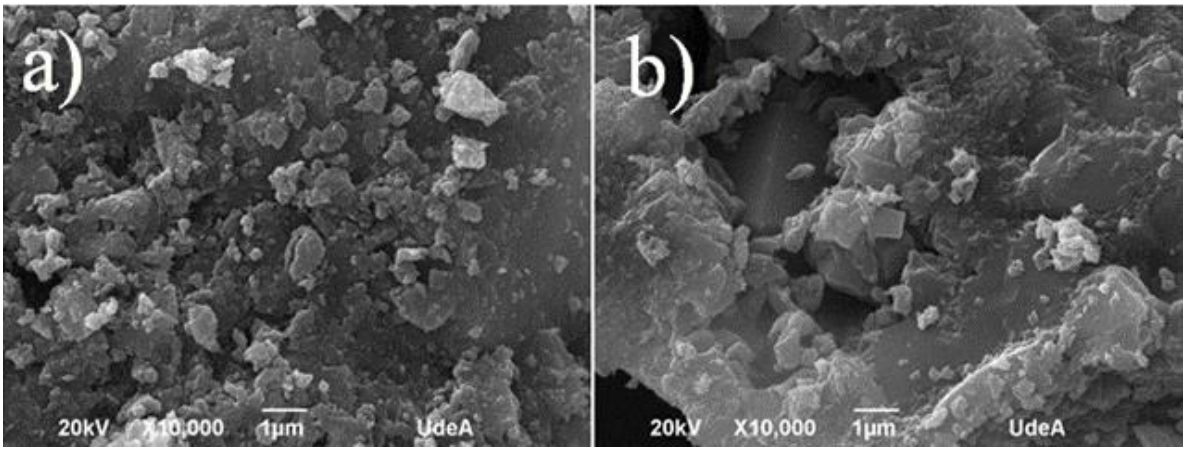

Figure 14. SEM images for CACP exposed at high temperature (20 °C), W/C=0.4:
a) CACP 51wt%, b) CACP 71wt%.

Table 18. XRD Analysis for CAC paste subjected to 1000 °C

Sample			Phases Composition						
	wt% Al_2O_3	W/C	CA_2	Grossite	Mayenite	Perovskite	Gehlenite	Hedenbergite	Mayenite
I	51	0.25	-	-	$Ca_6Al_7O_{18}$	-	$Ca_4Al_4Si_2O_{14}$	$CaFeSi_2O_6$	-
II	51	0.3	$CaAl_2O_4$	-	$Ca_{12}Al_{14}O_{33}$	$CaTiO_3$	-	-	-
III	51	0.4	$CaAl_2O_4$	$CaAl_4O_7$	-	-	-	-	$Ca_{12}Al_{14}O_{33}$
IV	71	0.25	-	$CaAl_4O_7$	$Ca_6Al_7O_{18}$	-	-	-	-
V	71	0.3	-	$CaAl_4O_7$	$Ca_{12}Al_{14}O_{33}$	-	-	-	-
VI	71	0.4	$CaAl_2O_4$	$CaAl_4O_7$	$Ca_{12}Al_{14}O_{33}$	-	-	-	-

When comparing the microscopy images, there is a morphology relationship within the water-to-cement ratio (W/C) that was also reported in the previous research [154].

More geometric regularity is observed in Figure 15a and 15b, which have the lowest W/C. In addition, cement with 51 wt% alumina contents (Figure 15a, 15b and 15c), shows more geometric regularity respect to cement with 71 wt% alumina contents. These results suggest that temperature gradients are related with a higher diffusion rate at higher alumina contents and higher W/Cs. More energy is absorbed, and thus the geometrical shape is affected.

Figure 16. FTIR curves for CAC pastes exposed at 1000°C: CACP-51wt%:

W/C: a) 0.25, c) 0.3, e) 0.4. CACP 71wt%: W/C: b) 0.25, d) 0.3, f) 0.4. shows the results of FTIR tests for CACP exposed at 1000 °C. The FTIR tests revealed two well-defined phases, mayenite and calcium aluminate, found in both types of cements.

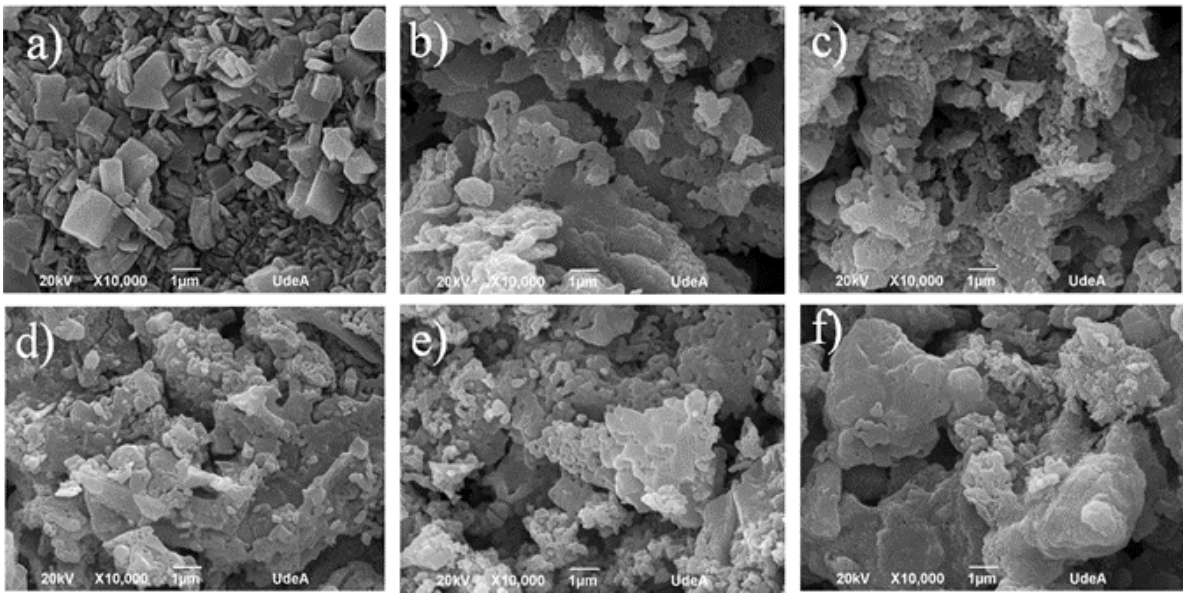

Figure 15. SEM images for CACP exposed at high temperature (1000 °C):
CACP 51wt%: W/C: a) 0.25, b) 0.3, c) 0.4. CACP71 wt%: W/C: d) 0.25, e) 0.3, f) 0.4.

Table 19. Characteristic absorbance bands of CAC phases at 1000°C summarizes the characteristic absorbance bands of the calcium aluminate cement powder phases reported in the literature and found in this work.

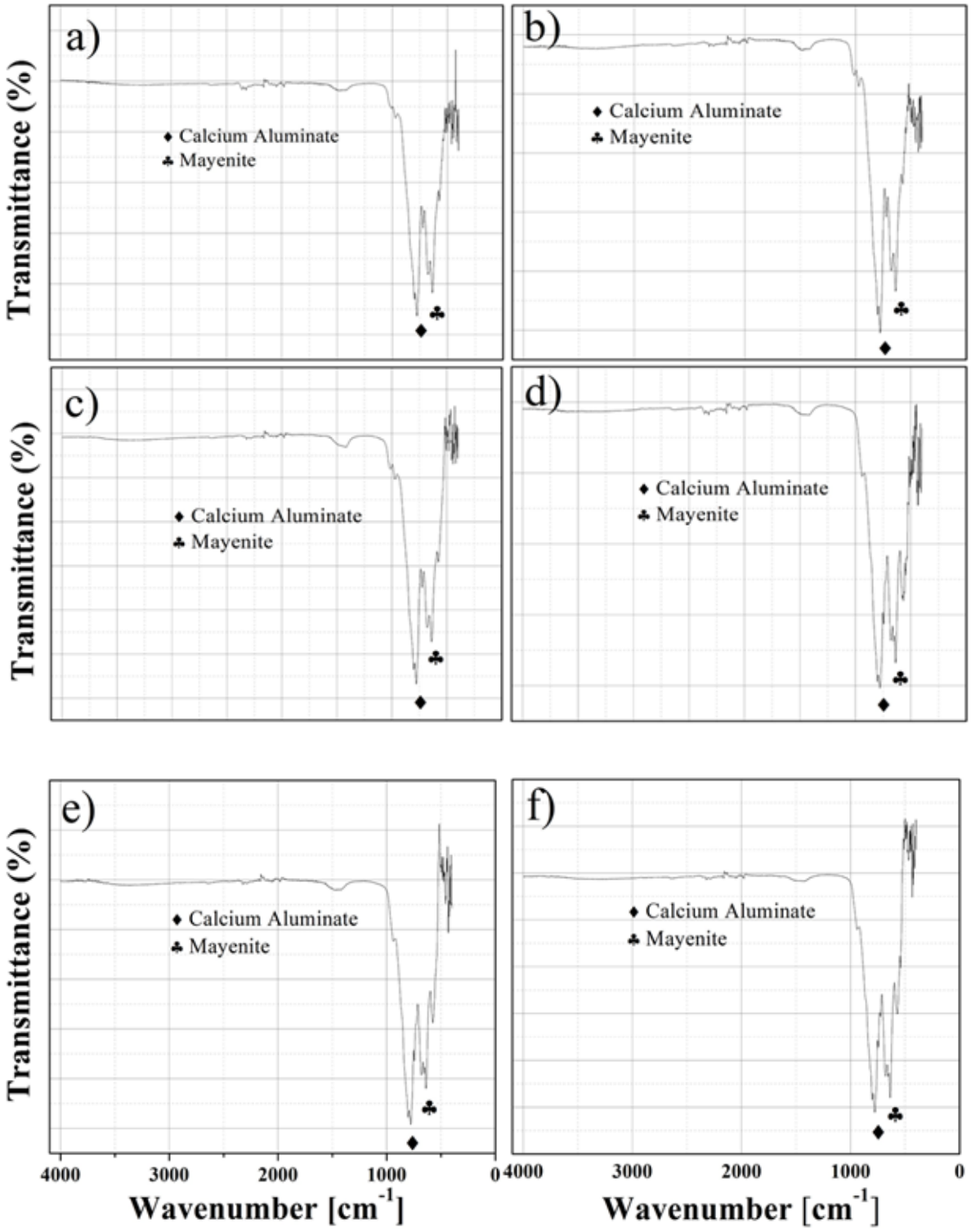

Figure 16. FTIR curves for CAC pastes exposed at 1000°C: CACP-51wt%: W/C: a) 0.25, c) 0.3, e) 0.4. CACP 71wt%: W/C: b) 0.25, d) 0.3, f) 0.4.

Table 19. Characteristic absorbance bands of CAC phases at 1000°C

Phase	Fundamental vibration (cm^{-1})	Reference
CA	840, 805, 780, 730, 720, 680, 640, 570, 540, 450, 420	[31,155]
	640.90 (51A-wt%: W/C=0.25), 641.2 (51A-wt%: W/C=0.3), 641 (51A-wt%: W/C=0.4), 640.90 (71A-wt%: W/C=0.25), 640.1 (71A-wt%: W/C=0.3), 641.27 (71A-wt%: W/C=0.4)	This work
Mayenite	850, 780, 610, 575, 460, 410	[31,155]
	780.65 (51A-wt%: W/C=0.25), 776.94 (51A-wt%: W/C=0.3), 780.64 (51A-wt%: W/C=0.4), 780.64 (71A-wt%: W/C=0.25), 780.64 (71A-wt%: W/C=0.3), 780.64 (71A-wt%: W/C=0.4)	This work

5.4 DAMAGE ANALYSIS

NORMAL DISTRIBUTION

Figure 17 shows crack size probability curves (normal distribution) for samples of calcium aluminate cements CACP 51wt% and 71wt% - Al_2O_3, subjected to temperatures of 500, 800°C and 1000°C.

The quantification of the damage was conducted by digital image analysis of fractured samples according to the alumina content, temperature, and W/C. The crack lengths were measured using ImageJ software, and data were grouped in just one number, the total crack length.

One observation from results shown in Figure 17a, is that CACP 51wt% exposed at 500°C presented bigger average crack size for a larger W/Cs. At W/C=0.4, the average crack size is 10.8 mm, while at W/C=0.3 and 0.25, the average crack size are 2.2 and 4.6 respectively. For CACP 71wt% at 500°C, shown in Figure 17b, it was found that in general as the W/C increases, the average crack size decreases. For CACP 51wt% at 800°C, shown in Figure 17c, there is less difference among the mean crack size, all near to 3mm. This is caused for the high temperture that can heal the cracks initially generated by the thermal effect. This is supported by Figure 17d, where for CACP 71wt% at 800°C, average crack size is even closer. Figure 17e and 17d presents CACP 51wt% and CACP 71wt% exposed to 1000°C, and in general show that more water in the paste (or more W/C) produce larger cracks, which is generates greater structural damages.

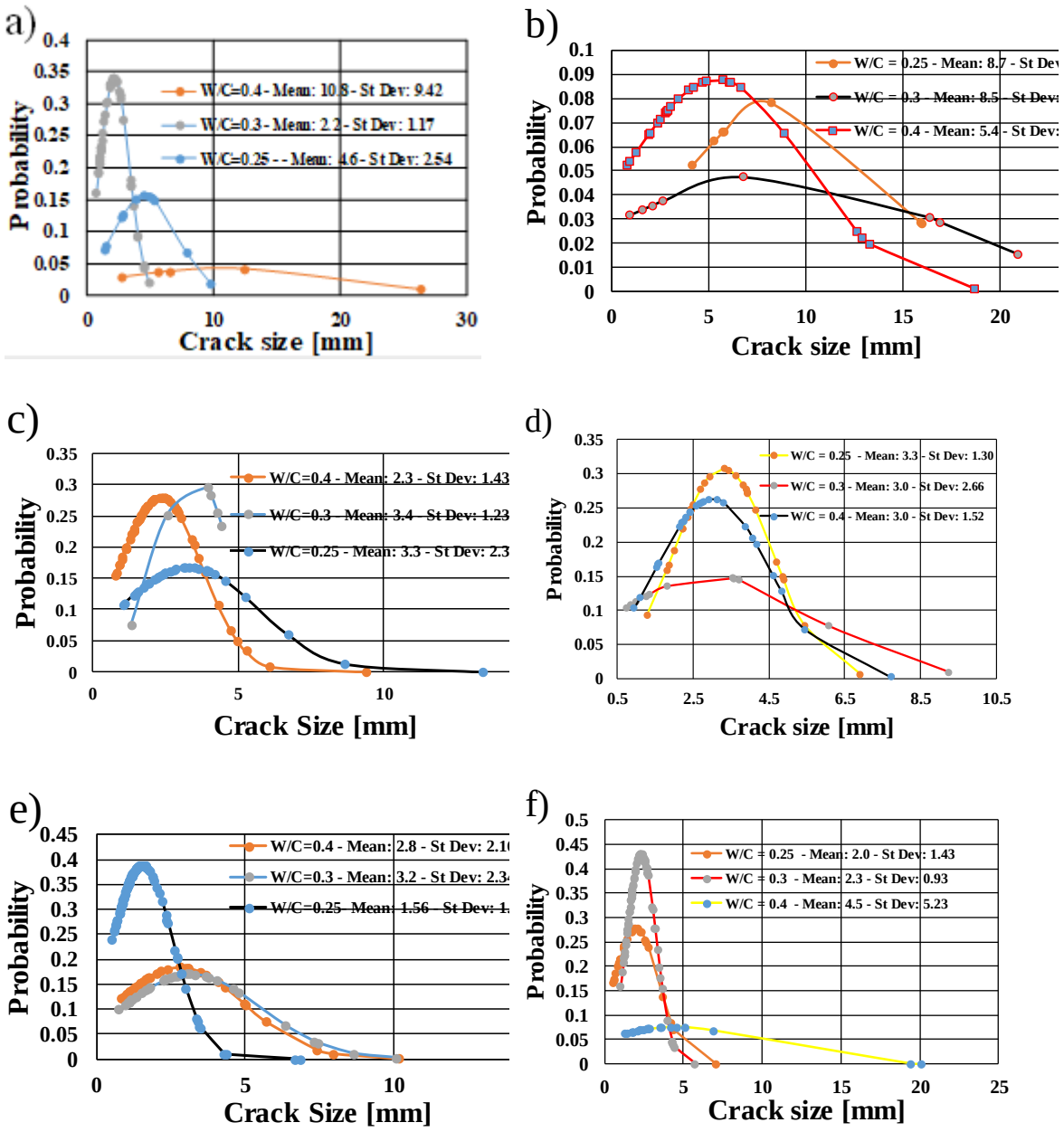

Figure 17. Crack's size probability curves:
CACP subjected to temperatures of 500, 800 and 1000 °C with W/C=0.25, 0.3 and 0.4 for different types of CACP: CACP 51wt%: a) 500 °C, c) 800 °C, e) 1000 °C. CACP 71wt%: b) 500°C, d) 800°C and f) 1000°C.

Figure 18 summarizes all the previous results for the mean crack length, where the samples CACP 51wt%-W/C=0.4, CACP 71wt%-W/C=0.25, and CACP 71wt%-W/C=0.3, follow the same trend; (for the notation of the formulations see Table 17): as temperature increases, the mean crack length decreases as well.

This may be due to the occurrence of significant damage at lower temperatures, as a result of the water released and its subsequent structural shrinkage. Later, the crack length reduces

due to a sintering effect (crack healing) because of the high temperature. For all other formulations, it seems that the mean crack length is not very dependent on temperature.

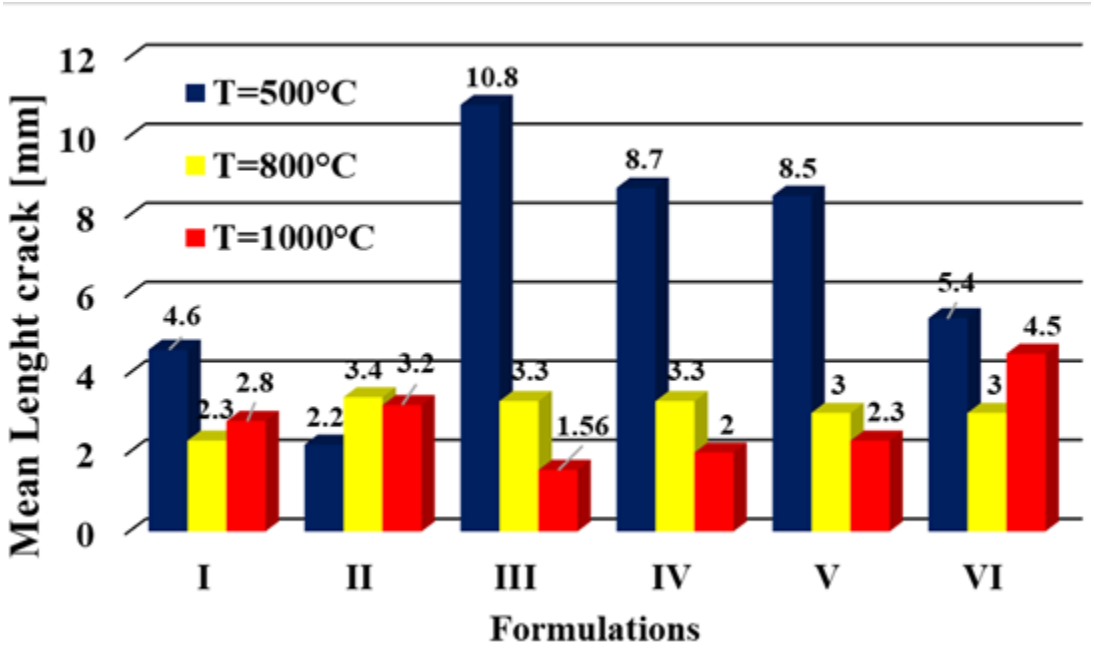

Figure 18. Mean crack length by the alumina content in two cement formulations: CACP 51wt% and 71wt%, subjected to 500, 800 and 1000°C.

Damage Analysis for Alumina Content Factor

Figure 19 shows total crack length curves for the samples with a) CACP 51wt% and b) CACP 71wt% subjected to high temperatures of 500, 800 and 1000 °C, and for W/C = 0.25, 0.3 and 0.4. It can be observed that the higher the temperature, the greater the damage in both cements. However, the cement with the highest alumina content suffered worse damage from a fixed temperature. A connection between the degree of damage and the W/C in these two figures is not clear. This suggests that the higher the alumina content, the better the behavior of the cement at high temperature, particularly at 1000 °C, which is quite high for a cementitious material.

Damage Analysis for the Temperature Factor

Figure 19 also shows that at 500 °C, the samples with the greatest damage are CACP 71wt% for a W/C ratio of 0.4 and CACP 51 wt% for a W/C ratio of 0.3. The direct relationship between the degree of damage, the alumina content and the W/C at this temperature is not clear. In addition, at 800 °C, the

samples with the greatest damage are CACP 51 wt% for a W/C ratio of 0.4 and CACP 51wt% for a W/C ratio of 0.3. This suggests that at 800 °C, the CACP 51wt% performs better than the CACP 71 wt% cement. Therefore, the direct relationship between the degree of damage

and W/C at this temperature is also not clear. On the other hand, at 1000 °C, cements with a lower alumina content and lower W/C showed more damage.

Damage Analysis for Water to Cement Ratio (W/C) Factor

The other results from

Figure 19 show that for W/C = 0.25 at 1000 °C and at 800 °C, the lower alumina content cement shows more damage. For W/C = 0.3 at 1000 °C, the higher alumina content cement shows more damage, and for 800 °C, the least damage occurs. It can also be observed that for W/C = 0.4 at 800 °C, the cement of lower alumina content shows more damage, while for 800 °C, the least damage occurs.

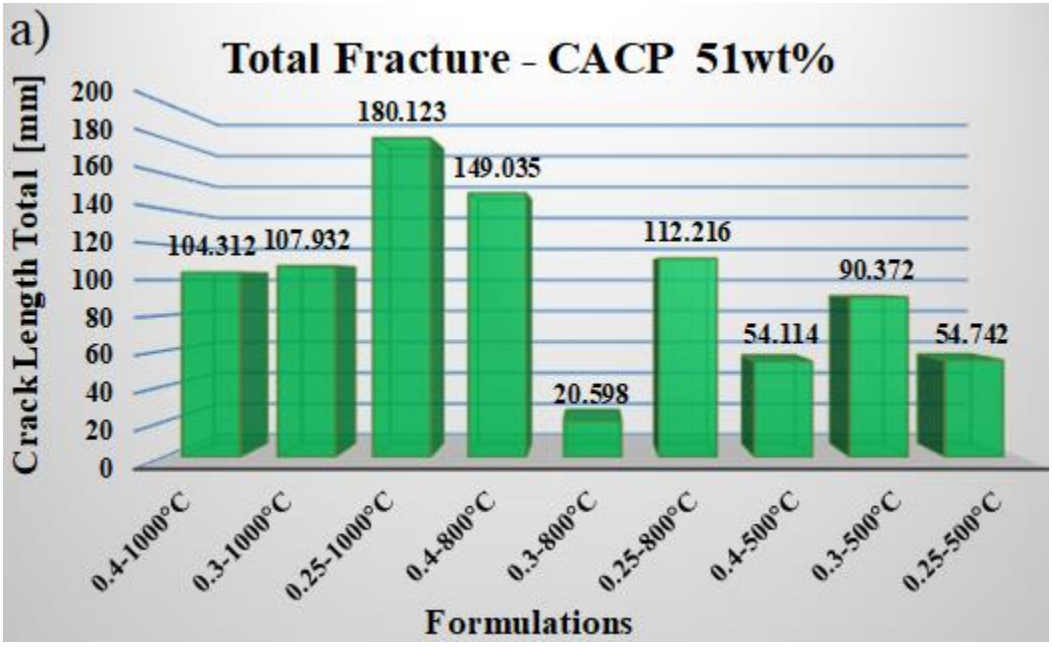

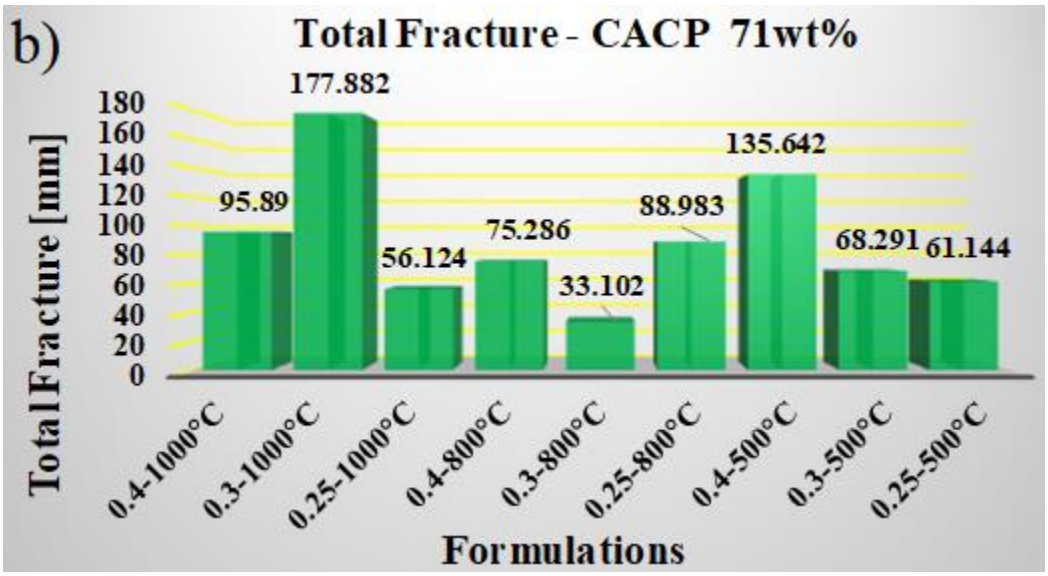

Figure 19. Damage quantification analyzed:
W/C =0.25, 0.3 and 0.4, and exposed to temperatures of 500, 800 and 1000 °C: a) CACP 51wt%, b) CACP 71wt%.

Damage Analysis for Monte Carlo Simulation and Analysis Weibull

Figure 20 shows Monte Carlo simulation curves for CAC paste subjected to 500, 800 and 1000 °C, for W/C = 0.4. Figure 20 shows that for a higher alumina content, the average crack size is higher, meaning that at 1000 °C, these cements suffered greater damage due to a higher alumina content. To reduce the length of this article, only the Monte Carlo analysis for the W/C = 0.4 formulation, which is the most optimum ratio to avoid conversion, has been included in detail. Three (3) samples were analyzed per composition, complemented by the Monte Carlo method which takes the crack formation as a stochastic process (no deterministic law), thereby simulating a large number (1000) of trials. In addition, the simulation is a reference to compare with the experimental results.

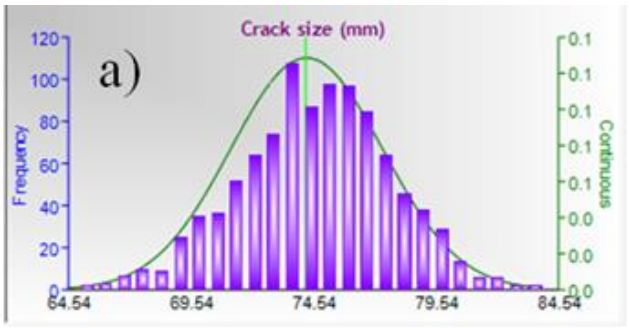

Statistics	Result
Number of Trials	1000
Mean	74.2204
Median	74.3195
Standard Deviation	3.1059
Variance	9.6464
Coefficient of Variation	0.0418
Maximum	83.5886
Minimum	64.5374
Range	19.0512
Skewness	-0.1447
Kurtosis	-0.0525
25% Percentile	72.2133
75% Percentile	76.3255
Percentage Error Precision at 95% Confidence	0.2594%

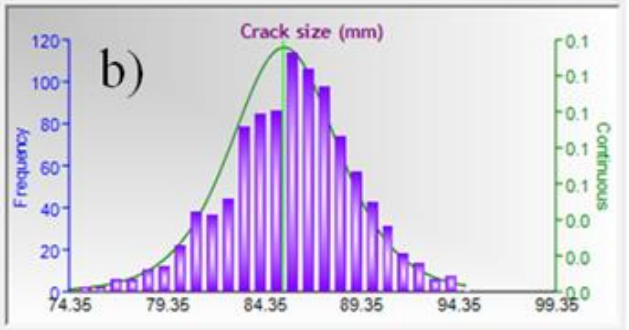

Statistics	Result
Number of Trials	1000
Mean	85.0370
Median	85.0024
Standard Deviation	3.2339
Variance	10.4580
Coefficient of Variation	0.0380
Maximum	94.8220
Minimum	75.5238
Range	19.2982
Skewness	-0.0079
Kurtosis	0.0146
25% Percentile	82.9343
75% Percentile	87.2411
Percentage Error Precision at 95% Confidence	0.2357%

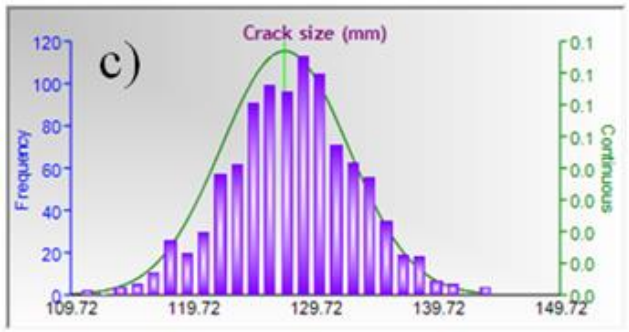

Statistics	Result
Number of Trials	1000
Mean	127.1890
Median	127.3438
Standard Deviation	5.2678
Variance	27.7500
Coefficient of Variation	0.0414
Maximum	143.6604
Minimum	109.7223
Range	33.9381
Skewness	-0.0591
Kurtosis	0.1351
25% Percentile	123.8875
75% Percentile	130.5819
Percentage Error Precision at 95% Confidence	0.2567%

Figure 20. Monte Carlo Simulation curves CACP 71wt%, W/C: 0.4 and exposed to temperatures: a) 500 °C, b) 800 °C, c) 1000 °C.

From Figure 18 a phenomenological model can be found using nonlinear regression techniques. This model is given by the following expression:

$$\delta_j^i = 8\omega k_R 10^{-5} T^2 - 0.1364\omega k_R T + 66.28\omega k_R$$

where

T : Temperature °C
δ : Amount of damage (mm)
i : Index that indicates the type of cement paste, takes values of 1 and 2. When $i = 1$, it refers to CACP51 and $i = 2$, it refers to CACP71.
j : Index that labels each formulation, takes values of 1,2 and 3.
ω: Water/Cement ratio. It takes values of 0.25, 0.3 and 0.4.
k_R: It is an adjustment factor. It takes values depending on the values of the pair of indices i, j, as follows:

i	j	R
1	*1*	*1,2 and 3*
1	*2*	*4, 5 and 6*
1	*3*	*7, 8 and 9*
2	*1*	*10, 11 and 12*
2	*2*	*13, 14 and 15*
2	*3*	*16, 17 and 18*

where

$k_1 = k_2 = k_3 = k_{10} = 1;\ k_4 = 0.42; k_5 = 0.46;, k_6 = 0.62;\ k_7 = 0.94; k_8 = 1.23; k_9 = 1.37; k_{11} = 1.4;\ k_{12} = 1.62; k_{13} = 1.25; k_{14} = 1.39; k_{15} = 1.33; k_{16} = k_7 = 0.94;\ k_{17} = 0.89.$

In this way, considering all possible combinations of index values, 6 models are generated:

1. **CACP51-0.25W/C; $\boldsymbol{i = j = 1;\ \omega = 0.25.\ k_R \equiv k_1 = k_2 = k_3}$**

$$\delta_1^1 = 8\omega k_1 10^{-5} T^2 - 0.1364\omega k_2 T + 66.28\omega k_3$$

$$\boxed{\delta_1^1 = 2 * 10^{-5} T^2 - 0.0341T + 16.6}$$

2. **CACP51-0.3** ; $\boldsymbol{i = 1, j = 2; \omega = 0.3. k_R \equiv k_4;\ k_5;\ k_6}$

$$\delta_2^1 = 8\omega k_4 10^{-5} T^2 - 0.1364\omega k_5 T + 66.28\omega k_6$$

$$\delta_2^1 = 1 * 10^{-5} T^2 - 0.029T + 12.2$$

3. **CACP51-0.4** ; $\boldsymbol{i = 1, j = 3; \omega = 0.4. k_R \equiv k_7;\ k_8;\ k_9}$

$$\delta_3^1 = 8\omega k_7 10^{-5} T^2 - 0.1364\omega k_8 T + 66.28\omega k_9$$

$$\delta_3^1 = 3 * 10^{-5} T^2 - 0.0076T + 36.3$$

4. **CACP71-0.25** ; $\boldsymbol{i = 2, j = 1; \omega = 0.25. k_R \equiv k_{10}; k_{11}; k_{12}}$

$$\delta_1^2 = 8\omega k_{10} 10^{-5} T^2 - 0.1364\omega k_{11} T + 66.28\omega k_{12}$$

$$\delta_1^2 = 2 * 10^{-5} T^2 - 0.0479T + 26.9$$

5. **CACP71-0.3** ; $\boldsymbol{i = 2, j = 2; \omega = 0.3. k_R \equiv k_{13};\ k_{14};\ k_{15}}$

$$\delta_2^2 = 8\omega k_{13} 10^{-5} T^2 - 0.1364\omega k_{14} T + 66.28\omega k_{15}$$

$$\delta_2^2 = 3 * 10^{-5} T^2 - 0.0569T + 26.5$$

6. **CACP71-0.4** ; $\boldsymbol{i = 2, j = 3; \omega = 0.4. k_R \equiv k_{16};\ k_{17};\ k_{18}}$

$$\delta_3^2 = 8\omega k_{15} 10^{-5} T^2 - 0.1364\omega k_{16} T + 66.28\omega k_{17}$$

$$\delta_3^2 = 3 * 10^{-5} T^2 - 0.0483T + 21.8$$

The experimental curves, their respective fit curve and the algebraic equation that represents it are shown in the Figure 21.

Figure 21 is another form of graphic representation of Figure 18, it does not introduce new information, so there is no need for a new analysis of it.

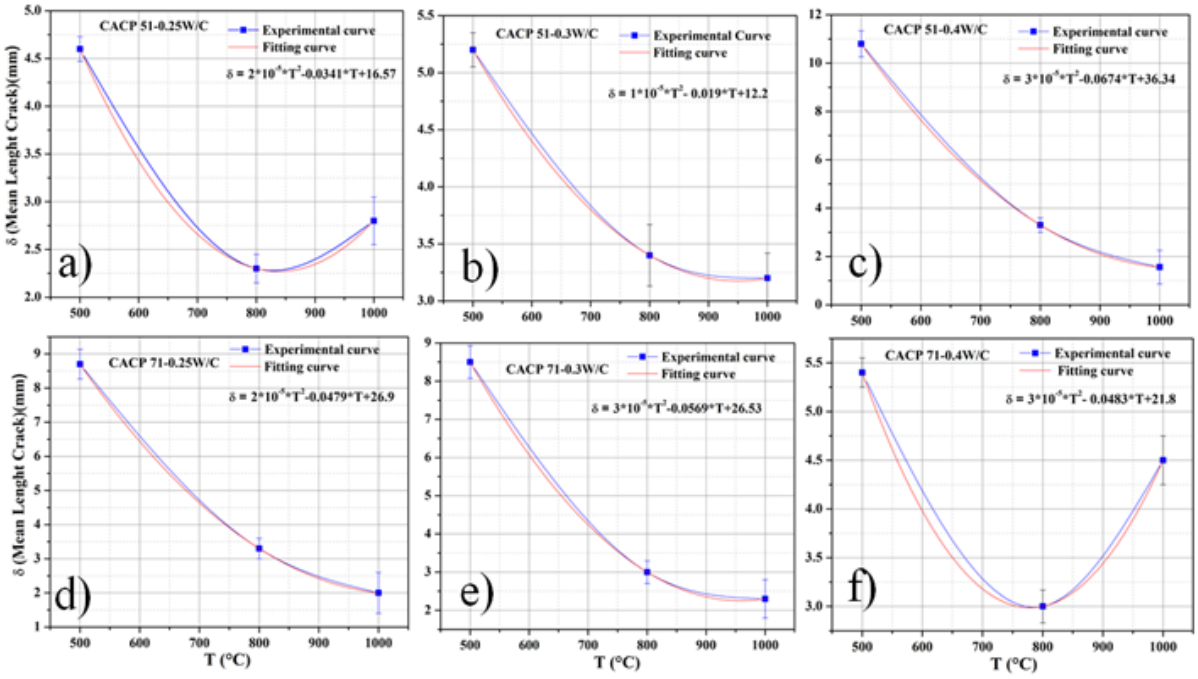

Figure 21. Experimental and fitting curves of damage behavior with temperature

5.5 DISCUSSION

From the XRD and SEM results, it can be observed that the combined phases are quite similar in the two cement pastes investigated, i.e., CAC with 51 and 71 wt% alumina content. However, the cement with 71 wt% alumina formed CA_2 [31] and showed more significant morphological changes, with CAH_{10} as the main hydration phase at 20 °C. Part of the water contained in the hydrated hexagonal calcium aluminates, CAH10, is weakly bounded [154]. CAH_X, C_2AH_z and C_4AH_Y can typically take values of X=10, Y=8, and Z=13. These molecules can lose small amounts of water without significantly changing their structure and are involved in the transformation from hexagonal to cubic forms. This is the fundamental reason why calcium aluminate cement paste is fractured when exposed to temperatures over 37 °C. Therefore, the main reason why the pure aluminate cement paste exhibits cracking with temperature is because of the weak bonding and variability of all these products (CAH_X, C_2AHz and C_4AH_Y). This research has made several new contributions to the literature, especially in terms of CACs exposed to high temperature. Most of the available research [128] has been carried out with CAC concrete, for just one specific CAC formulation (CAC with 50 wt% of alumina) plus aggregates. In this research, more formulations were used, and a complete damage analysis was conducted.

Figure 11 shows that in general, the higher alumina content samples (71 wt%) presented larger cracks when compared with the samples with lower alumina contents (51 wt%). However, more cracks and therefore longer length cracks (sum of all lengths together) appeared in the lower alumina cement. This shows that the larger defects did not always account for greater average damage. This is associated with a complex heat transfer

interrelationship among the alumina and other phases which can be optimized with additives, meaning that there is still room to improve the CAC.

Visual analysis of these cracks had to be completed with detailed quantification of the statistical analysis from Figure 17. First of all, for CAC 71 wt% at 500 °C, shown in Figure 17b, the damage given by the crack size was probably the lowest found in this research (up to 0.09), corresponding to 4 times less than for other samples. This means that the aforementioned combination of chemical composition and working conditions (500 °C) was ideal, and thus, it can be used in smart designs that reduce the exposure temperature to such conditions. All other compositions and conditions showed a crack size

probability up to 0.35, depending on the W/C ratio. In terms of the mean crack length, crack size probability, W/C ratio, exposure temperature and composition, it is hard to stablish a general conclusion that goes beyond the specific trends shown in Fig. 8, which is associated with the complex combination of multiple micro-constituents. It was confirmed that as temperature increases, the mean crack length decreases, which is associated with significant damage first caused by water released at temperatures below 400 °C (for bonded and unbounded water) and by structural shrinkage due to the release of waste. At high temperatures, the crack length reduction was associated with a sintering or healing process

For some formulations, the mean crack length was not very dependent on temperature. It is well-known that for both cements and all other fragile materials, these results can be substantially improved by the incorporation of the appropriate fibers as reinforcement, in this case to reinforce the cementitious matrix. Substantial research has been conducted before for cement-based materials, giving good outcomes for diverse types of cementitious binders used in high-temperature applications. Silicon carbide and basalt fibers could be a good option for CAC composites [156] This investigation has used a very simple but powerful two dimensional digital image analysis method to quantify damage by measuring the crack length, and has taken this length as the main damage parameter. The data values were adjusted to a Weibull distribution simulated using the Monte Carlo method. The method gives the relationship between the damage parameter (crack length), processing temperature, the water- to-cement ratio (W/C) and the alumina content in the CAC cements. It was found that CAC samples show significant thermal damage with a corresponding deterioration in compressive strength. The results imply that CACs in the present formulation do not support thermal shock. Some modification [157] that include the addition of ceramic reinforcement in fibers look very promising for structural applications.

5.6 CONCLUSIONS

There are several conclusions that can be drawn from this study. A simple and inexpensive method is validated that evaluates not only CAC cements but also any other type of cementitious or ceramic-based materials exposed to significant temperature changes and resulting in cracking damage. In addition, some more specific conclusions are:

- Materials with higher alumina content have an increased number of cracks. Furthermore, higher W/Cs contributes to the conversion process and generate greater numbers of cracks in these samples.

- At higher temperature and lower W/Cs, there is a greater probability of larger cracks.
- At higher alumina contents, the average crack size is higher, which causes these cements to have greater structural problems at 1000 °C.
- Calcium aluminate cement pastes exhibit limited refractoriness properties (but are still to be improved if not subtantialy enhanced with high temperature ceramic fibers or additives.

6. CHAPTER 6. EFFECT OF HIGH TEMPERATURE AND ADDITIONS OF SILICA ON THE MICROSTRUCTURE AND PROPERTIES OF CALCIUM ALUMINATE CEMENT PASTES

John F. Zapata, Henry A. Colorado & Maryory A. Gomez (2020) Effect of high temperature and additions of silica on the microstructure and properties of calcium aluminate cement pastes, Journal of Sustainable Cement-Based Materials, DOI: 10.1080/21650373.2020.1737593

6.1 INTRODUCTION

The hydration of CAC is highly dependent on temperature, resulting different morphologies, the products of which continuously alter the properties of the material [30,31,105,158–160]. The strength of CACP is mainly due to the hydration of CA, the products of which in general terms follow the scheme (10) [3,19,33,161,162].

$$\left.\begin{array}{c} CA + 10H \rightarrow CAH_{10} : T \leq 20°C \\ 2CA + 11H \rightarrow C_2AH_8 + AH_3 : T \sim 30°C \\ 3CA + 12H \rightarrow C_3AH_6 + 2AH_3 : T > 55°C \end{array}\right\} \quad (10)$$

C_2AH_8 can occur as a consequence of the hydration of CA_2 that is hydrated according to the reaction scheme (11):

$$\left.\begin{array}{c} CA_2 + 13H \rightarrow CAH_{10} + AH_x : T \leq 20°C \\ 2CA_2 + 13H \rightarrow C_2AH_8 + 3AH_x : T \sim 30°C \\ 3CA_2 + 21H \rightarrow C_3AH_6 + 5AH_3 : T > 55°C \end{array}\right\} \quad (11)$$

It is formed at an approximate temperature of hydration of ~ 30 °C, which requires that the ratio CaO/Al_2O_3 exceeds unity, C_2AH_8 is also formed by conversion of CAH_{10} [163]. C_2AH_8 and gel-AH_3 are formed naturally at about T=30 °C, and C_3AH_6 and AH_3 (crystalline) at temperatures greater than 55 °C [3,19]. The hydration of CA_2 contributes to late strength of hydrous CAC [35].

The conversion process of CAC, is due to the fact that the phases CAH_{10} and C_2AH_8 are metastable at ambient temperature and convert to the more stable phases C_3AH_6 and AH_3 [19] with consequent material porosity and permeability increase [164]. The conversion is accompanied by the release of free water which results in a decrease in strength caused by higher porosity [164]. Depending on conditions the conversion process can last up to several years [51]. The conversion process reaction scheme is (12) [3,51,165].

$$\begin{array}{c} 3C_2AH_8 \rightarrow 2C_3AH_6 + AH_3 + 9H \\ 3CAH_{10} \rightarrow C_3AH_6 + 2AH_3 + 18H \end{array} \quad (12)$$

The negative effects of the conversion can be cushioned by curing at temperatures higher than 50 °C and using W/C (Water/Cement ratio) not superior to 0.4 [38,61,166,167]. Mineral additives such as silica are also used, which leads to the formation of aluminum-silicate phases, but the mechanisms of their formation are not yet clear [168,169].

The main phases hydrated as a result of the reaction of $C_{12}A_7$, CA and CA_2 with silica and water at 40, 65 and 95°C are katoite of the type $Ca_3Al_2(SiO_4)_{3-x}(OH)_{4x}$ [169], with x in the range $0 \leq 3\text{-}x \leq 0.334$ and gibbsite $Al(OH)_3$. For a temperatures below ≤ 90 °C and (W/C=2) the crystal phase of gehlenite of the type $Ca_2Al_2SiO_7.8H_20$ is exhibited [169]. Other studies show [170,171] that various phases are formed, such as the hydrogarnet solid solution of the type $Ca_3Al_2(SiO_4)_{3-x}(OH)_{2x}$, $C_3AS_{3-x}H_{2x}$, with x in the range $0 \leq x \leq 3$, and gehlenite or stratlingite of the type C_2ASH_8. Stratlingite reacts with calcium oxide and initially inhibits the formation of C_2AH_8 and C_3AH_6 after the conversion [169,171–173].

The reaction of the anhydride phases of CAC, with a ratio (W/C = 0.5) and increasing additions between 25 - 50 wt% of silica does not show the formation of the gehlenite phase $Ca_2Al_2SiO_7.8H_2O$ [35,168,174]. The hydration reactions for CAC with the additions of silica, follow the scheme of reactions (13) where the stratlingite could crystallize in a stable phase in the temperature range $T \sim 20 - 90°C$ [17].

$$\left.\begin{array}{c} CAH_{10} + S \rightarrow C_2ASH_8 + AH_3 + 9H \\ CAH_{10} + CSH \rightarrow C_2ASH_8 + 3H \\ C_2AH_8 + 2CSH + AH_3 + 3H \rightarrow 2C_2ASH_8 \\ C_2AH_8 + AH_3 + S \rightarrow C_2ASH_8 + 3H \\ C_2AH_8 + S \rightarrow C_2ASH_8 \end{array}\right\} \quad (13)$$

When the hardened paste of CAC is heated to 800 °C, the dehydration generates the conversion process $CAH_{10} \rightarrow C_2AH_8 \rightarrow C_3AH_6$ [30]. The dehydration process ends during heating to 800 °C and $C_{12}A_7$ is formed which, after heating to a temperature of 1000 °C or higher, crystallizes in CA or CA_2 [22,30]. Antonovič et al [38] add to this by stating that, in addition to $C_{12}A_7$, the mineral phases CA, CA_2 are also formed at 800 °C and are independent of the curing temperature and $C_{12}A_7$ predominates.

CACP without additives present severe damage when subjected to temperatures equal to or higher than 500 °C [175,176]. Thermal micro cracking occurs in the pastes, due to thermal gradients and thermal expansion anisotropy within individual mineral phases [144,177]. Knowledge of the behavior at high temperatures of the hydrated phases of calcium aluminate cement pastes and quantification of the damage generated, is fundamental for further research leading to the improvement of their mechanical behavior [142,178]. Therefore, in this aspect the main contribution is made with the present work.

In this study different formulations of calcium aluminate cement pastes (CACP) with 51wt% (wt% -percentage by weight) of Al_2O_3 (CACP 51) were made at 0.4 water to cement ratio (W/C) with additions of 0 wt%, 10 wt% and 20 wt% silica (CACP 51-0 wt%, CACP 51-10 wt% and CACP 51-20 wt%, respectively). All samples were exposed to oxidative environment for 4 hours at 1000˚C, in a furnace under an air atmosphere.

The behavior of the constituent phases according to the temperature was also studied through TGA and DTG. The characterization was done using SEM, XRF, XRD, the Williamson-Hall Model (WHM)) and FTIR. Compression, absorption, density and porosity tests were done. It is observed that: $C_{12}A_7$ decreases between 800 °C and 1000 °C while the quantity CA and CA_2 increases, silica improves compression strength at 20 °C and 1000 °C, Silica favors the formation of C_2ASH_8 and avoids the conversion process of the CAC pastes. Knowledge of the behavior of the CACP added with silica between the temperatures of 20 °C to 1000 °C, is essential to understand its behavior at higher temperatures. A review of the state of the art shows an incipient literature in this aspect, for this reason this research is relevant for the refractory industry based on CACP with silica.

6.2 EXPERIMENTAL

6.2.1 SAMPLES MANUFACTURE

Three types of samples of CACP 51 wt% were fabricated with W/C = 0.4 and additions of high purity micro silica (SiO_2) with 10 wt% and 20 wt%, while samples with 0 wt% were prepared for use as a reference see Table 20. The micro silica presents a 98% purity, granulometry of 2 µm and was obtained from a Colombian natural source. All cement pasted were fabricated at 20 °C and were kept closed to air contact for 48 hours (in order to avoid pre-carbonation). They were then released from molds and subjected to 48 hours of hydration covered with water to 5 mm above their surface. Thereafter, the samples were removed from water and allowed to dry in air for 24 h. Sample dimensions were 19 mm in diameter and 22 mm in height. Additionally, the samples were heated at 1000 °C with a holding time of 4 hours in a Nabetherm GmbH 30-3000 °C LT 9/12P330 furnace, both heating and cooling were performed at a rate of 1.67 °C/min, for damage analysis and thermal stability.

Table 20. Formulations fabricated for cement paste sample with additions of silicon oxide

Formulations				
No	CEMENT	W/C	SiO_2 wt%	T (°C)
1			0	
2	CACP 51 wt%	0.4	10	20
3			20	

6.2.2 CHARACTERIZATION OF THE CAC PASTES

The chemical composition of the CAC powder was investigated by XRF in a Thermal spectrometer model OPTIM'X as shown in Table 21 .

Table 21. Chemical composition of raw CAC powders.

Sample	Chemical Composition (wt%)								
	Al_2O_3	CaO	SiO_2	TiO_2	Fe_2O_3	K_2O	P_2O_5	ZrO_2	MoO_3
CAC51 wt%	52.12	37.82	5.25	1.87	1.81	0.128	0.108	0.086	0.052

The distribution of granulometry of the CAC powder was determined by laser diffraction, which showed an average grain size of 4 µm. Porosity, density and absorption were established under the tests and requirements established in the international standard ASTM C 642-97 for CACP. The mass measurements required by this standard were performed with a Mettler Toledo AB204 balance with a sensitivity of 0.1 mg. XRD characterization was done in a X'Pert PRO diffractometer with Cu K radiation of 1.5406 A°. Scanning was performed for 2θ between 5 and 70°, with a step size of 0.02°.

XRD interpretation, phase identification, Rietveld refinement, and analysis of the crystallite size and micro strains (by the Williamson-Hall method) were performed with the X'Pert High Score Plus/Panalytical software. For the elimination of the K-alpha 2 peak, the Rachinger model was used, a background with a granularity of 20 and bending factor of 1. For the diffraction peak search, the minimization method of the second derivative was used. A JEOL JSM – 6490 scanning electron microscope (SEM) equipped with energy dispersive X-ray microwave was used to analyze the morphology and composition of samples of all formulations. Secondary electrons were used for a better definition of the surface texture.

FTIR measurements were conducted in a Shimadzu IR Tracer-100 with a scanning range (cm^{-1}): of 400-4000, the test was performed by ATR with Resolution 4 and of 16 cycles. Tests for thermal gravimetric analysis (TGA) were performed in an TGA Q500 V20.8 devices. Purge gas conditions las Purity Composition Moisture Nitrogen 99.995% N_2. Oxygen 99.980% O_2, at a rate of 10 °C/min. The analysis of physical and mechanical properties and chemical composition was performed on the samples before and after the thermal treatment, in order to ascertain their effect of on these properties. The compression tests were conducted in a universal Shimadzu Autograhp apparatus at a cross head speed of 1mm/min.

6.3 ANALYSIS AND RESULTS

6.3.1 ANALYSIS BY XRD AND PHASE IDENTIFICATION

The identification analysis of hydrated phases of CACP 51-0 wt% at 20 °C, confirmed the formation of CAH_{10}, C_2AH_8, AH_3, as shown in Figure 22a, as established in the literature

[3,19,33,163,174,179]. The identification analysis of hydrated phases of CAC 51-10 wt% and 20 wt% at 20 °C, confirmed the formation of CAH_{10}, C_2AH_8 and C_2ASH_8 [170,174,180,181] (see Figure 22b and 1c). It can be seen that the influence of silica restricts the formation of AH_3, which implies that for these formulations of silica retards the conversion effect. Figure 22a, corresponding to compositions with 0 wt%, show that the intensity of the peaks associated with C_2AH_8, drastically decrease in the formulations added addition of silica, Figure 22b, 1c. This is because part of C_2AH_8 reacts with S or AH_3, in accordance with $C_2AH_8 + AH_3 + S \rightarrow C_2ASH_8 + 3H$ or $C_2AH_8 + S \rightarrow C_2ASH_8$ [17], to form C_2ASH_8. Hence, the silica also restricts the formation of C_2AH_8 and thus retards the effects of the conversion. Silica favors the formation of C_2ASH_8.

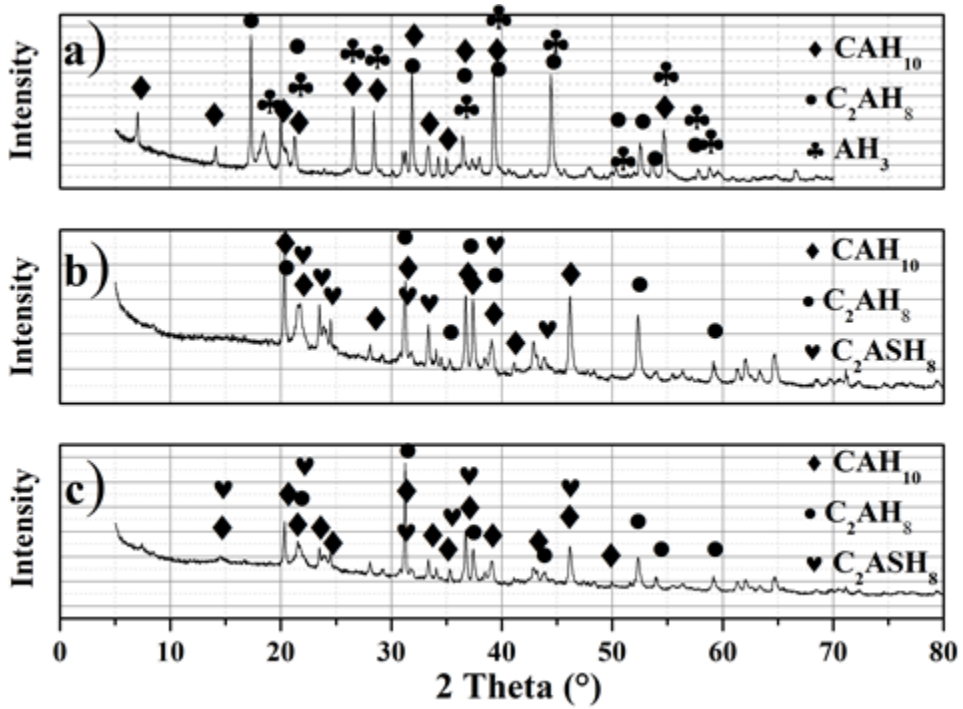

Figure 22. XRD, W/C=0.4, T=20°C. CACP: a) 0wt%; b) 10wt%; c) 20wt%.

The Bragg-intensity, R(Bragg), is given by equation (14):

$$\mathrm{R(Bragg)} = \frac{\sum_{hkl}|F_{hkl}(obs) - F_{hkl}(calc)|}{\sum_{hkl} F_{hkl}(obs)} \quad (14)$$

Where $I_{hkl} = mF_{hkl}^2$, (m=multiplicity) and I_{hkl} is the intensity of each peak. This can be used to monitor the improvement in the structural model [182]. It is accepted as a good refinement when R(Bragg) < 10. R(Bragg)s is calculated with X'Pert High Score Plus/Panalytical software.

Figure 23a shows the diffractogram of CACP 51-0 wt% subjected to 1000 °C. It can be seen that CA, CA_2 and $C_{12}A_7$ phases were formed. For CAC 51-0 wt%, CA, R(Bragg) = 3.08; CA_2, R(Bragg) = 3.54 and $C_{12}A_7$, R(Bragg) = 3.14.

Figure 23b and 23c show the diffractogram of CACP 51-10 wt% and 20wt% subjected to 1000 °C. It can be seen that CA, SiO_2 and $C_{12}A_7$ phases were formed.

- For CACP51-10 wt%, CA, R(Bragg) = 5.21; SiO_2, R(Bragg) = 4.26 and $C_{12}A_7$, R(Bragg) = 3.57.
- For CACP51-20 wt%, CA, R(Bragg) = 5.86; SiO_2, R(Bragg) = 6.93 and $C_{12}A_7$, R(Bragg) = 5.32.

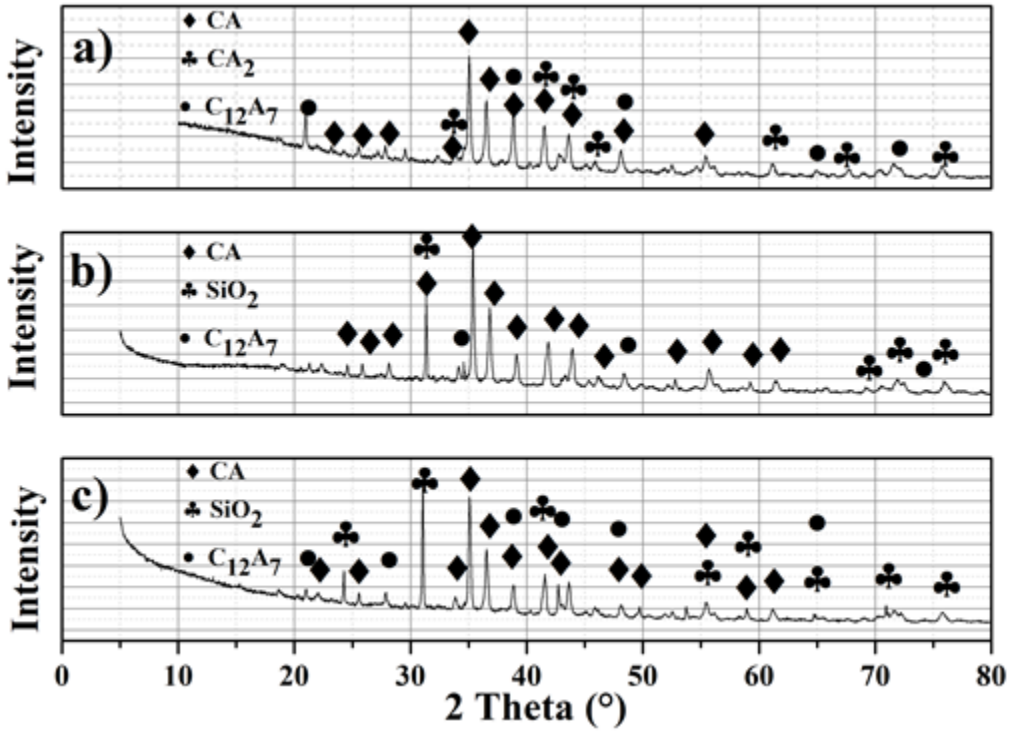

Figure 23. XRD, W/C=0.4, 1000°C. CACP: a) 0wt%; b) 10wt%; c) 20wt%.

6.3.2 RIETVELD REFINEMENT ANALYSIS

The Rietveld analysis was performed with the polynomial method. The order of the background, the unit cells, the atomic coordinates and width and shape of the peaks were refined in each phase. Table 22 shows all the parameter values obtained from the Rietveld refinement for all formulations subjected to 1000 °C. The parameters a good Rietveld refinement are defined as [50]: Rp: Residual of least-squares refinement. R_{wp}: weights residual. Rexp: evaluates the quality of the data. GOF: Goodness of fit; compares R_{wp} to Rexp. It is calculated from equation (15).

$$\text{GOF} = \chi^2 = \left[\frac{R_{wp}}{Rexp}\right]^2 \quad (15)$$

It would be a perfect fit, but you want GOF <4 and the fit are acceptable for GOF < 10 and $R_p < 10$.

Table 22. Rietveld refinement parameter – 1000°C: W/C=0.4

Formulations	Rexp	Rp (<10)	Rwp	GOF (<10)
CACP 51-0 wt%	2.92	4.23	5.21	3.18
CACP 51-10 wt%	3.17	6.14	8.23	6.74
CACP 51-20 wt%	3.20	6.73	8.17	6.52

Figure 24 shows the quantification of the phases obtained by Rietveld analysis in CACP 51-0wt%, 10wt% and 20wt%, W/C = 0.4, subjected to 1000 °C. CACP51-0wt% forms the phases CA, CA_2 and $C_{12}A_7$ with 50.5%, 45.9% and 3.6% respectively. CACP51-10wt%, forms the phases CA (82%), $C_{12}A_7$ (9.9%) and SiO_2 (8.1%). CACP51-20wt%, forms the phases CA (72%), $C_{12}A_7$ (7.5%) and SiO_2 (20.2%).

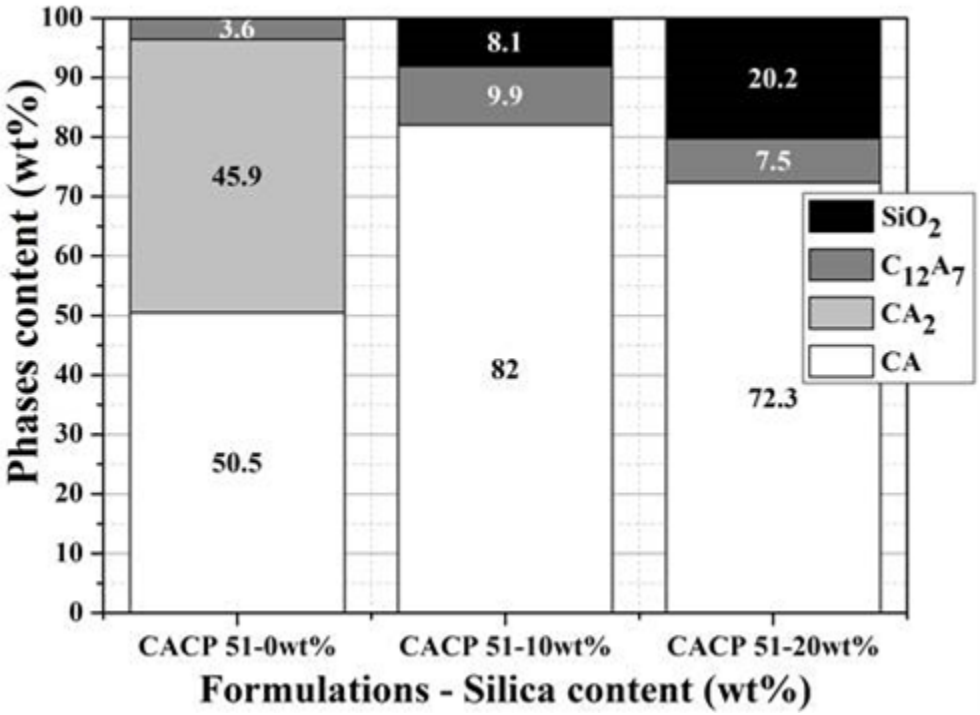

Figure 24. Quantification of phases by Rietveld refinement: W/C=0.4, T=1000°C.

6.3.3 FTIR ANALYSIS

Figure 25a and 25b, show the results of FTIR analysis for CACP 51-10 wt% and CACP 51-20 wt% at 20 °C, in the range of 400-1200 wavenumbers (cm^{-1}). It can be seen that stratlingite is formed at very low wavenumbers and transmittance. The value of the wavenumbers for the transmittance bands for Figure 25 are summarized in Table 23 . Figure 25a and 25b, corroborates the formation of hydrated phases, identified by XRD tests (see Figure 22b and 1c)

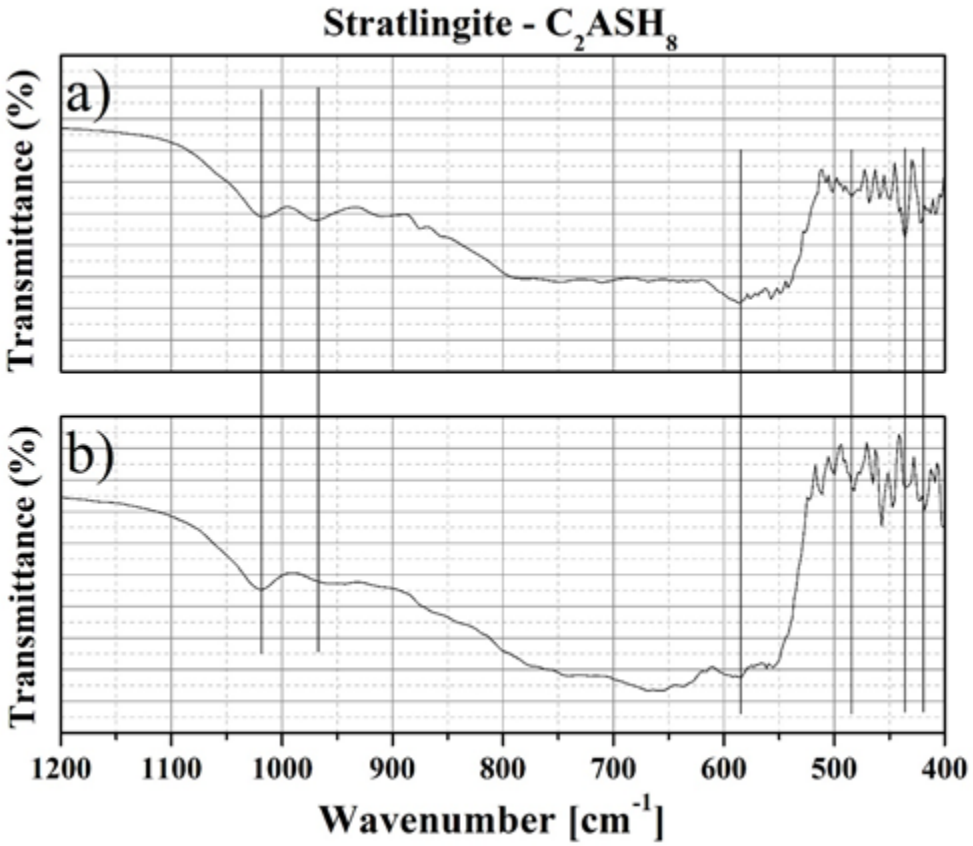

Figure 25. FTIR: W/C=0.4: CACP 51- 0 wt%: a) 20°C, b) 1000°C

Figure 26a and 26b show the results of FTIR analysis for CACP 51-0 wt% at 20 °C and CACP 51- 0wt% at 1000 °C, respectively. For 20 °C in the 1000-4000 range wavenumbers (cm^{-1}) and for 1000 °C in the 400-1000 range. Transmittance bands are observed only in these ranges. Figure 26a corroborates the formation of hydrated phases, identified by XRD tests (see Figure 22a) and Figure 26b corroborates the formation of anhydrous phases, identified by XRD tests (see Figure 23a). The value of the wavenumbers for the transmittance bands for Figure 26a are summarized in Table 24 and for Figure 26b in Table 25.

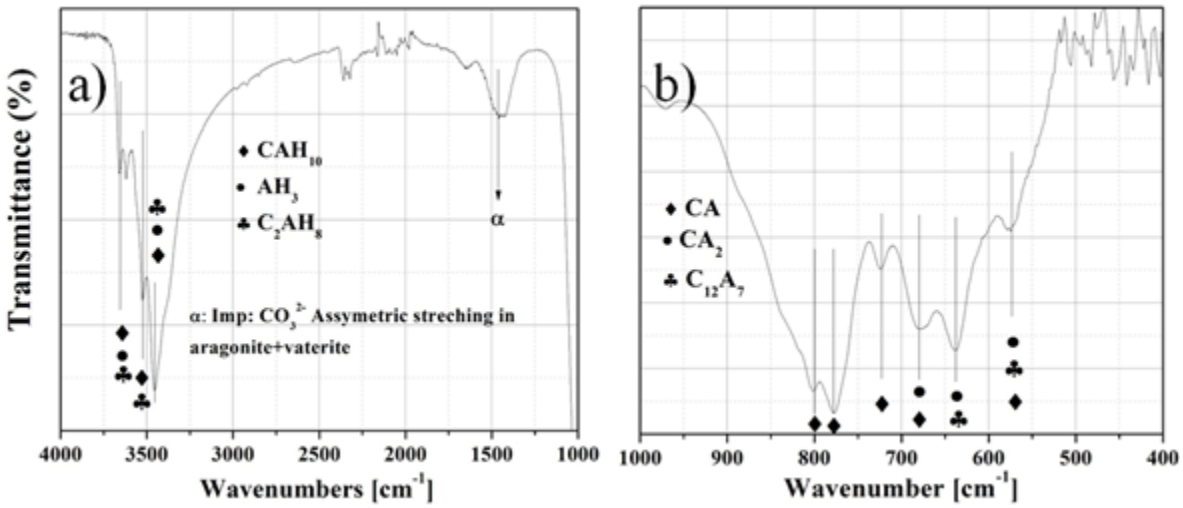

Figure 26. FTIR, 1000°C, W/C=0.4:
a) CACP 51-10wt%, b) CACP 51-20wt%, 4000-1000 and 400-1000 cm^{-1} respectively.

Table 23. FTIR – wavenumbers values for Stratlingite

Wavenumber [cm^{-1}]	Assignment	Reference
1016, 913, 911, 855, 710, 709, 477, 475, 472, 418, 417, 416.	Si–O–Al- Stratlingite	[183]
1020, 965, 860, 710, 590, 530, 455	Si–O–Al- Stratlingite	[184]
969.17, 907.89, 585.67, 485.17, 435.06, 421.25 [51-10-20] [51-20-20]	Si–O–Al- Stratlingite	This work

Figure 27a and 27b show the results of FTIR tests for CACP 51-10 wt% and CACP 51-20 wt% at 20 °C in the range between 1000 and 4000 wavenumbers (cm^{-1}). The formation of the phases detected by XRD is verified and no different phases were detected with FTIR analysis. The value of the wavenumbers for the transmittance bands for Figure 27a and 27b are summarized in Figure 27a and 27b, corroborate the formation of hydrated phases, identified by XRD (see Figure 22b and 22c).

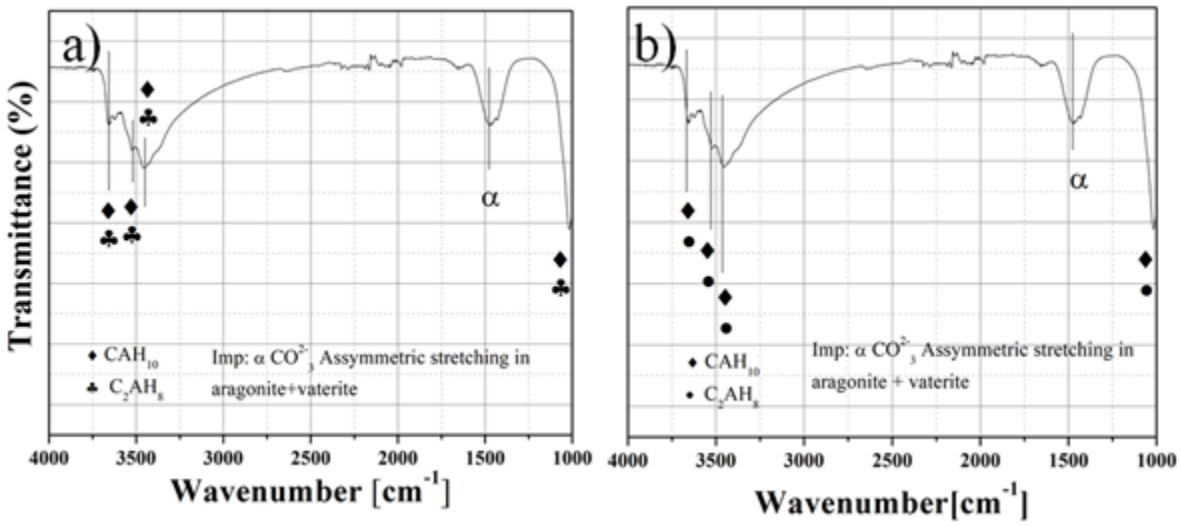

Figure 27. FTIR: 20°C, W/C=0.4, a) CACP51- 10 wt%, b) CACP51-20wt%.

Table 24. Assignments of FTIR transmittance Bands:
20°C: CACP51-0, 10 and 20wt%, W/C= 0.4.

Wavenumber [cm^{-1}]	**Assignment**	**Reference**
3666 – 3665 – 3662 – 33661	O-H stretch in hydrogarnet	[161,170,185]
3659.45[51– 0 – 20] [51– 10 – 20] 3671.06 [51– 0 – 20] [51– 20 – 20] 3659.47 [51– 0 – 20]	O-H stretch in hydrogarnet	This work
3529 – 3527 – 3525 – 3524	O-H stretch in gibbsite	[170,186,187]
3522.59 [51– 0 – 20] [51– 10 – 20] 3528.71[51– 20 – 20]	O-H stretch in gibbsite	This work
3471 – 3469 – 3468– 3467	O-H stretch in gibbsite	[170,186,187]
3464.29 [51– 20 – 20] 3457.21 [51– 10 – 20]	O-H stretch in gibbsite	This work
1646 –1641–1640 –1639 –1637	O-H bending water	[185]
1486 –1485 –1482 –1481	CO^{2-}_3 Asymmetric stretching in aragonite+vaterite	[170,188]
1474 [51– 10 – 20] 1468.55 [51 – 20 – 20]	CO^{2-}_3 Asymmetric stretching in aragonite+vaterite	This work

1429 –1420 –1418 –1416	CO^{2-}_3 Asymmetric stretching in calcite	[188]
1366 –1364	CO^{2-}_3 Asymmetric stretching in C_4AcH_{11}	[189,190]

Figure 28 shows the results of FTIR, T=1000°C, W/C = 0.4 of CACP 51-10wt% and 20wt%. The phases detected by XRD are observed. The values of the observed transmittance peaks are summarized in Table 25.

Figure 28a and 28b, corroborates the formation of hydrated phases, identified by XRD tests (see Figure 23b and 22c)

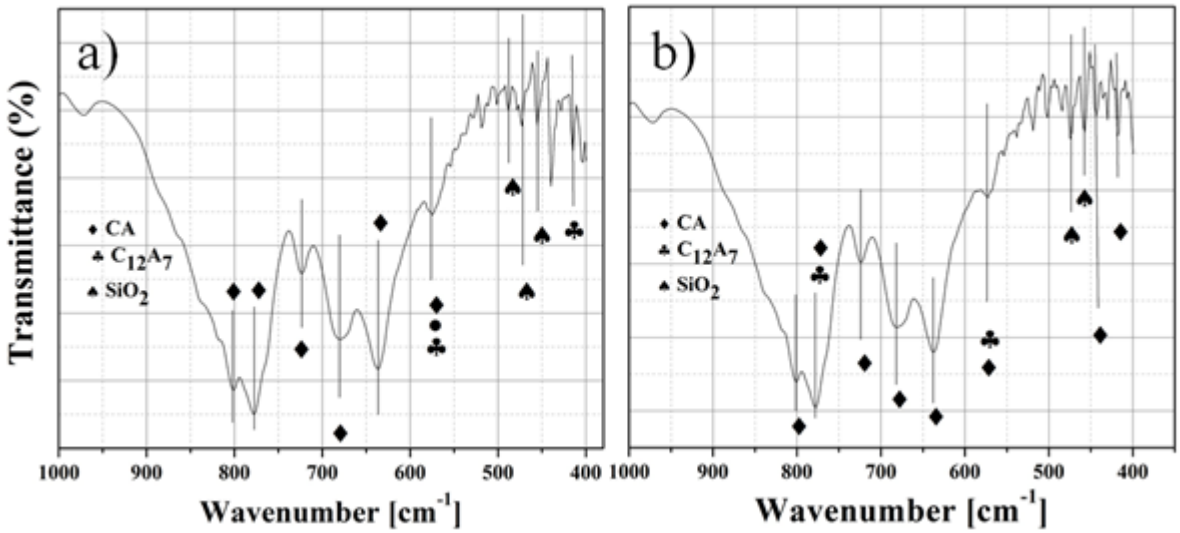

Figure 28. FTIR, 1000°C, W/C=0.4: a) CACP 51-10wt%, b) CACP 51-20wt%. 400-1000 cm^{-1}.

Table 25. Assignments of FTIR Transmittance Bands:
1000 °C: CACP51-0, 10 and 20wt%, W/C= 0.4

Wavenumber [cm^{-1}]	**Assignment**	**Reference**
805 – 804	AlO_4 vibration in CA	[31,113,115,116,155]
801.97 [51– 0 – 1000] [51– 10 – 1000] 801.38 [51– 20 – 1000]	AlO_4 vibration in CA	This work
780	AlO_4 vibration in CA AlO_4 vibration in $C_{12}A_7$	[31,113,115,116]
777.48[51– 0 – 1000] [51– 10 – 1000] – 779.55 [51– 20 – 1000] 776.89 [51– 0 – 1000]	AlO_4 vibration in CA AlO_4 vibration in $C_{12}A_7$	This work

745	AlO_4 vibration in CA_2	[113,115]
744.72 [51– 0 – 1000]	AlO_4 vibration in CA_2	This work
720	AlO_4 vibration in CA	[31,113,115,116,155]
723.43[51– 10 – 1000] – 724.21 [51– 20 – 1000]	AlO_4 vibration in CA	This work
680 - 677	AlO_4 vibration in CA_2 AlO_4 vibration in CA	[31,113,115]
681.77[51– 10 – 1000] – 680.39 [51– 20 – 1000]	AlO_4 vibration in CA_2 AlO_4 vibration in CA	This work
640	AlO_4 vibration in CA_2 AlO_4 vibration in CA	[31,113,115,116,155]
636.30 [51– 0 – 1000] [51– 10 – 1000] – 638.04 [51– 20 – 1000]	AlO_4 vibration in CA_2 AlO_4 vibration in CA	This work
573 – 570	AlO_4 vibration in CA_2 AlO_4 vibration in CA AlO_4 vibration in $C_{12}A_7$	[31,113,115,116,155]
576.20 [51– 10 – 1000] 573.70 [51– 20 – 1000]	AlO_4 vibration in CA_2 AlO_4 vibration in CA AlO_4 vibration in $C_{12}A_7$	This work
478 – 477– 455 – 453	SiO_4 bending vibration of quartz	[185]
487.81 [51– 10 – 1000]	SiO_4 bending vibration of quartz	This work
478 – 477– 455 – 453	SiO_4 bending vibration of quartz	[185]
471.91 – 454.74 [51– 10 – 1000] 473.36 – 457.87 [51– 20 – 1000]	SiO_4 bending vibration of quartz	This work

422 – 420	AlO_4 vibration in CA_2 AlO_4 vibration in CA	[31,113,115,116,155]
414.20[51– 10 – 1000] 418.02 [51– 20 – 1000]	AlO_4 vibration in CA_2 AlO_4 vibration in CA	This work

6.3.4 SEM ANALYSIS

Figure 29a, 29b and 29c shows SEM images of CACP 51-0, 10 and 20 wt%, respectively, with W/C = 0.4 at 20 °C. For CACP 51-0 wt%, phases of CAH_{10}, AH_3 and C_2AH_8 are observed. For CACP 51-10 wt% and 20 wt%, phases of C_2ASH_8, CAH_{10} and C_2AH_8 are observed. The phases CAH_{10} and C_2AH_8 are hexagonal [31,171,191–194] and the phases AH_3 and C_2ASH_8 are cubic and elongated [192,193]. Figure 29d and 28h show SEM images pure silica, on a scale of 100 and 1 µm, respectively.

Figure 29e shows SEM images of CACP 51-0 wt%, W/C=0.4 at 1000 °C. Phases CA, CA_2 and $C_{12}A_7$ were observed [195,196]. Figures 29f and 29g show SEM images of CACP 51-10 wt% and 20 wt%, respectively, with W/C=0.4 at 1000 °C. Phases of CA, CA_2, $C_{12}A_7$ and SiO_2 were observed [195–197]. These structures could be attributed to the path's roads produced by the evaporation of water, the redistribution of products formed by dehydration, changes in morphology and structure, changes in density and pores formed in the initial conversion processes. Unfortunately, it would be very complex to separate all these effects.

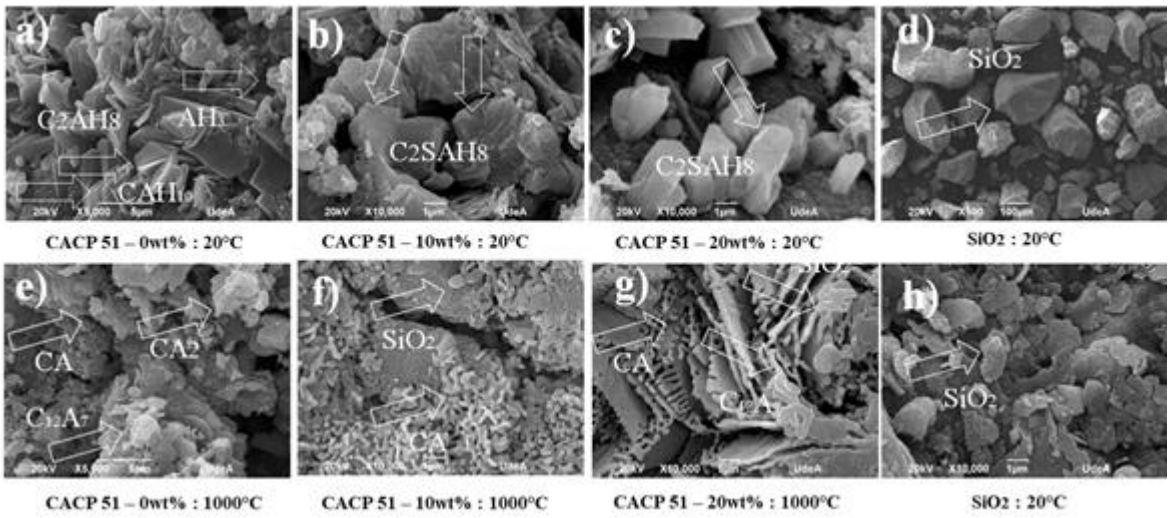

Figure 29. SEM – CACP 51-0, 10 and 20wt%, W/C=0.4 – 20°C and 1000°C.

6.3.5 CRYSTALLITE SIZE AND MICROSTRAIN ANALYSIS

The Williamson-Hall method was used for each formulation with the following parameters in the X'Pert High Score Plus/Panalytical software: FWHM (Full Width at Half Maximum) plot mode: FWHM; FWHM curve fit type: Caglioti function and Williamson-Hall; plot type: Linear Williamson-Hall Plot.

The distance d between adjacent planes in the Miller indices (hkl) in a crystalline structure can be calculated from Bragg's law $\lambda = 2dsin\,\theta$, λ is the wavelength of x-rays and θ is the angle between the incident rays and the scatter planes [198]. However, the peak width derived from crystallite size varies as $1/\cos\theta$, whereas strain varies as $\tan\theta$. This difference in behavior as a function of 2θ enables one to discriminate between the size and strain effects on peak broadening. The distinct θ dependencies of both effects laid the basis for the separation of size and strain broadening in the analysis of Williamson and Hall [199,200], using equation (16) :

$$\beta_{hkl} = \left(\frac{k\lambda}{D\cos\theta}\right) + (4\epsilon\tan\theta) \tag{16}$$

Where β_{hkl} is the peak width at half-maximum intensity, k is a constant equal to 0.94, D is the particle and ϵ is the Strain-induced broadening arising from crystal imperfections and distortion. Figure 30a, 30b and 30c show the results of the numerical adjustment for micro strain for the formulations CACP 51-0, 10 and 20 wt%, respectively. The values obtained for the micro strains are: 0.22, 0.19 and 0.21% respectively. It can be observed that the non-silica formulation has the highest percentage in the micro strain, so it can be conjectured that the silica content restricts the micro strains. Figure 30d, 30e and 30f show the results of the numerical adjustment for crystallite size: for the formulations CACP 51-0, 10 and wt%, respectively. The values obtained for the crystallite size are: 453, 533 and 466 Å respectively. It can be observed that the formulation with 10 wt% of silica has a larger crystallite size.

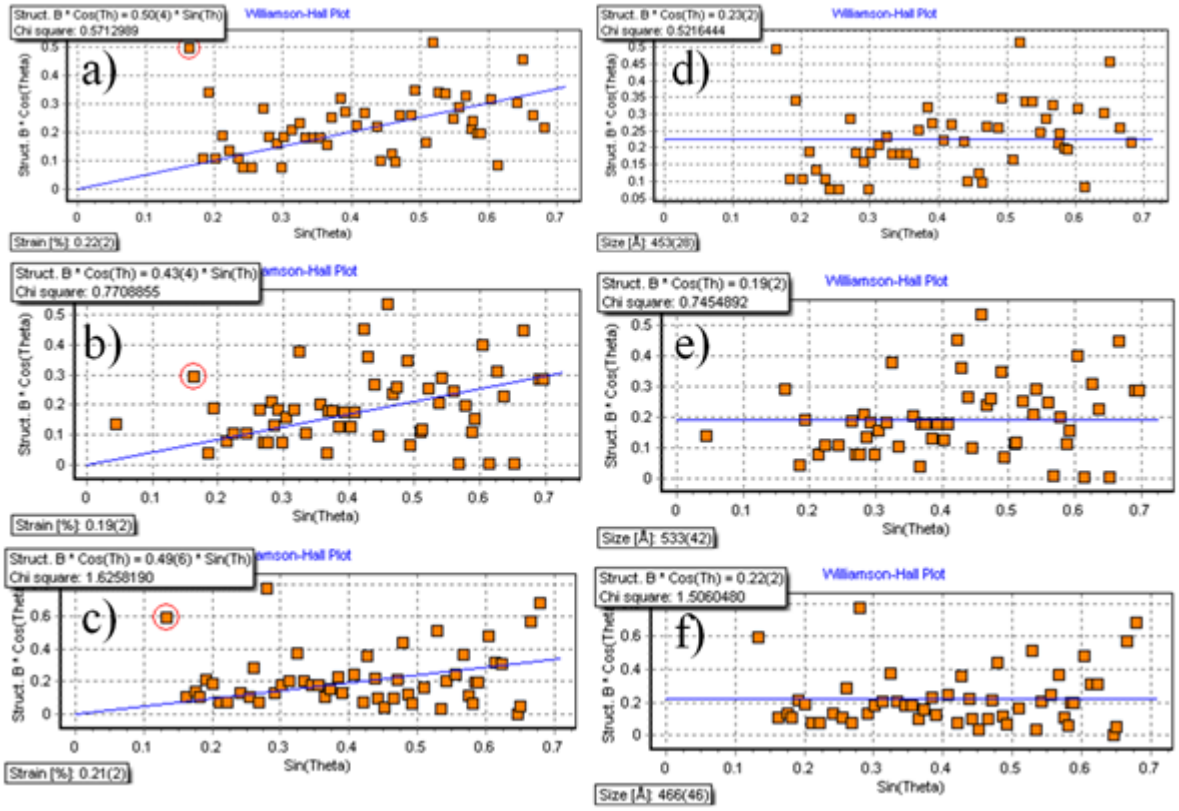

Figure 30. 1000°C - W/C=0.4: Williamson-Hall Method: Microstrain:
CACP 51: a) 0wt%, b) 10wt% and c) 20wt%. Crystallite size: d) 0wt%, d) 10wt% and d) 20wt%.

6.3.6 TGA – DTG ANALYSIS

Table 26 summarizes the decomposition temperatures of CAC hydration products in °C according to various studies and those that were found in this work.

Table 26. Decomposition temperatures of CAC hydration products:
T (°C), according to various studies and this work.

Reference	Method	CAH_{10}	C_2AH_8	C_2ASH_8	C_3AH_6	AH_3-gel	AH_3	$Al(OH)_3$
This work – CACP 51-0 wt%	TGA-DTG	115.23	239.70	–	317.93	–	293.88	–
This work – CACP 51-20 wt%	TGA-DTG	–	–	235.97	306.57	–	297.50	–
Schneider [201]	DTA	~ (155 & 285)	–	–	–	–	–	–

Heikal et al [202]	DTA	170	295	210-225	330	100	256	–
Ramachandran [203]	DTA	140–170	–	–	–	–	–	–
Barnes et al [204]	DTG	~125	–	–	~330	–	–	~290
Day et al [205]	DTG	–	–	–	–	100–200	–	3 steps ~550
Pope et al [85]	DTA	~110-120	–	–	~320–350	–	–	~295–310
George [159]	–	~140	~170	–	~300	~90	–	~280
Midgley [206]	DTA	~150	~230	–	~310	–	–	~275
Bushnell et al [207]	DTA	–	~190–200	–	–	~107–120	–	–
Das et al [208]	DTA	160–180 ~175	200–280 ~275	–	290–350 ~320	–	290–350 ~300	–
Guirado et al [39]	DTG	~(37,99&112)	–	–	–	–	–	–
Schmitt et al [209]	DTG	–	–	–	200–400	–	–	–
Fryda et al [210]	DTA	~150	~200	–	~330	–	–	~290
Cardoso et al [30]	–	120	170–195	–	240–370	100	–	210–300
Collier [211]	DTG	100–150	150–200	200–250	300–350 450–500	–	–	250–300 500–550
Bushnell et al [212]	DTG	100–150	140–200	192	~ 330	–	–	~230
Taylor [22]	DTG	100–150, 290			200–250		–	–
Kwan et al [213]	DTG	–	–	200		–	–	–
Scrivener et al [10]	DTG	–	–	200–230		–	–	–
Kalousek [214]	DTG	–	–	–	315–330	–	–	–

Passaglia [215]	DTG	–	–	–	250–310 450–550	–	–	–
Alwiit [216]	DTG	–	–	–	–	–	–	220–230 280–300 310–325 495–525
Mackenzie [217]	DTG	–	–	–	–	–	–	220–230 310–325 495–25 ~ 330
Scheinherrova et al [84]	DSC	100–150	80–200	–	290–350	–	260–330	–
Mostafa et al [65]	DSC	~100	~230	200–230	~300	–	~280	–
Lothenbach [218]	DTG	~100	140–200	–	~330	–	~280	–
Park et al [219]	DTG	~100	~130	–	~320	–	~280	–
Tchamba et al [220]	DTG	–	–	–	~300	–	~250	–
Tchamba et al [106]	DTG	~150	–	–	~320	–	–	–
Rambo et al [221]	DTG	–	~140	–	–	~100	~280	–
Maitra et al [222]	DTG	~220	–	–	~370	~100	–	–
Antonovic et al [38]	–	120	200	–	300	100	300	–
Zhu et al [223]	DTG	–	–	–	–	–	270-317	257-277
Pacewska et al [181]	DTG	–	180-220	180-220	–	20-180	220-370	–

Szczerba et al [83]	DTA	97.94	165.93	–	451.29	97.94	–	285.48
Made et al [224]	DTA	88.43	159.78	–	439.20	88.43	–	261.67
Pacewska et al [165]	DTG	95	125	180-220	280	96.54	220-370	–
Griffin et al [225]	TGA	–	–	–	340	–	–	300
Cardoso et al [226]	DTG	–	–	–	240-370	–	300	–

Figure 31a shows the TGA curve for CACP 51-0 wt%, there are four characteristic temperatures, 115.23 and 239.70 °C which can be associated with the dehydration of CAH_{10} and C_2AH_8 and the formation of AH_3 and C_3AH_6; 293.88 °C which can be associated with dehydration of AH_3 and 317.93 °C which can be associated with the dehydration of C_3AH_6. In the process of dehydration between 239.70°C and 317.93 °C a mass loss of 16.97 % equivalent to 6.26 mg is observed.

Figure 31b shows the DTG curve associated with the TGA curve for CACP 51-0 wt% silica and confirms the dehydration temperatures for AH_3 and C_3AH_6.

Figure 31c shows the TGA curve for CACP 51-20 wt%, four characteristic temperatures are observed: 129.87 °C, which can be associated with the dehydration of C_3AH_{10} [174], 235.97 °C with that of C_2ASH_8, 297.50 ° C with that of AH_3 and 306.57 °C with that of C_3AH_6. In the process of dehydration between 235.97 °C and 297.50 °C a mass loss of 17.56% is observed, equivalent to 3.37mg.

Figure 31d shows the DTG curve associated with the TGA curve for CACP 51-20 wt% and confirms the dehydration temperatures for AH_3 and C_3AH_6. These identifications are established based on the phases that have already been identified with XRD and FTIR, and are supported by the work of other researchers; see Table 26.

As the dehydration of AH_3 and C_3AH_6 occurs at very similar temperatures and the thermal energy for the dehydration of AH_3 is much greater than that of the dehydration of C_3AH_6, these dehydration peaks overlap in a slow sweep, for example at a10 °C/min [53], the rate used in this work. Therefore, the total thermal energies for the dehydration of phases AH_3 and C_3AH_6 are observed together in the same peak as observed in Figure 31b and 31d.

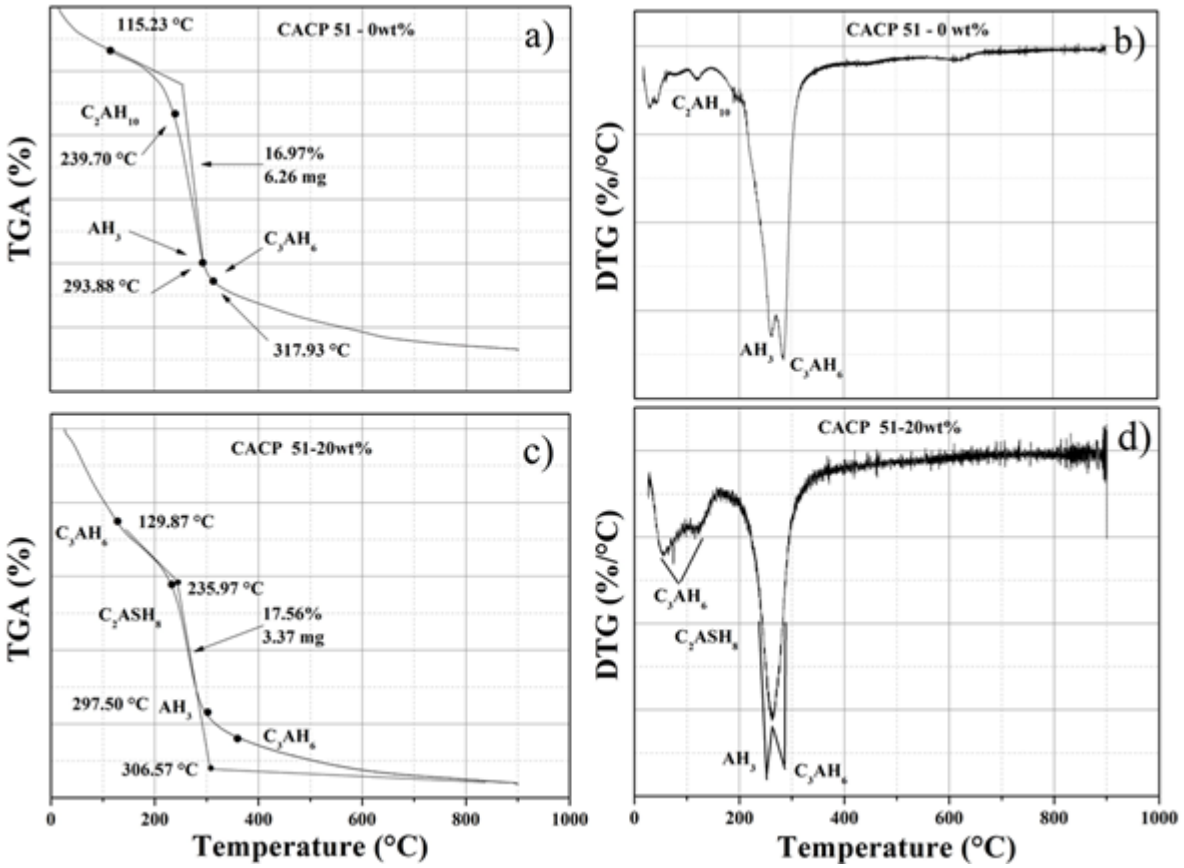

Figure 31. TGA curves: CACP 51: a) 0wt%, c) 20wt%. DTG curves: b) 0wt%, d) 20wt%.

6.3.7 POROSITY, DENSITY AND ABSORPTION ANALYSIS

Porosity, density and absorption were calculated under the tests and requirements established in the international standard ASTM C 642-97. The results of the calculations are summarized in Figure 32. All the results are for the CACP 51-0, 10 and 20 wt%. Figure 32a shows the density variation at 20 °C and after subjection to 1000 °C for 4 hours. It can be established that at 1000 °C the density decreases by 72, 76 and 73% for CACP 51-0 wt%, CACP 51-10 wt% and CACP 51-20 wt%, respectively. This shows that the higher the silica content, the greater the change in density.

Figure 32b quantifies the volume generated by the porosity for the different formulations. It can be observed that at 1000 °C the porosity increases significantly (with respect to the porosity at 20 °C) by 33.1%, 31.2% and 27.65% for CACP 51-0 wt%, CACP 51- 10 wt% and CACP 51-20 wt%, respectively. This shows that the formulation with higher silica content shows a greater increase in porosity. Figure 32c shows the absorption values for the different formulations, it can be seen that at 1000 °C the absorption increases significantly (with respect to absorption values at 20°C) by 31.1%, 33.28% and 25.91% for CACP 51-0 wt%, CACP 51- 10 wt% and CACP 51-20 wt%, respectively. This shows that the formulation with higher silica content shows less change in absorptivity.

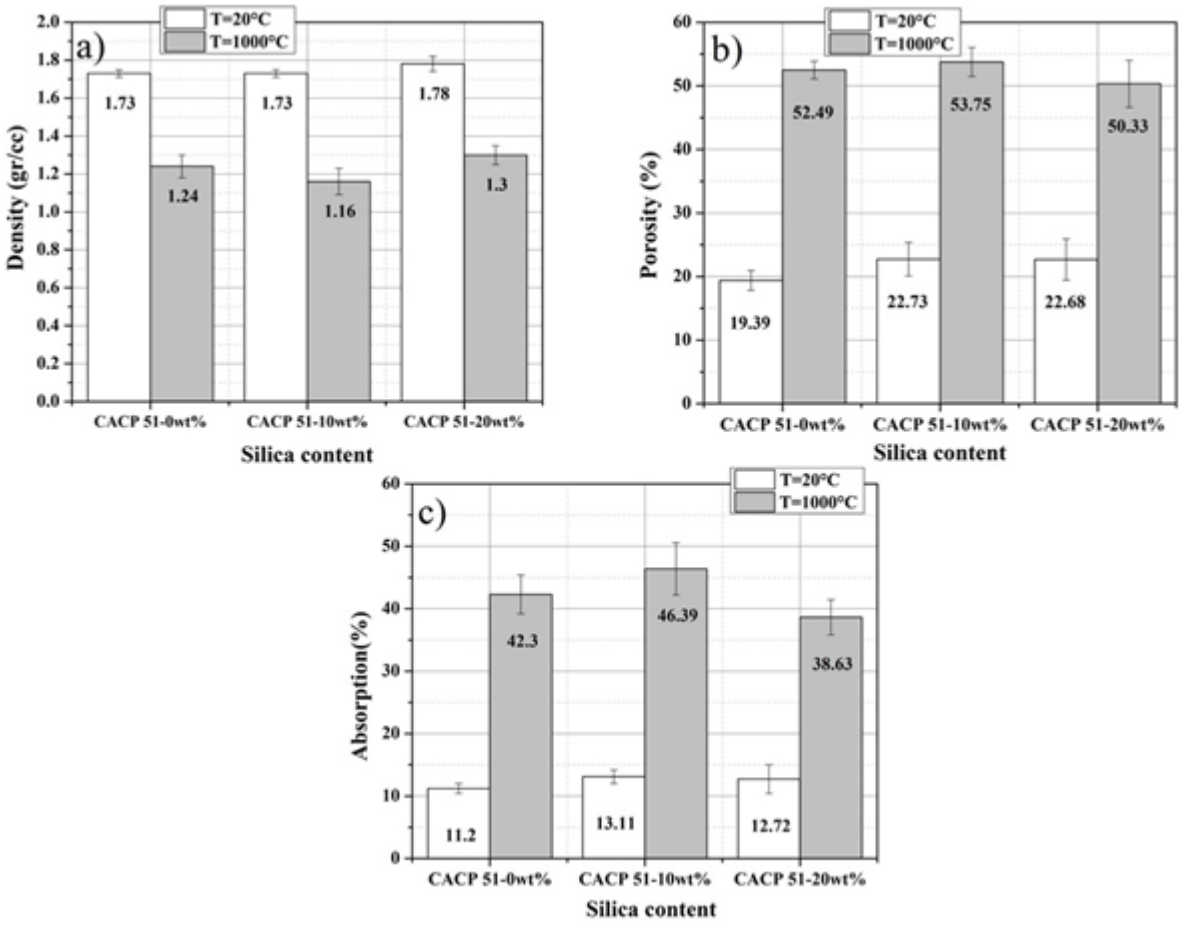

Figure 32. Results test according to the international standard ASTM C 642-97:
a) comparison of porosity, density and absorption, b) density, c) porosity and d) absorption.

6.3.8 DAMAGE ANALYSIS AND PROBABILITY CURVE

There are no analytical models similar to those used for the study of classical fracture in materials to describe and quantify damage, because all material constants change with temperature, which makes them inadequate models. Therefore, to quantify the damage generated by thermal effects, statistical and alternative methods are used, such as those used in this work. A proprietary method is used to quantify the damage caused by high temperatures. This consists of measuring the length of the cracks by means of digital image analysis, taking this length as damage parameter, then calculating the probability distribution. This methodology allows the relationship between the damage parameter, the porosity and the silica content to be established.

Figure 33a, 33b and 33c, show images of CACP 51- 0, 10 and 20wt% respectively, 20°C. Figure 33d, 33e and 33f, show images of CACP 51-0, 10 and 20wt% respectively, subjected to 1000 °C.

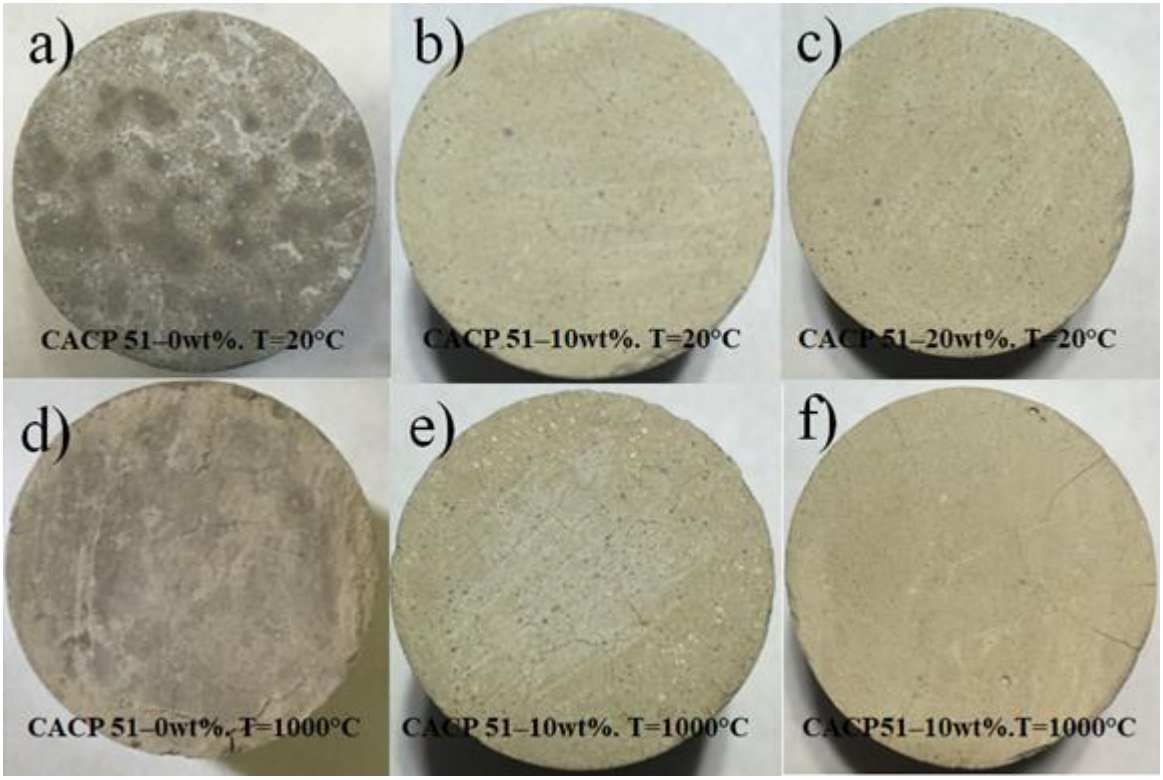

Figure 33. Images of CACP 51-0, 10 and 20wt% subjected to 20 and 1000 °C.

With the ImageJ software, the length of each crack was measured, and the total and average crack length was taken as a damage parameter. The mean value and the standard deviation of the different crack lengths are calculated and the probability distribution for the different formulations is calculated.

Figure 34a shows the probability distribution of average crack length of CACP 51-0wt%, 10wt% and 20wt%, subjected to 1000°C, respectively. It is observed that the highest probability values occur for CACP 51-10wt% of 15% average lengths of 7mm. It follows CACP 51-0wt% silica of 14.5% of average lengths 6.5mm and finally for CACP 51-20wt% silica of 11% of average lengths of 9.7mm. Note that for CACP 51-20wt% silica the probability is smaller but the average crack length is greater, which means greater damage. Figure 34b clearly shows that the formulations with higher silica content present greater damage.

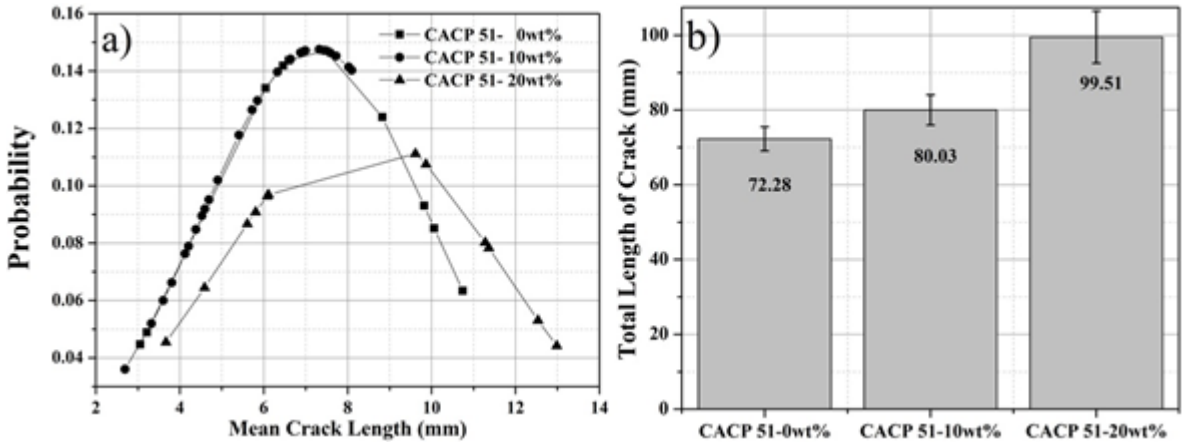

Figure 34. Statistical analysis:
a) Distribution of average crack length probability of CACP 51-0, 10 and 20wt% subjected to 1000 °C. b) Total length of crack in each formulation.

6.3.9 STRAIN STRENGTH

Figure 35 shows the compression strength at 20 and 1000°C for CACP 51-0, 10 and 20wt%. It can be observed that when the samples are subjected to 1000°C compression strength is lost in all the formulations. For CACP 51-0wt% there is a loss of 6.64 MPa (21.96%), for CACP 51-10wt% of 6.37 MPa (18.36%) and for CACP 51-20wt% of 4.51MPa (11.64%). This proves that silica improves compression strength at both 20 and 1000°C.

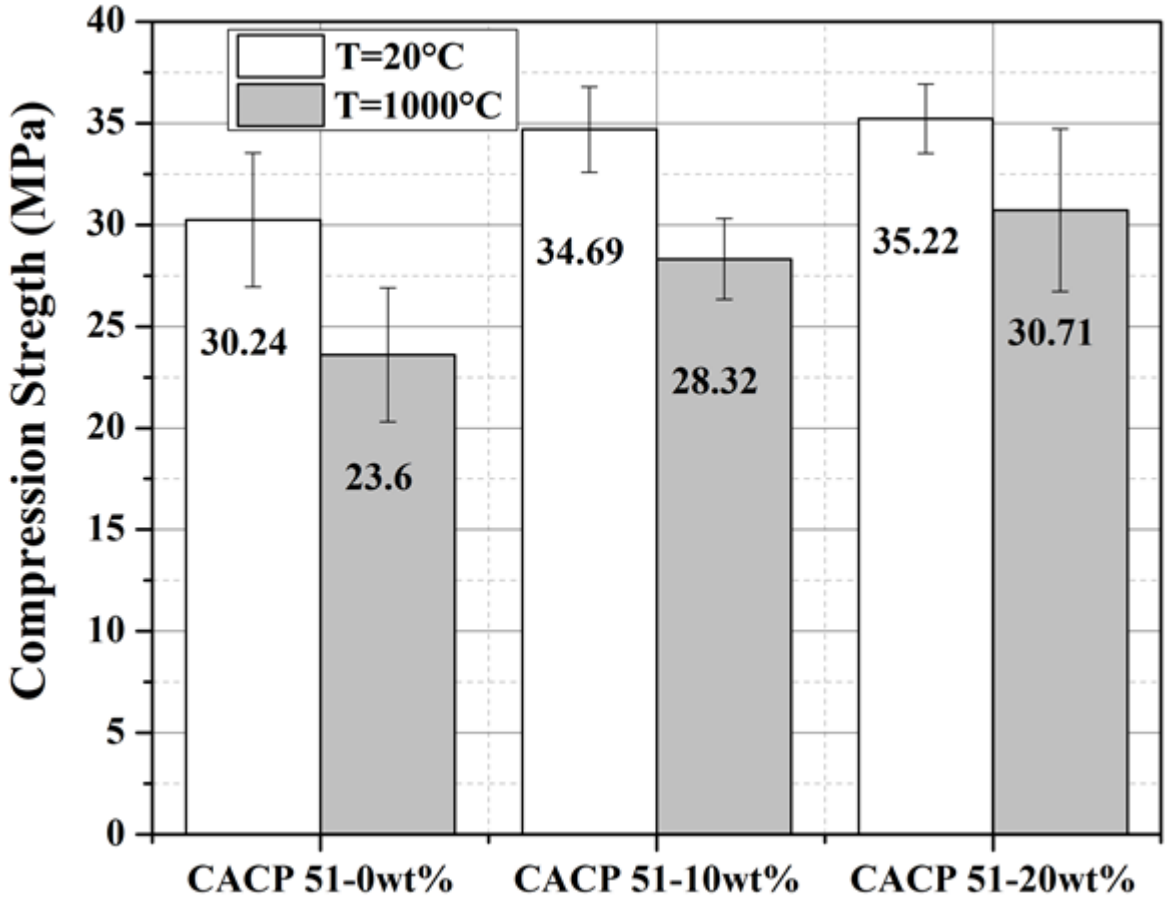

Figure 35. Compression strength

Figure 36 shows the comparison of LS (Loss of Strength), AD (Amount of Damage), PO (Porosity), LD (Loss of Density), CS (Crystallite Size), MS (Microstrain) and AB (Absorption) in the formulations of CACP 51wt% at 1000 °C.

In Figure 36a, it can be seen that the CACP 51-20 wt% formulation has the lowest loss of mechanical strength, implying that silica favors compressive strength, but at the same time this formulation shows greater cracking and a greater amount of damage. This can be explained due to the fact that the amount of damage was estimated by the size of cracks, for CACP 51-10 wt % at 1000 °C the cracks were greater in number but shorter in size, while for CACP 51-20 wt%, the cracks smaller in number but longer resulting in the effect explained above for the physical properties. This means that the mechanical strength was more influenced by the phases that were formed, so the mechanical strength was higher with the two silica formulations compared to the silica-free formulation.

Silica increased the porosity up to 1000 °C (see Figure 36b), the absorption and density of the formulation CACP 51-20 wt%, are lower than in the formulation CACP 51-10 wt% (see

Figure 36b and 36c, but the two silica formulations improved mechanical strength despite this.

From Figure 36c it can also be established that in silica formulations the lower the loss of strength, the higher the crystallite size, but the greater the number of microstrains, this increase in the micro strains due to the silica explains why these formulations have greater damage. In addition, the value for linear thermal expansion coefficient at 1000 °C reported in the literature for alumina is $10.3x10^{-6}$ °K^{-1} [227], while for silica this is $4.4x10^{-6}$ °K^{-1} [228]. This implies that the formulations with silica have greater micro strains compared to the formulation without silica, because of the sum of both strains.

From Figure 36d, it can be seen that the formulations with silica have greater porosity and greater damage, in accordance with what was discussed above.

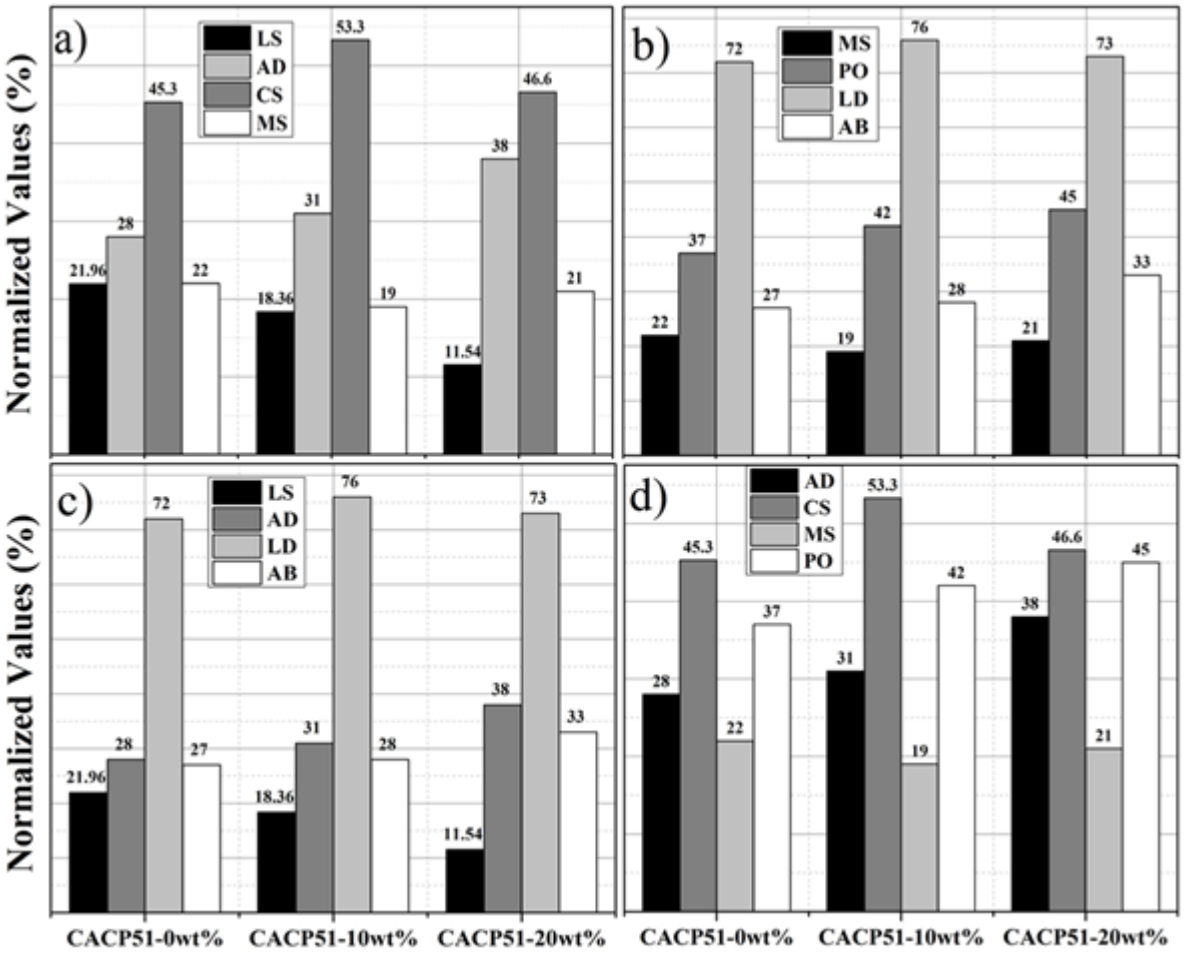

Figure 36. Analysis of the formulations CACP 51-0, 10 and 20wt% at 1000°C:

Factors: LS, AD, CS, MS, PO, LD and AB: a) LS, AD, CS and MS, b) MS, PO, LD and AB, c) LS, AD, LD and AB d) AD, CS, MS and PO.

6.4 DISCUSSION

In the formulations CACP 51-10 wt% and 20 wt% at 1000 °C the phase CA_2 is not observed and the formulation CACP 51-0 wt% at 1000 °C if you formed it (see Figure 23a, 22b, 22c,). This is because the silica restricts the formation of CA_2. The reasons for this come from the clinker of the CAC. We will analyze this in depth and in several steps.

1. CAC of low alumina content such as CAC 51 wt% does not contain the phase CA_2 [31] because the analysis of the binary diagram of phases $CaO - Al_2O_3$ of the CACs shows that CaO/Al_2O_3 ratios between 0.9 and 1.2 they have lower solidus & liquids temperatures than the CaO/ Al_2O_3 ratios than those that take values between 1.8 and 2.5 [29,229]. If the CaO/Al_2O_3 ratio is less than 1.0, that is, it is a low alumina cement, it is expected for phases $C_{12}A_7$ and CA to be the main phases of the CAC. For this reason, CAC with low alumina content such as CAC51 does not present the CA_2 phase. High alumina cements, depending on their CaO/Al_2O_3 ratio, contain mainly CA and CA_2, or with increasing Al_2O_3 content, CA_2 and CA_6 [29,230,231].

2. Silica restricts the formation of C_2AH_8 in the hydration process and thus retards the effects of the conversion [180,232], because C_2AH_8 can occur mainly as a consequence of the hydration of CA_2 [19,160,161]. Therefore, in the hydration of low alumina cements, a small amount C_2AH_8 is formed, as per the previous explanation. On the other hand, stratlingite can be formed through the reactions of C_2AH_8 with S or AH_3, in accordance with $C_2AH_8 + AH_3 + S \rightarrow C_2ASH_8 + 3H$ or $C_2AH_8 + S \rightarrow C_2ASH_8$. This explains why the amount of C_2AH_8 drastically decreases in the formulations added with silica, (in Figures 22b, 22c this can be seen by the size and number of peaks). Part of the C_2AH_8 interacts with the silica to form C_2ASH_8 and, therefore, the silica favors the formation of C_2ASH_8. In this way, the silica restricts the formation of C_2AH_8 because it uses it to form stratlingite in the hydration process and thus retards the effects of the conversion, since the strantlingite is a stable phase from 65 °C and does not undergo conversion after its formation at least until 90 ± 5 °C [180].

3. The formulations without silica present the hydrated phases CAH_{10}, C_2AH_8 and gel AH_3, (see Figure 22a). The TGA and DTG tests (see Figure 31) show that when they undergo heating the hydrated phases are converted to crystalline phases C_3AH_6 and AH_3 according to the reaction scheme

   Formulations without silica present hydrated phases CAH_{10}, C_2AH_8 and gel AH_3, (see Figure 22a and 22b). TGA and DTG tests (see Figure 31), show that when subjected to heating the hydrated phases are converted to the phases C_3AH_6 and crystalline AH_3 according to the reaction scheme $3CAH_{10} \rightarrow C_3AH_6+2AH_3+18H$ [233] and $3C_2AH_8 \rightarrow 2C_3AH_6+AH_3+9H$ [234], as the temperature continues to rise phase C_3AH_6 is dehydrated according to $7C_3AH_6 \rightarrow C_{12}A_7H+9CH+32H$ [19,107,208,235] and AH_3 is dehydrated $AH_3 \rightarrow A+3H$ [19,107,208,235,236] later $CH \rightarrow C + H$ and $C_{12}A_7H$

dehydrates as $C_{12}A_7H \rightarrow C_{12}A_7+H$ approximately ~800 [235] then the mayenite is sintered with alumina and crystallized in CA and CA_2, according to $C_{12}A_7 +5A \rightarrow 12CA$ or $C_{12}A_7 +17A \rightarrow 12CA_2$ between 800 °C and 1000 °C [235]. This explains why the quantities of mineral $C_{12}A_7$ increases dramatically to 800 °C [237] and between 800 °C and 1000 °C decreases to higher alumina content, while the amount of minerals CA and CA_2 increase (see Figure 25).

4. The formulations with silica form the hydrated phases C_2ASH_8, CAH_{10}, C_2AH_8 (see Figure 22b and 22c). TGA and DTG tests (see Figure 31), show that as the temperature increases, stratlingite is dehydrated according to the reaction $C_2ASH_8 \rightarrow C_2AS+8H$, at temperatures between ~165 and 220 °C later C_2AS reacts with the alumina at 800 °C to generate mayenite and silica, $C_2AS+A \rightarrow C_{12}A_7+S$ between 800 °C and 1000 °C [53,168,169,238].

5. The formulations with silica do not produce gibbsite in the hydration process (see Figures 22b and 22c) and for CACP 51-10 wt% and 20 wt% there is little C_2AH_8, because they have low alumina content, (see numeral 2.), for this reason the formulations with silica only have the CAH_{10} phase to produce alumina during the heating while the phases without silica have the three hydrated phases, as channels, to produce alumina. For the formulations without silica, much more alumina is observed in the heating process up to 1000 °C than for the formulations with silica, which explains the following:

    a. The formulations with silica at 1000 °C have more unreacted $C_{12}A_7$ than those with silica since CACP 51-10 wt% has 9.9% $C_{12}A_7$, CACP 51-20 wt% 7.5% and CAC 51-0 wt% has 3.6% (see Figure 25). This is because in the heating process up to 1000 °C produces $C_{12}A_7$ and S and these two phases are not sintered at this temperature, so more energy is required to produce for example gehlenite C_2AS at 1200 °C and anorthite CAS_2 at 1400 °C [104,237,239].

    b. CACP51-0 wt% at 1000 °C (see Figure 25) is observed to contain CA and CA_2 in almost equal proportions of 50.5%, 45.9% respectively and little $C_{12}A_7$, at 3.6%. The small amount of $C_{12}A_7$ observed is due to the fact that there is more alumina to be sintered, since it does not contain silica.

    c. CACP51-10 and 20 wt% does not produce CA_2 because there is not enough alumina and the alumina that is produced reacts with $C_{12}A_7$ to produce CA due to the fact that less energy is required to produce it (see numeral 1), this also explains why higher amounts of CA are observed in these formulations (see Figure 24).

C_3AH_6 was not observed initially because the hydration process was performed at 20 °C, but in the heating process, it is evidenced from the TGA and DTG, that this phase was formed and then dehydrated in a temperature range of 306.57 - 351.67 °C for the different formulations investigated.

The crystallization process and the lack of energy to combine the anhydrous phases, explains why there is a loss of compressive strength between 200 °C and 1000 °C. At these temperatures there is not enough energy for the silica to react with the CA and CA_2, form gehlenite or anorthite, and start establishing the ceramic bonds. After at 1200 °C these phases are formed and ceramic bonds are established and a combination of them occurs.

It is important to investigate the behavior between 20 °C and 1000 °C as it helps to ascertain, with the best possible precision, the relationship between the amount of damage and the factors such as LS, CS, MS, PO, LD and AB. This helps to define the materials that can be mixed, the quantities, and methods to improve the material in with these factors in mind, as well as the temperatures to which the materials must be subjected to achieve particular phases and improve the mechanical properties.

6.5 CONCLUSIONS

1. The addition of silica to CACP restricts the formation of C_2AH_8 and Gibbsite (AH_3) and favors the formation of stratlingite ($C_2ASH_{8)}$ in the hydration process, implying that it avoids the conversion process and improves the mechanical strength.
2. Silica does not provide refractory properties for the heating process up to 1000 °C.
3. With the temperature increase between 800 and 1000 °C, the mayenite ($C_{12}A_7$) crystallizes in CA and CA_2, so these phases increase and the amount of mayenite decreases dramatically.
4. All formulations lose compression strength at 1000 °C but silica improves compression strength at 20 and 1000 °C.
5. The formulations with silica present a lower temperature dehydration of the AH_3 and similar hydration temperature for C_3AH_6.
6. The dehydration temperature of C_2ASH_8, C_2AH_8, AH_3, C_3AH_6 and CAH_{10} are close, in each formulation with 20 and 0 wt% correspondingly.
7. The formulations with addition of silica show a higher increase in the microstrains determined by the XRD tests, at 1000 °C

7. CHAPTER 7. CALCULATION OF ACTIVATION ENERGIES OF CALCIUM ALUMINATE CEMENT PASTES ADDED WITH MICROSILICA SUBJECTED TO HIGH TEMPERATURES

Submitted to publish

7.1 INTRODUCTION

When the hardened paste of CAC is heated up to 800 °C, the dehydration generates the conversion process $CAH_{10} \rightarrow C_2AH_8 \rightarrow C_3AH_6$ [30]. The dehydration process ends during heating up to 800 °C and $C_{12}A_7$ is formed which, after heating to a temperature of 1000 °C or higher, crystallizes in CA or CA_2 [22,30]. Antonovic et al [38] it complements by saying that in addition to $C_{12}A_7$, the mineral phases CA, CA_2 are also formed at 800 °C and is independent of the curing temperature and $C_{12}A_7$ predominates.

The activation energy is defined as the difference between the internal energy of the system in the transition state and that of the initial state. This is that minimum amount of energy required to initiate a chemical reaction or phase transformation. The use of non-isothermal methods for the calculation of the kinetic parameters of the reactions instead of the conventional isothermal methods is fully justified [81,85–88].

In this research different formulations of calcium aluminate cements pastes (CACP) with 71wt% of Al_2O_3 (CACP 71wt%), (wt% -percentage by weight) were made at 0.4 water to cement ratios (W/C) with additions of 0, 10 and 20wt% of silica (CACP 71-0, 10 and 20wt%, respectively). All samples were exposed to oxidative environment for 4 hours at 1000 ˚C, in a furnace under an air atmosphere. The chemical and mineralogical characterization was done using x-ray fluorescent (XRF) X-ray diffraction (XRD) (with Rietveld refinement) and Fourier-transform infrared spectroscopy (FTIR), their morphology is characterized with Scanning electron microscopy (SEM) tests and phase quantification is carried out by the Rietveld method.

The behavior of the constituent phases with the temperature was also studied through of thermal gravimetric analysis (TGA) and the corresponding derivative thermogravimetry (DTG). It is observed that: the $C_{12}A_7$ decrease dramatically between 800 °C and 1000 °C while the amount of minerals CA y CA_2 are increasing, Silica favors the formation of C_2ASH_8 , among other results. Activation energies were calculated using Friedman's method. The values of the activation energies obtained for the formulation of CACP 71- 0wt% for different phases, were in the range of 12.02 to 16.41 kJ/mol and for the formulation of CACP 71-20wt%, in the range of 7.7 to 16.23 kJ/mol.

Activation energies were calculated from the results of the TGA and DTG tests; and by using Friedman's differential method [240], whose mathematical expression is given by the equation (17):

$$\ln\frac{d\alpha}{dT} = \ln\left(\frac{A}{\beta}\right) + n\ln(1-\alpha) - \frac{Q}{RT} \quad (17)$$

When plotting $\ln\frac{d\alpha}{dT}$ vs $\frac{1}{T}$ a straight line is obtained, the slope of which can be found by numerical adjustment using the least squares method, which provides a value for the activation energy.

7.2 EXPERIMENTAL

7.2.1 SAMPLES MANUFACTURE

Silica from a natural Colombian source with 98% purity and an average grain size of 2 µm was used to prepare the specimens. The chemical composition of raw CAC 71wt% powder, obtained by X-ray fluorescence in an XRF Thermo spectrometer model OPTIM'X, is: Al_2O_3 (71.09), CaO (28.38), SiO_2 (0.238). Calcium aluminate cement pastes CACP were investigated. Three types of CACP 71wt% sample were made, with water to cement (W/C) ratios of 0.4, and with additions of silicon oxide of 0wt%, 10wt% and 20wt% as summarized in

Table 27. Formulations fabricated for cement paste sample with additions of silicon oxide, all cement pastes were fabricated and cured at 20°C and were kept closed to air contact for 48 hours (in order to avoid pre-carbonation), then released from molds and subjected to 48 hours of hydration covered with water, 5mm above its surface. Thereafter, samples were removed from water and let to air drying during 24 h. Sample dimensions were 19 mm in diameter and 22 mm in height.

Table 27. Formulations fabricated for cement paste sample with additions of silicon oxide

Formulations				
No	CEMENT	W/C	SiO_2 - wt%	T (°C)
1	CACP 71wt%	0.4	0	20
2			10	
3			20	

7.2.2 CHARACTERIZATION OF THE CAC PASTES

Tests for thermal gravimetric analysis (TGA) were performed in TGA Q500 V20.8 Build 34. InstrSerial 0500-1190 equipment. Temperature range was (25ºC to 1000ºC), at a rate of 10 °C/min. Additionally, the samples were heated to 1000°C, with a holding time of 4 hours in a Nabetherm GmbH 30-3000°C LT 9/12P330 furnace. Both heating and cooling were performed at a rate of 1.67°C/min, for analysis of the formation of phases according to

temperature and their kinetic behavior. The samples were characterized before and after heat treatment.

XRD characterization was done in a X'Pert PRO diffractometer with Cu K_ radiation of 1.5406 A°. Scanning was performed between 2θ of 5 to 70°, with a step size of 0.02°. For the XRD interpretation, the COD database (Crystallography Open Database) was used. Phase identification and Rietveld refinement were performed with the X'Pert High Score Plus/Panalytical software. For the elimination of the K-alpha 2 peak, the Rachinger model was used, with a background with a granularity of 20 and bending factor of 1. For the diffraction peak search, the second derivative minimization method was used. A JEOL JSM – 6490 scanning electron microscopes equipped with microwave energy dispersive X-ray was used to observe the variation of the microstructure of samples of all formulations. Fourier transform infrared spectroscopy (FTIR) measurements were conducted in a Shimadzu IR Tracer-100 with a scanning range between 400 and 4000 cm-1. The analysis was performed by ATR, with resolution 4 and 16 cycles.

7.3 ANALYSIS AND RESULTS

7.3.1 ANALYSIS BY XRD

PHASE IDENTIFICATION

The identification analysis of hydrated phases of CACP 71-0wt% silica at 20°C, confirmed the formation of CAH_{10}, C_2AH_8, AH_3, as shown in Figure 1c. This is consistent with what has been in the established in the literature [3,19,33,163,174,179]. The identification analysis of hydrated phases of CACP 71-10wt% and 20wt% at 20°C, confirmed the formation of CAH_{10}, C_2AH_8, C_2ASH_8 [170,174,180,181] (see Figure 37a and 36b). It can be seen that the influence of silica restricts the formation of AH_3, which implies that for these formulations the silica retards the conversion effect [19,164].

The conversion process of CAC, is due to the fact that the CAH_{10} and C_2AH_8 phases are metastable at ambient temperature and convert to the more stable phases C_3AH_6 and AH_3 [19,221]. This conversion is accompanied by the release of free water which results in a decrease in strength, caused by the increase in porosity and permeability and permeability [164]. The conversion process reaction scheme is equation (18) [3,51,165].

$$3C_2AH_8 \rightarrow 2C_3AH_6 + AH_3 + 9H$$
$$3CAH_{10} \rightarrow C_3AH_6 + 2AH_3 + 18H \quad (18)$$

Figure 37a, that corresponds to compositions with 10wt%, shown that the intensity of the peaks associated with C_2AH_8, drastically decreases with respect to the formulations with added silica, Figure 37a and 37b. This is because part of C_2AH_8 reacts with S or AH_3, in accordance with $C_2AH_8 + AH_3 + S \rightarrow C_2ASH_8 + 3H$ or $C_2AH_8 + S \rightarrow C_2ASH_8$ [17], to

form C_2ASH_8. Therefore, silica also restricts the formation of C_2AH_8 and thus retards the effects of the conversion. Silica favors the formation of C_2ASH_8.

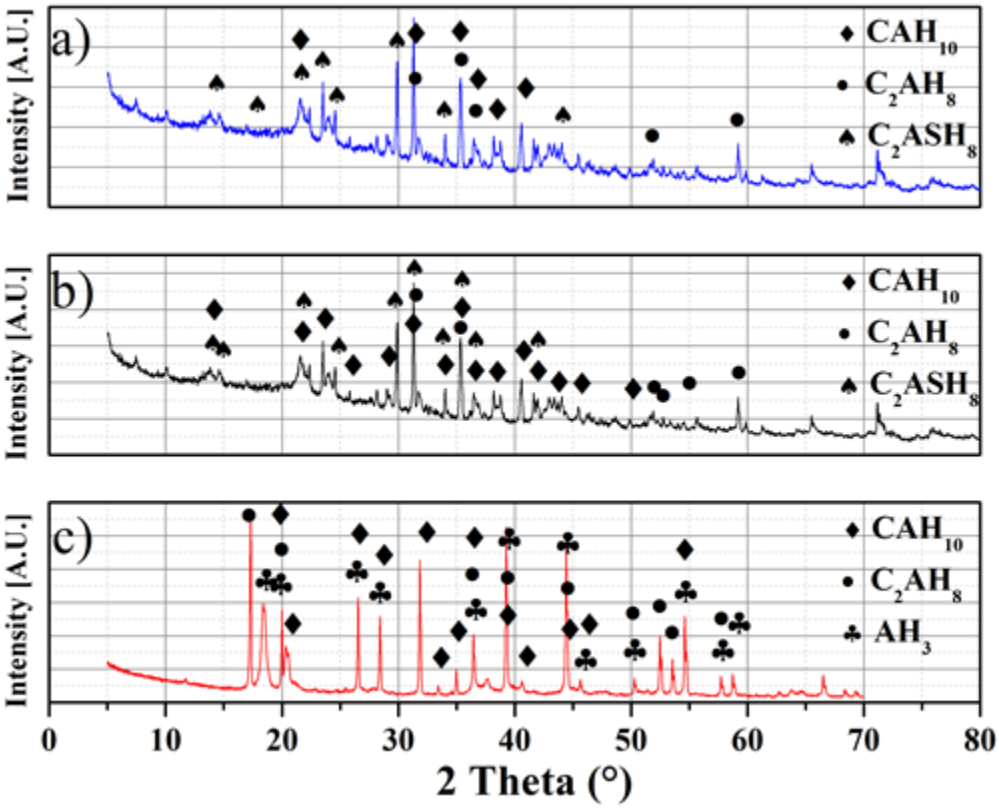

Figure 37. XRD, W/C=0.4, T= 20°C, CACP 71wt%: a) 10wt%, b) 0wt%, c) 20wt%

7.3.2 RIETVELD REFINEMENT ANALYSIS

The Bragg-intensity R(Bragg) value given by equation (19):

$$R_{Bragg} = \frac{\sum_{hkl}|F_{hkl}(obs) - F_{hkl}(calc)|}{\sum_{hkl} F_{hkl}(obs)} \quad (19)$$

Where $I_{hkl} = mF_{hkl}^2$, (m=multiplicity) and I_{hkl} is the intensity of each peak, can be used to monitor the improvement in the structural model [182]. It is accepted as good refinement when R(Bragg) < 10.

Table 28. Values of the database COD and R(Bragg)s, W/C=0.4, 1000°C. summarizes the values of the database COD (Crystallography Open Database) of the phases identified by XRD of samples submitted to 1000°C, W/C=0.4 and the estimated values of the R(Bragg)s, which shows that the phase identification was done with very good precision. Figure 38 shows the phases formed, established by XRD, with W/C = 0.4, at 1000°C for CACP 71-0wt%, 10wt%, and 20wt%.

Table 28. Values of the database COD and R(Bragg)s, W/C=0.4, 1000°C.

Formulation	Phase	Code - COD	R (Bragg)
CACP 71-0wt%	CA	96-200-2889	3.08
	CA_2	96-350-0015	3.61
	$C_{12}A_7$	96-901-1738	2.99
CACP 71-10wt%	CA	96-200-2889	3.44
	CA_2	96-350-0015	2.95
	$C_{12}A_7$	96-901-1738	2.88
	SiO_2	96-230-0371	4.02
CACP 71-20wt%	CA	96-200-2889	4.82
	CA_2	96-350-0015	4.25
	$C_{12}A_7$	96-901-1738	5.36
	SiO_2	96-230-0371	5.93

The Rietveld analysis was performed with the polynomial method. The order of the background, the unit cells, the atomic coordinates and width and shape of the peaks were refined in each phase. Table 29 shows all the values obtained from the Rietveld refinement parameters for all formulations subjected to 1000°C. The parameters of a good Rietveld refinement are defined as [50]: Rp: Residual of least-squares refinement. R_{wp}: weights residual. Rexp: evaluates the quality of the data. GOF: Goodness of fit; compare R_{wp} to Rexp. This is calculated from equation (20):

$$\mathrm{GOF} = \chi^2 = \left[\frac{R_{wp}}{Rexp}\right]^2 \quad (20)$$

It would be a perfect fit if GOF < 4 but the fit is acceptable for GOF < 10 and $R_p < 10$.

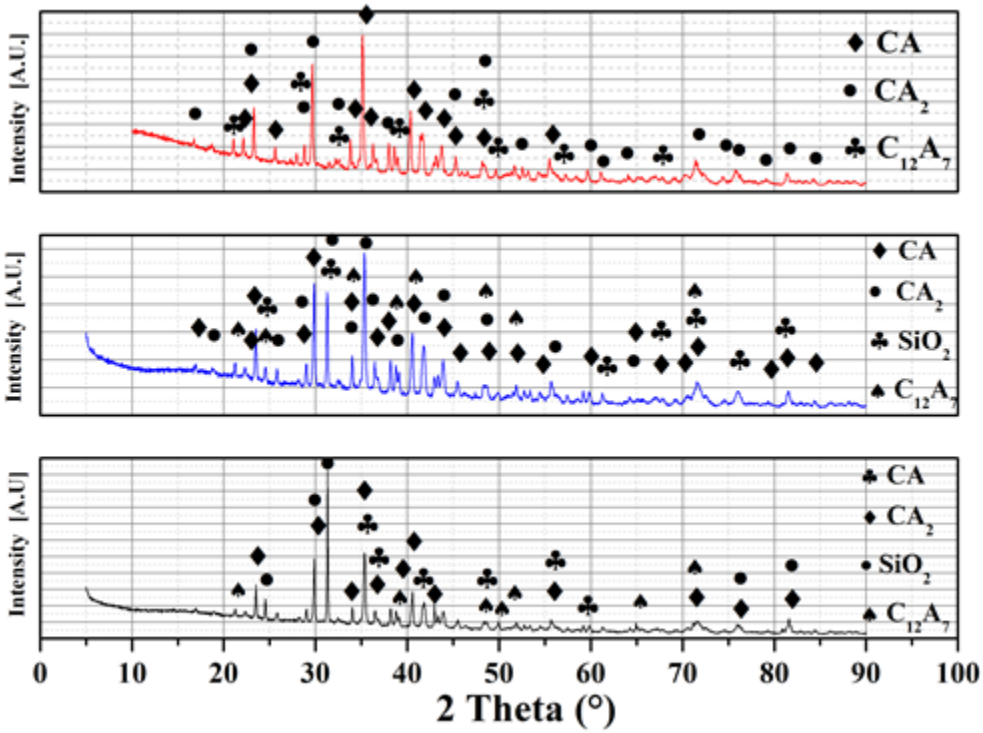

Figure 38. XRD, W/C=0.4, 1000°C, CACP 71: a) 0, b) 10, c) 20wt%.

Table 29. Rietveld refinement parameter – 1000°C: W/C=0.4

Formulations	Rexp	Rp	Rwp	GOF
CACP 71-0wt%	2.80	4.11	5.30	3.58
CACP 71-10wt%	3.23	6.32	7.21	4.98
CACP 71-20wt%	3.27	6.42	7.63	5.44

Figure 39 shows the quantification, obtained by Rietveld analysis, of CACP 71-0, 10 and 20wt%, W/C = 0.4, subjected to 1000°C. It can be seen from Figure 39 that the higher the silica content, the lower the CA and $C_{12}A_7$ content and the higher CA_2 content.

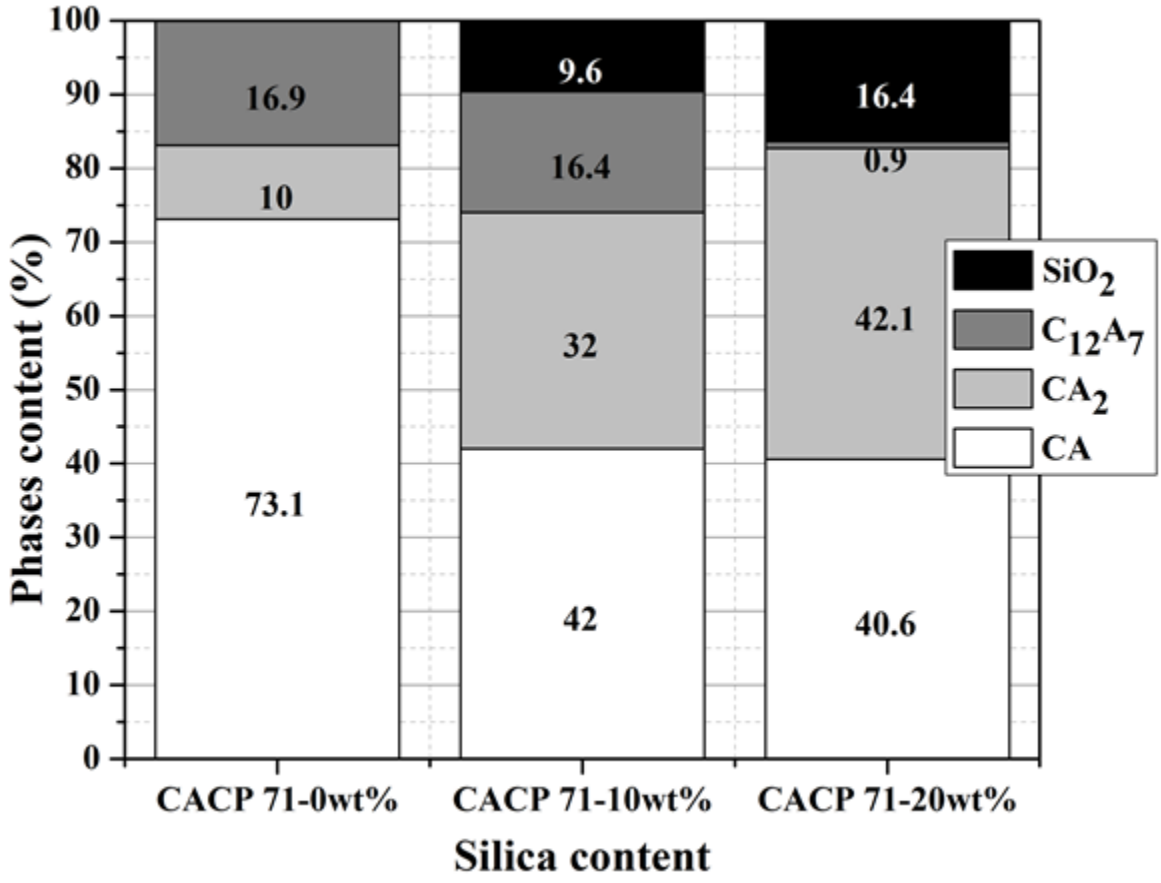

Figure 39. Quantification of phases by Rietveld refinement's, W/C=0.4, CACP 51-71, with 0wt%, 10wt% and 20wt% silica content, 1000 °C.

These results suggest that silica, in high alumina cements, favors the formation of CA_2 at 1000°C, which implies that the silica improves the mechanical resistance. The $C_{12}A_7$ phase impairs mechanical resistance, so the formation of this phase in large percentages should be avoided in the manufacture of cement. It can also be seen from Figure 39 that silica restricts the formation of $C_{12}A_7$ at 1000°C, which further demonstrates that silica improves mechanical strength.

7.3.3 FTIR ANALYSIS

Figure 40a and 40b, show the results of FTIR tests for CACP 71-10wt% and 20wt% at 20°C, in the range of 400-1200 wavenumbers (cm^{-1}). It can be seen that stratlingite is formed at very low wavenumbers and transmittance. The value of the wavenumbers for the transmittance peaks for Figure 40 are summarized in Table 30.

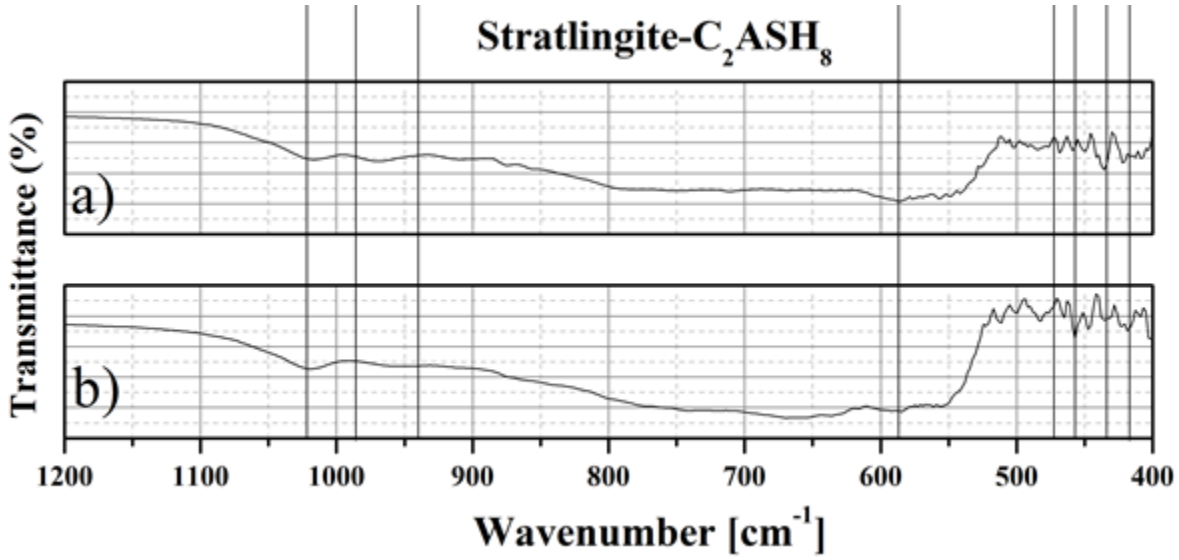

Figure 40. FTIR, 20°C, W/C=0.4, range 400-1200 [cm^{-1}]:
a) CACP 71-10wt%, b) CACP 71-20wt%.

Table 30. FTIR – wavenumbers values for Stratlingite

Wavenumber [cm^{-1}]	Assignment	Reference
1019.17, 967.77, 906.50 579.79, 482.37, 467.17, 437.85, 418.46 [71-10-20] [71-20-20]	Si–O–Al-Stratlingite	This work

Figure 41a and 41b, shows the results of FTIR tests for CACP 71-10wt% and 20wt% at 20°C in the range of 1000-4000 wavenumber (cm^{-1}). The formation of the same phases detected by XRD is verified. The values of the wavenumbers for the transmittance peaks are summarized in Table 31.

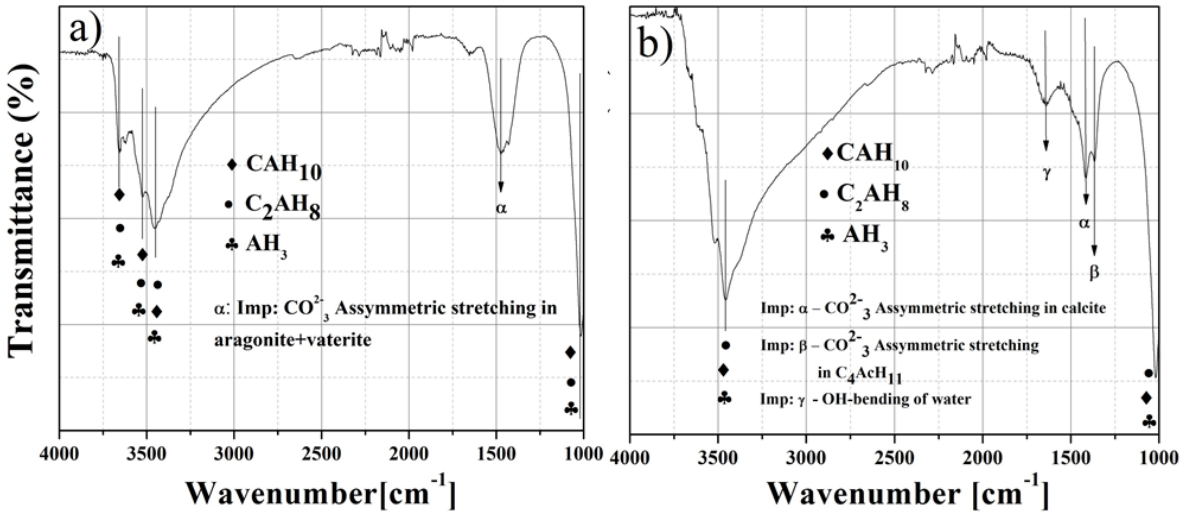

Figure 41. FTIR results of CACP 71:
in the range between 1000 and 4000 cm^{-1} without heat treatment with: a) 10wt% silica and b) 20wt% silica.

In Figure 41a, α refers to an impurity of CO_3^{2-} Asymmetric stretching in aragonite + vaterite. In Figure 41b, α refers to an impurity of CO_3^{2-} Asymmetric stretching in calcite, β refers to CO_3^{2-} Asymmetric stretching in C_4AcH_{11} and γ refers to OH – bending of water.

Table 31. Assignments of FTIR Transmittance Bands:
in CACP 71-10wt% and 20wt%, 20°C, W/C= 0.4.

Wavenumber [cm^{-1}]	Assignment	Reference
3659.47 [71– 10 – 20]	O-H stretch in hydrogarnet	This work
3522.59 [71– 10 – 20]	O-H stretch in gibbsite	This work
3457.21 [71– 10– 20] 3451.08 [71– 20– 20]	O-H stretch in gibbsite	This work
1646.31[71 – 20 – 20]	O-H bending water	This work
1474 [71– 10 – 20]	CO^{2-}_3 Asymmetric stretching in aragonite+vaterite	This work
1414.76 [71 – 20 – 20]	CO^{2-}_3 Asymmetric stretching in calcite	This work
1367.08 [71 – 20 – 20]	CO^{2-}_3 Asymmetric stretching in C_4AcH_{11}	This work

Figure 42 show FTIR curves, 1000°C, W/C = 0.4 of CACP 71-10wt% and 20wt%. The same phases detected by XRD are observed. The values of the observed adsorption peaks are summarized in Table 32.

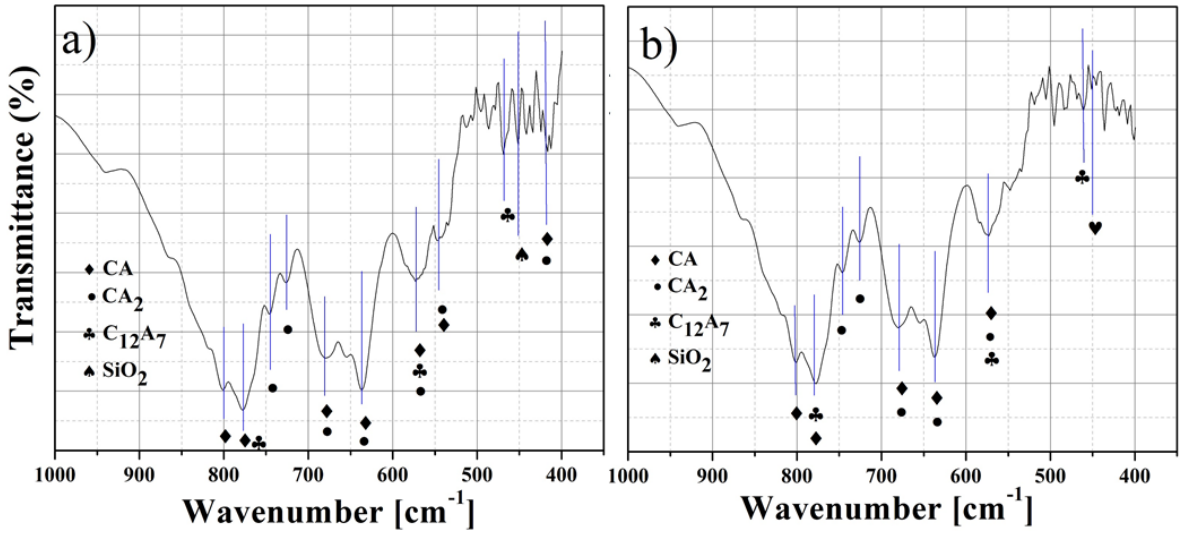

Figure 42. FTIR, 1000°C: W/C=0.4. CACP 71: a) 10wt%, b) 20wt%.

Table 32. Assignments of FTIR transmittance Bands in CACP 71-10 and 20wt%, 1000 °C.

Wavenumber [cm^{-1}]	Assignment	Reference
801.38 [71– 20 – 1000] 800.07 [71– 10 – 1000]	AlO_4 vibration in CA	This work
776.89 [71– 10– 1000] 775.38 [71– 20– 1000]	AlO_4 vibration in CA AlO_4 vibration in $C_{12}A_7$	This work
744.72 [71– 10– 1000] 746.05 [71– 20– 1000]	AlO_4 vibration in CA_2	This work
725.36 [71– 10– 1000] 725.54 [71– 20– 1000]	AlO_4 vibration in CA	This work
681.71 [71– 10– 1000] 679.21 [71– 20– 1000]	AlO_4 vibration in CA_2 AlO_4 vibration in CA	This work
636.71 [71– 10– 1000] [71– 20– 1000]	AlO_4 vibration in CA_2 AlO_4 vibration in CA	This work
573.70 [71 – 20– 1000] 572.37 [71– 10– 1000]	AlO_4 vibration in CA_2 AlO_4 vibration in CA AlO_4 vibration in $C_{12}A_7$	This work
451.52 [71– 10– 1000] 450.19 [71– 20– 1000]	SiO_4 bending vibration of quartz	This work
418.02 [71– 10– 1000]	AlO_4 vibration in CA_2 AlO_4 vibration in CA	This work

7.3.4 TGA – DTG ANALYSIS

Figure 43a shows the TGA curve for CACP 71-0wt%. There are four characteristic temperatures: 129.67 and 236.00 °C, which can be associated with the dehydration of CAH_8 and C_2AH_8, respectively; and 302.84 °C and 338.74°C, which can be associated with the dehydration of AH_3 and C_3AH_6, respectively. In the process of dehydration between 236.00 °C and 338.74 °C, a mass loss of 16.30% is observed, equivalent to approximately 6.45 mg.

Figure 43b shows the DTG curve associated with the TGA curve for CACP 71-0wt%, which exhibits the peaks at the indicated the dehydration temperatures for AH_3 and C_3AH_6 [241,242].

Figure 43c shows TGA curve for CACP 71-20wt%. Here, four characteristic temperatures are observed, which can be associated, 169.33 °C to the dehydration of C_3AH_{10} [37]; 245.24 °C which can be associated to that of C_2ASH_8, 297.89 °C, which can be associated to that of

AH_3; and 351.67 °C, which can be associated to that to that of C_3AH_6. In the process of dehydration between 169.33°C and 351.67 °C, a mass loss of 20.12% is observed, equivalent to approximately 3.825 mg.

Figure 43d shows the DTG curve associated with the TGA curve for CAC 71-20wt%, and confirms the dehydration temperatures for AH_3 and C_3AH_6. Table 33 summarizes the decomposition temperatures of CACP hydration products in °C found in this work.

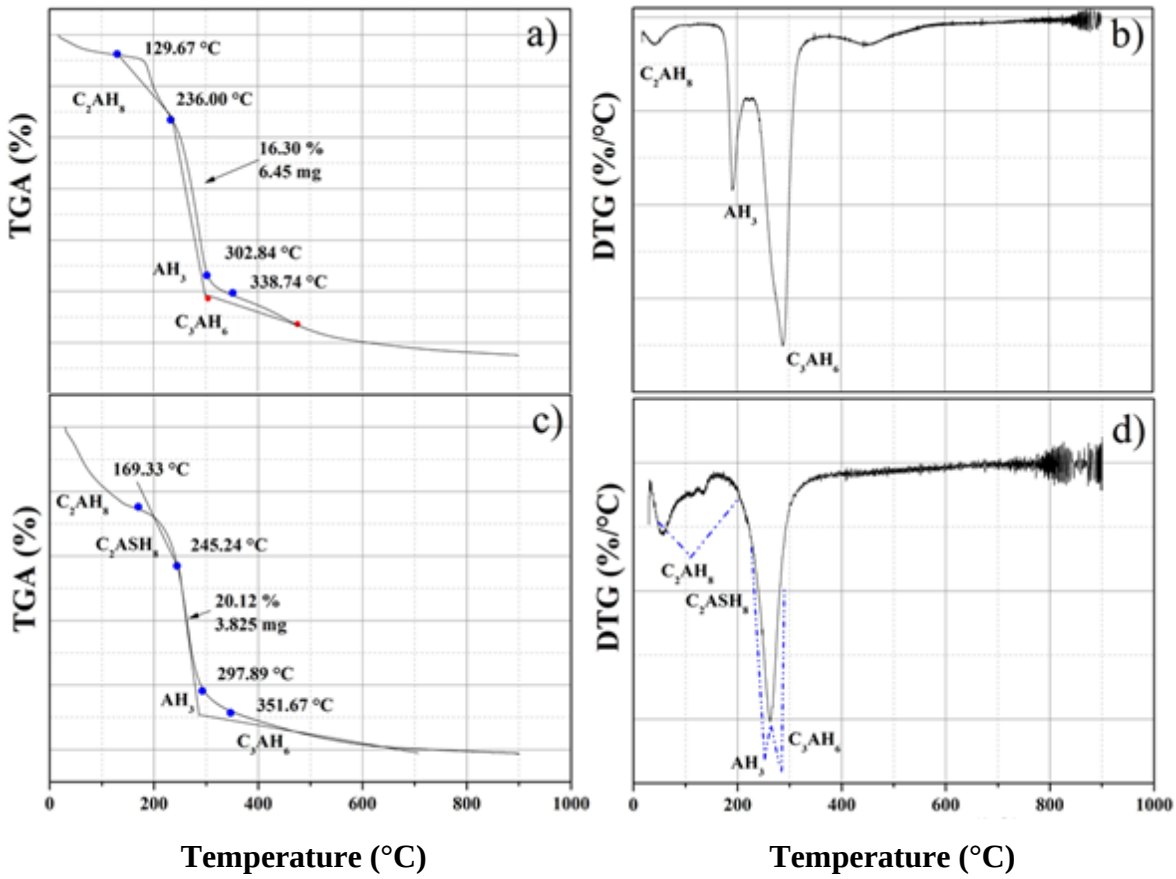

Figure 43. Curves TGA and DTG of CACP 71:

a) TGA-0wt%, b) DTG 0wt% c) TGA – 20wt%, d) DTG-20wt%

As the dehydration of AH_3 and C_3AH_6 occurs at very similar temperatures, and the thermal energy for the dehydration of AH_3 is much greater than that for the dehydration of C_3AH_6, these dehydration peaks overlap in a slow sweep, for example a rate of 10 °C/min [53], which was the one used in this work. Therefore, the total thermal energy for the dehydration of AH_3 and C_3AH_6 phases are observed together in the same peak as observed in Figure 43d.

The AH_3 phase, can be formed in small quantities in the hydration process at 20 °C in the form of a quasi-crystalline gel. As it can be seen in Figure 43c. The C_3AH_6 phase is only

formed by conversion or hydration at temperatures higher than 35°C, so it does not appear initially to 20°C [176,243].

The AH_3 and C_3AH_6 phases produced by conversion are crystalline, if XRD and FTIR are made with samples heated to 35 °C or higher up to approximately 300 ° C, they would appear, but we only did them at 20 and 1000 °C, but Figure 43 shows its formation and subsequent dehydration, in the heating process.

Table 33. Decomposition temperatures of CACP hydration products in °C according to this work.

Reference	Method	CAH_{10}	C_2AH_8	C_2ASH_8	C_3AH_6	AH_3-gel	AH_3	Al $(OH)_3$
This work – CACP 71-0wt%	TGA-DTG	129.67	236.00	–	338.74	–	302.84	–
This work – CACP 71-20wt%	TGA-DTG	–	–	245.24	351.67	–	297.89	–

Table 34 and Table 35 show the temperature ranges of the phase dehydration, the activation energy and the correlation factor for CACP 71-0wt% and CACP 71-20wt%. The activation energies were calculated based on the data obtained by the TGA tests (see Figure 43) and using Friedman's model, equation (17).

Table 34. Activation energies at different stages – CACP 71-0wt%

Dehydration	Temperature range [°C]	R^2	Activation energy [kJ/mol]
C_2AH_{10} to AH_3	236-302	0.9811	12.02
C_2AH_{10} to C_3AH_6	236-338	0.9842	16.41
C_3AH_6 to CA	336-700	0.9870	13.71

Table 35. Activation energies at different stages – CACP 71-20wt%

Dehydration	Temperature range [°C]	R^2	Activation energy [kJ/mol
C_3AH_{10} to AH_3	169.33 - 297.89	0.9831	9.79
C_3AH_{10} to C_3AH_6	169.33 - 351.67	0.9843	7.70
C_2ASH_6 to CA + S	336 - 700	0.9825	16.23

7.4 DISCUSSION

It can be seen from Table 34, that the activation energies decrease at a higher temperature starting from the average range of 16.41 kJ/mol to 13.71 kJ/mol in the dehydration of C_2AH_{10} and C_3AH_6 respectively, but from Table 35 the opposite is observed, there is an increase in

activation energy 7.70 kJ/mol to 16.23 kJ / mol in the dehydration of C_3AH_{10} and C_2ASH_6 respectively.

The growth of the activation energy could be due to the collapse of the calcium aluminate hydrate network after dehydration, and the increase in the cationic field of the aluminum cation with the dehydration of the gel. This suggests that silicon bonding leads to more energy being required for the dehydration process. The decrease in activation energy may be due to the disintegration of the compact structure, which facilitates the release of calcium water molecules and aluminate hydrates.

The crystallization process and lack of energy to combine the anhydrous phases. This explains why there is a loss of compression strength at high temperatures in these cements. At these temperatures (1000 °C), there is not enough energy for the silica to react with the CA and CA_2 and form gehlenite or anorthite, thereby starting to establish the ceramic bonds. After 1200°C, these phases are formed, ceramic bonds are established, and a combination of the phases occurs.

In this work it was found that the hydrated CAC forms stratlingite when reacting with the silica, according to the reaction scheme (3) and this improves the mechanical properties over a wide range of temperatures [174,180,197,232,244–248].

7.5 CONCLUSIONS

- Silica restricts the formation of C_2AH_8 while favoring the formation of C_2ASH_8 in the hydration process.
- The formulations with silica do not produce gibbsite (AH_3) in the hydration process.
- The dehydration temperature of C_2ASH_8, C_2AH_8, AH_3, C_3AH_6 and CAH_{10} are close, in each formulation with 10wt% and 20wt% correspondingly.
- The values of the activation energies obtained for the formulation of CACP 71-0wt% for different phases, were in the range of 12.02 to 16.41 kJ/mol and for the formulation of CACP 71-20wt%, in the range of 7.7 to 16.23 kJ/mol.
- Silica, in high alumina cements, favors the formation of CA_2 at 1000°C, which implies that the silica improves the mechanical resistance.
- The $C_{12}A_7$ phase discourages mechanical resistance, so it is a phase that should be avoided if it is formed in large percentages, in the manufacture of cement, which implies by another criterion that silica improves mechanical strength.

8. CHAPTER 8: CALCIUM ALUMINATE CEMENTS WITH SILICA CONTENTS UNDER HIGH TEMPERATURE COMPRESSION TESTS

Submitted to publish

8.1 INTRODUCTION

Some of the main properties attributed to CAC are high strength to impact and abrasion, good acid resistance, high temperature stability, and high early strength cement [1]. CAC is one the main binders used by industry in the monolithic refractories [1,4,23,65,245], while other applications include industrial floors for extreme acidic conditions, and protective coatings and chemical products for the construction industry [23]. The hydrated phases that are formed with CAC depend on the temperature [19,245]. The main phase of hydration at temperatures $\leq 20°C$ is the CAH_{10} [22,31]. For temperatures $\geq 20°C$, the majority phases are C_2AH_8 ($Ca_2Al_2O_{13}H_{16}$ - Dicalcium aluminate octahydrate) and AH_3 ($Al(OH)_3$ - Gibbsite) [22]. The initial high resistance of the CAC is attributed to the formation of hexagonal hydrates, CAH_{10} ($CaAl_2O_{14}H_{20}$ - Monocalcium aluminate decahydrate) and C_2AH_8, but these phases are metastable and are converted to phases C_3AH_6 ($Ca_3[Al(OH)_6]_2$ - Katoite), which are more stable [22,164,167], which certainly limits the applications of these materials.

The hydration reactions for CACP added with silica, follows the equations (21), where the stratlingite could crystallize in a stable phase in the temperature range $T{\sim}20°C - 90°C$ [17].

$$\begin{gathered} CAH_{10} + S \rightarrow C_2ASH_8 + AH_3 + 9H \\ C_2AH_8 + AH_3 + S \rightarrow C_2ASH_8 + 3H \\ C_2AH_8 + S \rightarrow C_2ASH_8 \end{gathered} \tag{21}$$

In order to determine the CACP behavior under high temperature, the use of non-isothermal methods for the calculation of the kinetic parameters from the reactions instead the use of conventional isothermal methods is required [75,81,85–88], where the activation energy can be calculated with and without considering the stresses. For the activation energies in the absence of stress, TGA tests and Friedman's differential method has been used before [240], mainly due to its simplicity and precision, whose mathematical expression is given by the equation (17).

Three creep extrapolation techniques have been extensively explored for the creep design:

a. The theoretical approach, which is addressed from the constitutive equations, is derived from an analysis of the continuum mechanics.
b. The practical or parametric approach; is developed from numerical methods with the mathematical fit of models and experimental curves. Larson-Miller [249], Sherby-Dorn [250] and Manson-Haferd [251].

c. Theta Projection Model (TPM) [249,252,253] is a procedure for the interpolation and extrapolation of creep properties, some of which may have been obtained from accelerated tests. TPM has been successfully applied to ceramic materials [254–256], however, has not been applied to CACP [254,256,257].

Experimentally, it has been established for crystalline materials that creep at the micro scale is governed by three types of mechanisms or combinations of them: intragranular dislocation, diffusive creep (diffusion of vacancies), and grain-boundary diffusion [258–262]. A particular case of creep at low stresses and high temperatures, which is governed by self-diffusion energy and is linear in the stress, is known as Nabarro-Herring creep [263,264]. As the temperature goes down near 0.4Tm, the atoms (vacancies) are more opposed to move, being forced to use the grain boundaries, which is known as Coble's creep [265]. The standard creep modeling of the second stage of creep at high temperature in crystalline materials, has been described with equation (22) [266,267]. Where $\dot{\varepsilon}$ is the steady state strain rate, A is a dimensionless constant, and D is the diffusion coefficient, G is the shear modulus, b is the Burgers vector, k is the constant of Boltzmann ($\approx 1.38 * 10^{-23}$ J/°K), T is the absolute temperature, d is the grain size, p is the inverse grain size exponent, σ is the stress to which it is subjected the material, and n is the exponent of stress.

$$\dot{\varepsilon} = \frac{ADGb}{kT}\left(\frac{b}{d}\right)^{p}\left(\frac{\sigma}{G}\right)^{n} \tag{22}$$

$$D = D_0 exp\left(-{}^{Q}/_{RT}\right) \tag{23}$$

In equation (23), D_0 is the frequency factor and R is the gas. The mechanisms of diffusion of creep in the boundary may be subdivided into three distinct categories [268–270]: Lifshitz sliding, with an elongation of the grain in the direction of the stress; Rachinger sliding, when there is no elongation in the grains; and Interface reaction control, when the boundaries are not perfect sinks and sources for vacancies. Results of several diffusive creep works, the subtype of the creep and the values of n and p associated with those mechanisms, have been published: Lifshitz Sliding: n=1, p=1[271,272]; n=2, p=1[273–277]; n=2, p=2[278]; n=2.4, p=1.4[279]; n=5,p=1[280]. Rachinger Sliding: n=1, p=2 [281]; n=2, p=1[274,282]; n=2, p=2 [266,277,283,284].

Creep parameters can be calculated from a numerical fit by non-linear regression methods, TPM and experimental curves. TPM proposed by Evans et al. [252,257], is mathematically represented by equation (24),

$$\epsilon = \theta_1\left(1 - e^{-\theta_2 t}\right) + \theta_3\left(e^{\theta_4 t} - 1\right) \tag{24}$$

The parameters θ_1 and θ_2 characterize the state of primary strain, where θ_1 determines the strain at the end of the primary state and θ_2 governs the curvature of the process, θ_3 is the strain of the tertiary state (that is, the total strain reached in the creep to the failure of the material, regardless of the one reached in the primary state) and θ_4 represents the curvature of the tertiary strain.

Equation (24) shows the strain at each instant of the material's life. On the other hand, the limit moment between the primary and tertiary states, characterized by the minimum strain rate, is obtained by deriving the equation (24) twice and equaling it to zero, obtaining the minimum time of creep ($\mathrm{t_m}$) or life time as is show in equation

(25), with a minimum creep rate given by equation (26):

$$\mathrm{t_m} = \frac{1}{\theta_2 + \theta_4} \ln\left(\frac{\theta_1 \theta_2^2}{\theta_3 \theta_4^2}\right) \tag{25}$$

$$\dot{\epsilon}_\mathrm{m} = \theta_1 \theta_2 e^{-\theta_2 \mathrm{t_m}} + \theta_3 \theta_4 e^{\theta_4 \mathrm{t_m}} \tag{26}$$

Thus, with the values of these four θ parameters, the strain (ϵ), life time (t_m), and the minimum creep rate ($\dot{\epsilon}_m$), can be calculated as function of time. The data provided by equation (25) and (26) are used to estimate the values of n and E_a (equations (27) and (28)) for any stress and temperature [285], with n is the exponent of stress. Δ denotes a finite and small increase.

$$n = \frac{\partial \ln \dot{\epsilon}}{\partial \ln \sigma} \sim \frac{\Delta \ln \dot{\epsilon}}{\Delta \ln \sigma} \tag{27}$$

$$Q = -R \frac{\partial ln\, \dot{\epsilon}}{\partial (T^{-1})} \sim -R \frac{\Delta ln\, \dot{\epsilon}}{\Delta (T^{-1})} \tag{28}$$

In the theory of internal variable, the internal variables associated with general hardening (H), recovery (R) and damage by creep (W) are all scalar quantities during the whole lifetime of creep, were developed by Evans [286] in terms of theta parameters of the TPM and used by Baldan et al [287]. The constitutive equations are [287]:

$$\dot{\epsilon} = \dot{\epsilon}^0 \left(1 + \dot{H} + \dot{R} + \dot{W}\right) \tag{29}$$

and

$$\dot{H} = -\widehat{H}\dot{\epsilon};\ \dot{R} = \widehat{R};\ \dot{W} = \widehat{W}\dot{\epsilon} \tag{30}$$

where

$$\dot{\epsilon}^0 = \theta_1 \theta_2 + \theta_3 \theta_4 \tag{31}$$

$$\widehat{H} = \frac{\theta_2}{\theta_1\theta_2 + \theta_3\theta_4} \quad (32)$$

$$\widehat{R} = \frac{\theta_2\theta_3\theta_4}{\theta_1\theta_2 + \theta_3\theta_4} \quad (33)$$

$$\widehat{W} = \frac{1}{\theta_3} \quad (34)$$

The addition of silica to the CACP decreases the porosity, increases the mechanical resistance [197,245] and plays an important role in modern castable technology, although it is potentially negative for hot resistance and greatly improves the placement characteristics [246].

It is important to know how much damage is due to creep or other mechanisms to be able to use the materials designed in the right conditions and to know the effect of silica on the amount of damage. For this reason, in this work, a creep analysis of pure CACP and CACP 51-10wt% and 20wt% and CACP 71-10wt% and 20wt% is made by estimating parameters from the TPM and to understand the mechanisms. The values of the Theta Projection Model parameters were estimated using non-linear regression fit methods.

Different formulations of CACP with 51wt% and 71wt% added with silica have been exposed to high-temperature oxidation environments during 16 hours at T=800°C, in a furnace built for creep tests, subjected to the constant stress of 0.3MPa. CACP was mixed with 10% and 20 wt% of silica and had a Water to Cement ratio (W/C) of 0.40. Both, the raw cement powders and their corresponding hydrated samples, were characterized using laser granulometry, X-ray Fluorescence, X-ray Diffraction, and Scanning Electron Microscopy. The parameters of the TPM are calculated by fitting the experimental curve upon the optimization of non-linear regression techniques, implemented in the MATLAB software: The activation energy (Q), minimum time of creep (t_m), minimum creep rate $(\dot{\epsilon}_m)$, inverse grain size exponent (p) and the exponent of the stress (n). The creep micro-mechanisms were established as well. In addition, the internal variables associated with general hardening (H), recovery (R) and damage by creep (W) were calculated to find relationships between their rheological and microstructural behavior.

The behavior of the constituent phases with the temperature was also studied through Thermal Gravimetric Analysis for CACP 71wt% and CACP 71-20wt%. A value for CACP 71wt% of the activation energy exclusively of creep, of 2.98 kJ/mol and for CACP 71-20wt% of 7.04 kJ/mol was estimated.

8.2 MATERIAL AND METHODS

CACP 51-71-0, 10 and 20wt%, were investigated in this work. Six types of samples were fabricated. W/C was kept to 0.4, as shown in Table 36. Formulations fabricated for cement paste samples with additions of silicon oxide The chemical composition of these powders was obtained in X-ray Fluorescence (XRF) Thermo spectrometer Model: OPTIM'X. Sample dimensions were 19 mm in diameter and 22 mm in height. All samples were fabricated at 20°C and were kept closed to air contact for 48h (in order to avoid pre-carbonation).

Thereafter, samples were removed from water and let to air drying during 24h and subjected to 48 hours of hydration, covered with water 10mm above its surface.

Table 36. Formulations fabricated for cement paste samples with additions of silicon oxide.

Sample	W/C	SiO_2 (wt%)	T (°C)
CACP 51wt%	0.4	0	20
CACP 51wt%	0.4	10	20
CACP 51wt%	0.4	20	20
CACP 71wt%	0.4	0	20
CACP 71wt%	0.4	10	20
CACP 71wt%	0.4	20	20

X-ray Diffraction (XRD) characterization was done in a X'Pert PRO diffractometer with Cu Kα radiation of 1.5406 A°. The scanning was performed between 2θ of 5 to 70°, with a step size of 0.02°. A JEOL JSM – 6490 scanning electron microscope with energy-dispersive x-ray spectroscopy was used to analyze the samples and the damage, when the samples were subjected to creep tests. Secondary electrons were used for a better definition of the surface texture. A more complete characterization of the powders and CACP used in this work were reported in [31,191].

Thermal Gravimetric Analysis (TGA) tests were performed in equipment: TGA Q500 V20.8 Build 34. Purge gas conditions Gas Purity Composition Moisture Nitrogen 99.995% N_2. Oxygen 99.980% O_2, at a rate of 10 °C/min.

Samples were subjected to high temperature compression tests in a self-made machine shown in the Figure 44, at a temperature of 800°C during 16 hours and with a constant stress of 0.3MPa. The heating temperature ramp was 3.4°C/min. This equipment has an external sensor that measures the strains at a micrometric scale with the following functions and characteristics:

a) Zero setting at any position, b) ON/OFF button, c) Metric/Inch system interchange at any position, d) With data output interface. Characteristics: e) Power: One 1.5v SR44 battery, f) Operating temperature: 0°C ~ 40°C, g) Storage temperature: -20°C ~ 70°C, h) Relative humidity: ≤ 80%.

In Figure 44: 1. Alumina support with high melting point. 2. Sample submitted to creep tests. 3. Resistance generating high temperature. 4. Alumina rod. 5. Load slip train. 6. strain sensor. 7. Iron rod - sliding channel. 8. Weight that generates the stress of the test. 9. Support for sensor displacement needle. 10. Metallic load support of high temperature compression tests. 11. Counterweight for the sliding platform.

The activation energy was calculated in the absence of stress (TGA Test) and by high temperature compression tests using TPM. Activation energies in the absence of stress were calculated from the results of the TGA tests, and using Friedman's differential method given by the equation (17). When plotting $\ln \frac{d\alpha}{dT}$ vs $\frac{1}{T}$ a straight line is obtained whose slope can be found by numerical adjustment, using linear regression method, which provides a value of the activation energy.

The values of the parameters θ_1, θ_2, θ_3 and θ_4 of TPM (see equation (24)) were estimated by numerical fit, using nonlinear regression methods, with creep experimental curve. The values for the different formulations of the lifetime (t_m) were estimated using the equation (25), the minimum creep rate ($\dot{\epsilon}_m$) using the equation (26), stress exponent - power law n using the equation (27) and activation energy creep (Q) using the equation (28). The rate values of the internal variables associated with the general hardening (H), the recovery rate (R) and the damage by creep (W). $\dot{H}$, $\dot{R}$, $\dot{W}$ were calculated with the theory of Evans [286].

To estimate the amount of damage exclusively by creep, this strain has been estimated integrating equation (28), using the minimum time value (found with the equation (25)) and the value of the exclusive activation energy for creep found by TPM.

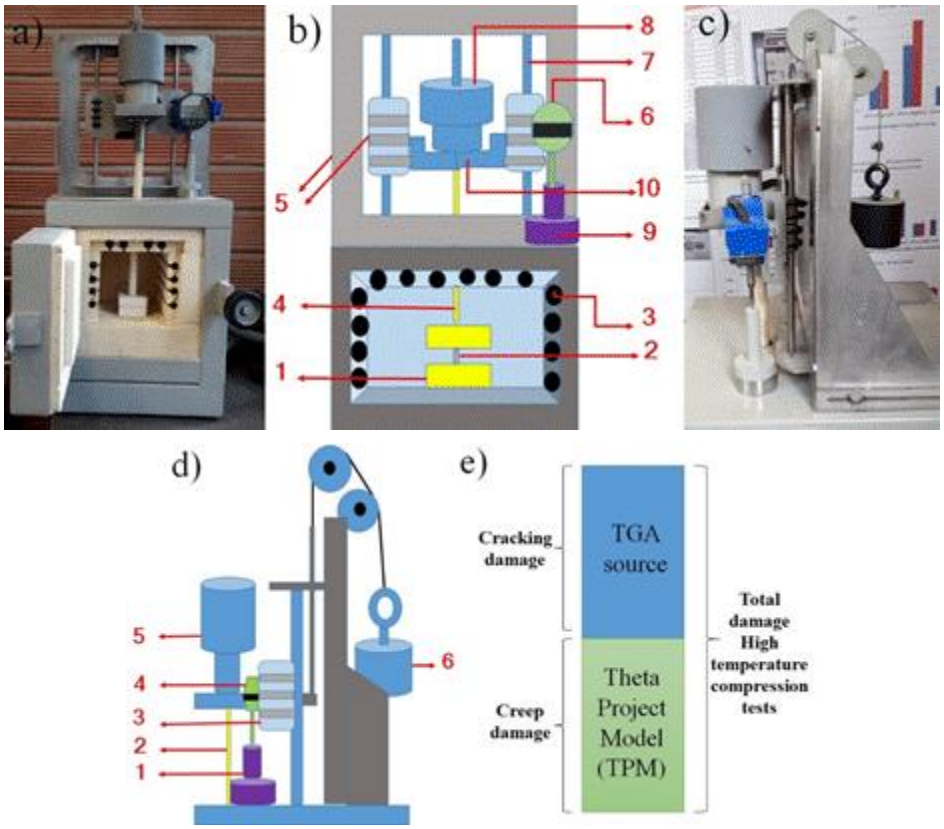

Figure 44. Furnace characteristics: a) Furnace for high temperature compression tests, b) diagram that describes details of the furnace, c) Data loading and acquisition system, d) Schematic representation of the loading and data acquisition system, e) Damage mechanisms by high temperature compression tests.

8.3 RESULTS

XRF results for chemical composition of CAC powder with 51-71wt% of alumina (CAC 51wt%-CAC 71wt%, respectively) are shown in the Table 37.

Table 37. Chemical composition of raw CAC powders.

Sample	Chemical Composition (wt%)								
	Al_2O_3	CaO	SiO_2	TiO_2	Fe_2O_3	K_2O	P_2O_5	ZrO_2	MoO_3
CAC 51wt%	52.12	37.82	5.25	1.87	1.81	0.128	0.108	0.086	0.052
CAC 71wt%	71.09	28.38	0.238	-	-	-	-	-	-

The Figure 44. *Powder properties: a) Particle size distribution curves CAC Powders. b) XRD for raw powder from silica*a) shows the particle size probability curves of the CAC powders from data taken with the laser granulometry technique. The normal distribution curve establishes an average diameter of 4 µm for the CAC powder 71 wt% and CAC powder 51wt% of alumina, that is, both cements show a similar granulometry. The powder from silica was analyzed with XRD and it is presented in Figure 44.b). Results proved that the sand used is made of high purity silica, very fine in size, with an average particle diameter of 0.16 µm.

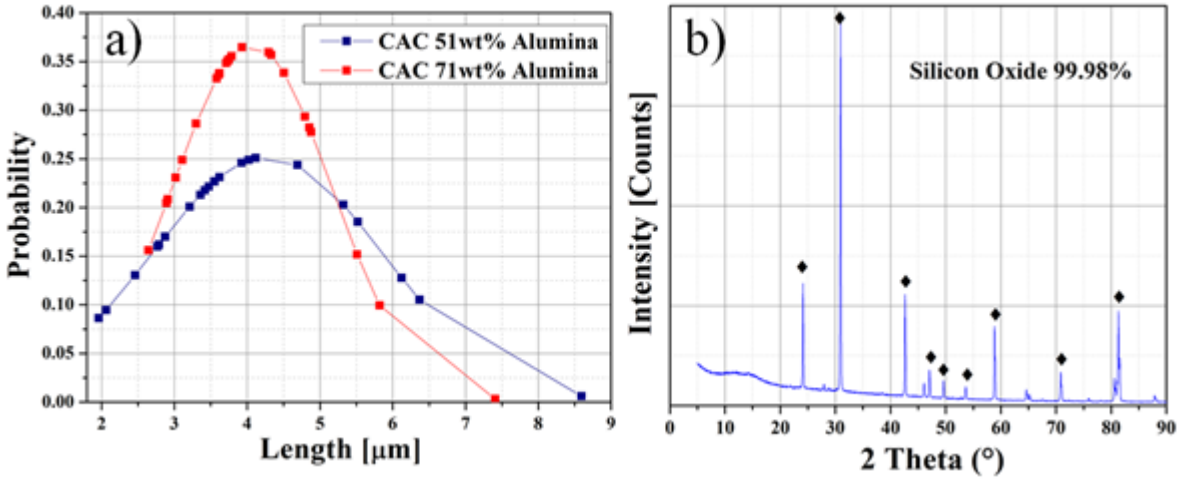

Figure 44. Powder properties: a) Particle size distribution curves CAC Powders. b) XRD for raw powder from silica.

Other results regarding the raw materials characterization and regarding the hydrated phases without additives were published before [31].

Other results regarding the raw materials characterization and the hydrated phases without additives were published before [31]. Figure 45 shows XRD data for pure CACP and CACP added with silica for W/C=0.4 at 20 °C. It can be seen that the main phases are CAH_{10} and C_2AH_8 and that the silica restricts the formation of gibbsite in both cements, this implies that the silica slows the process of conversion in the CACP. It can also be observed that silica favors the formation of Stratlingite (C_2ASH_8), this implies that silica increases mechanical strength [177, 271].

Figure 45a and 46b shows the formation of the same hydrated phases independent of the alumina content. Similarly, Figure 45c and 46d shows the formation of the same hydrated phases independent of the alumina content.

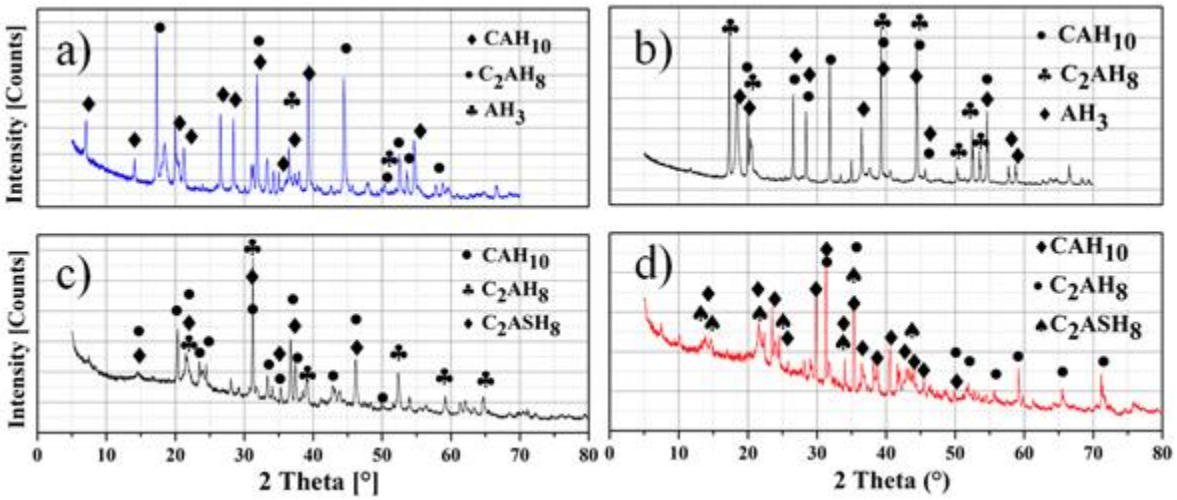

Figure 45. XRD Images, W/C=0.4:
CACP 51wt%: silica content: a) 0wt%, c) 20wt%. CAC 71wt%: b) 0wt%, d) 20wt%.

Figure 46 shows the TGA curves for CACP 71wt% and CACP 71-20wt%. It can be seen that the main dehydration processes are observed in the temperature range of 200°C to 352°C. At temperatures above 352°C, anhydrous phases are observed. The dehydration temperatures observed for each phase are shown in Table 38. Decomposition temperatures (°C) of CAC hydration products obtained in this work.

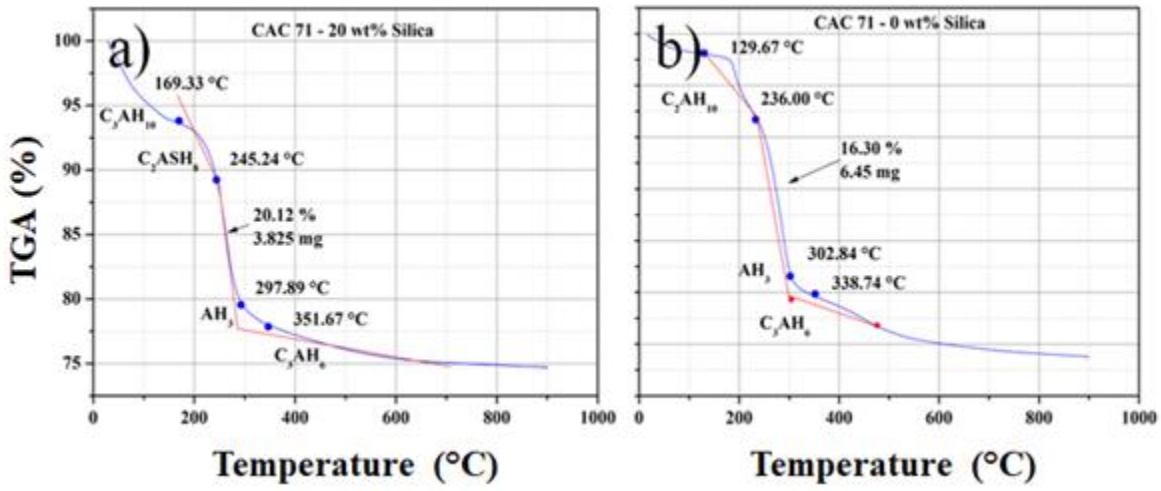

Figure 46. TGA curves for CAC 71wt% and CAC71-20wt%

Table 38. Decomposition temperatures (°C) of CAC hydration products obtained in this work.

Sample	CAH_{10}	C_2AH_8	C_2ASH_8	C_3AH_6	AH_3-gel	AH_3
CACP 71-0wt%	–	236.00	–	338.74	–	302.84
CACP 71-20wt%	129.67	–	245.24	351.67	–	297.89

The activation energies for the phase change in the dehydration process obtained by the TGA tests (see Figure 46. TGA curves for CAC 71wt% and CAC71-20wt% and using Friedman's model (see equation (17)) are shown in the Table 39 where R^2 is the determination coefficient.

Table 39. Activation energies in the range 336-800 °C – CAC 71-0wt%

Sample	Dehydration	Temperature range [°C]	R^2	Activation energy [kJ/mol]
CACP 71-0wt%	C_3AH_6 to CA	336-800	0.9870	13.71
CACP 71-20wt%	C_2ASH_6 to CA + S	336-800	0.9825	16.23

Figure 47 shows images of the different formulations before and after of creep tests. It can be seen that all the formulations exhibit surface fractures after being exposed to creep. It is difficult to establish from the images, a precise relationship of the amount of damage associated with the content of alumina and silica.

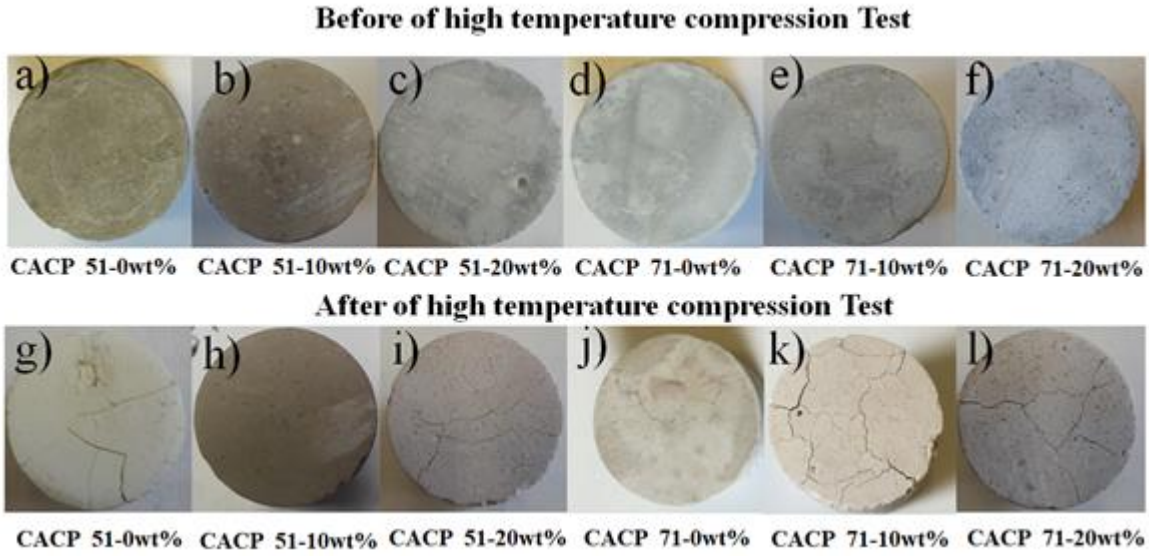

Figure 47. CACP images W/C=0.4:
Before of high temperature compression tests: CACP51: a) 0wt%, b) 10wt%, c) 20wt%. CACP 71: d) 0wt%, e) 10wt%, f) 20wt%, After of high temperature compression tests: CACP 51wt%: g) 0wt%, h) 10wt%, i) 20wt%. CACP 71: j) 0wt%, k) 10wt%, l) 20 wt%.

Figure 48 shows the experimental curves of high temperature compression tests (ECHTCT), 800°C, W/C=0.4, $\sigma = 0.3\,MPa$. Figure 48a, shows the ECHTCT for CACP 51-0wt%, 10wt% and 20wt%, it can be observed that the higher the alumina content, the greater the strain, but a non-linear behavior is evidenced, since the formulation with 0wt% silica strain in greater quantity than the 10wt% silica. Figure 48b shows the ECHTCT for CACP 71-0, 10 and 20wt%. It can be observed that lower the alumina content the greater the strain. A non-linear behavior is also shown; this is because the formulation of 10wt% silica shows a higher strain than the 20wt%.

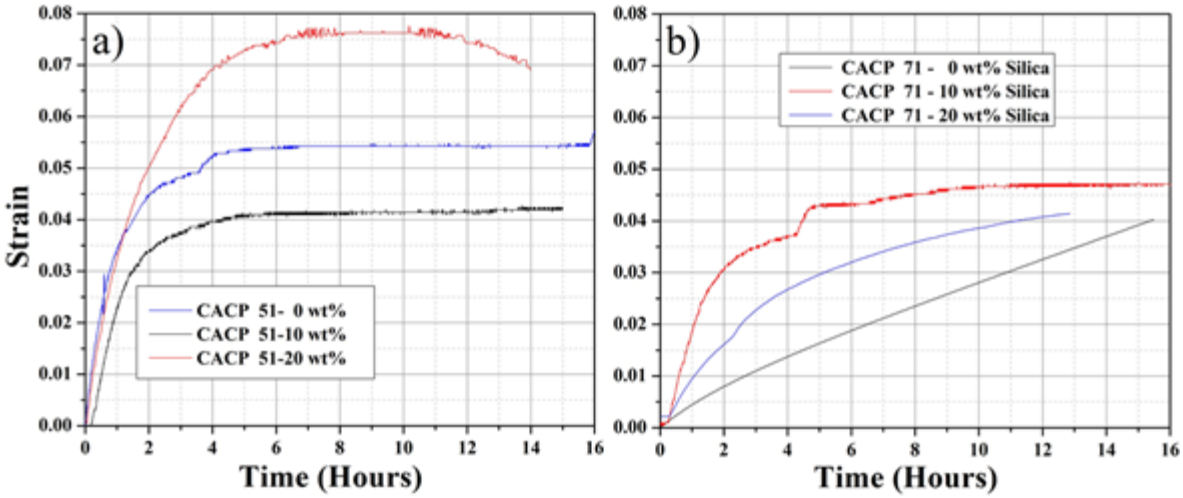

Figure 48. ECHTCT: a) CACP 51-0, 10 and 20wt%; b) CACP 71-0, 10 and 20 wt%.

Figure 49 shows the fit conducted by non-linear regression methods and implemented in the MATLAB software for the experimental ECHTCT to theta projection model (TPM), represented by equation (26), 800°C, W/C=0.4, $\sigma = 0.3\ MPa$. Figure 49a), b) and c) show the fit for the ECHTCT of CACP 51wt% with 0, 10 and 20 wt% silica, respectively. Figure 49 d), e) and f) show the fit for the ECHTCT of CACP 71-0, 10 and 20wt%, respectively. All curves were adjusted independently.

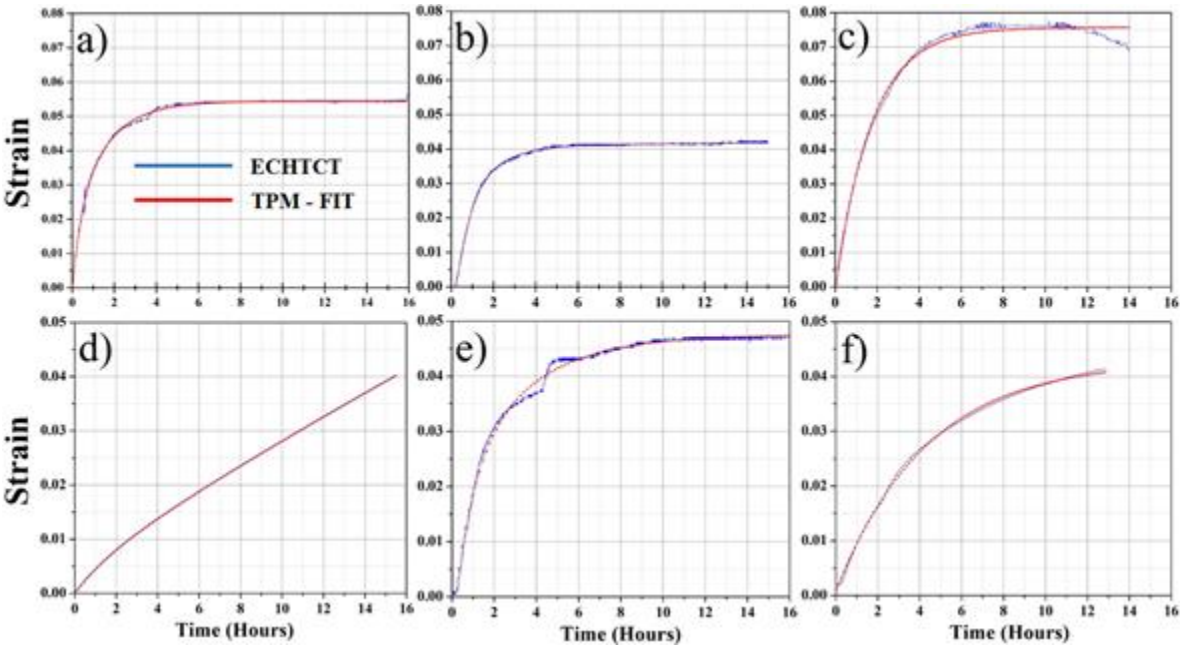

Figure 49. ECHTCT fit using the theta projection model (TPM):
CACP 51: a) 0wt%, b) 10wt%, c) 20wt%. CACP 71: d) 0wt%, e) 10wt%, f) 20wt%.

The values of the parameters θ_1, θ_2, θ_3 and θ_4 found by the TPM are showed in the Table 40.

Table 40. Estimated values of the parameters θ_1, θ_2, θ_3 and θ_4 - TPM

	Formulations – Silica content (wt%)					
	CACP 51			CACP 71		
Parameters	0	10	20	0	10	20
θ_1	0.9558	0.0490	0.4131	1.0221	0.0473	0.8119
θ_2	0.9980	0.9371	0.7936	0.7090	0.4791	0.9458
θ_3	0.9503	0.8505	0.7508	0.8140	0.7917	0.7693
θ_4	0.0998	0.0685	0.03726	0.0931	0.0939	0.0940

The values for the different formulations of the lifetime (T_m), the minimum creep rate ($\dot{\epsilon}_m$), stress exponent - power law n and activation energy creep Q and are shown in the Figure 50 (for notation of the formulations, see Table 41).

From Figure 50a and 51b, the inverse relationship between the minimum time of creep and the minimum creep rate can be seen, as expected.

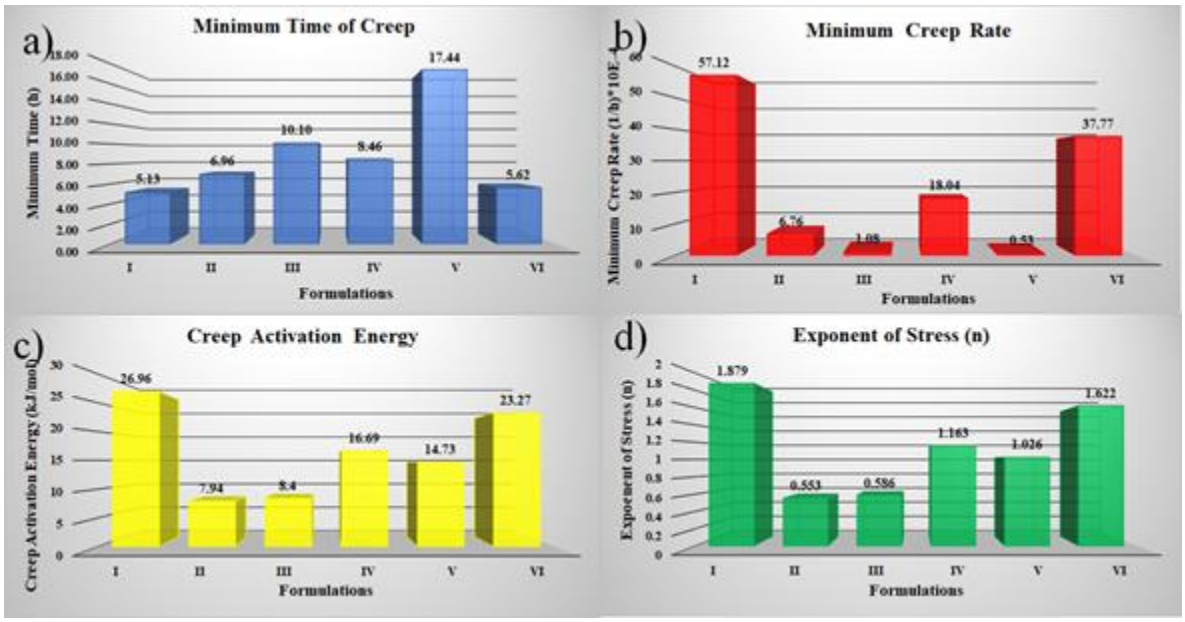

Figure 50. Values of the parameters calculated with TPM.

Table 41. Formulations**:** Creep parameter values.

I	II	III	IV	V	VI
	CACP 51			CACP71	
0wt%	10wt%	20wt%	0wt%	10wt%	20wt%

The rate values of the internal variables associated with the general hardening (H), the recovery rate (R) and the damage by creep (W). $\dot{H}, \dot{R}, \dot{W}$ were calculated with equations (29) and (30).

Figure 51 summarizes the magnitudes of all calculated values and shows the behavior of the minimum time of creep with respect to the minimum rate to visualize more easily the behavior of these parameters, in relation to each formulation. It can be established from Figure 51a the small values of theta 4 with respect to the values of theta 1, 2 and 3 in all the formulations. This indicates that stage 3 of creep is not presented with greater significance, as can be seen also in the curves of Figure 49. Figure 51b shows a low stress exponent in all formulations, which shows that the creep is diffusive and is not governed by a power law.

In addition, the activation energy and the minimum creep speed a non-linear behavior is presented in relation to the type of cement and silica contents. Figure 51c shows that recovery is almost zero in all formulations. The parameters of hardening and damage creep presents a non-linear behavior in relation to the type of cement and silica contents. Figure 51d shows a decreasing behavior of the minimum rate of creep in relation to the minimum time. This is because the greater the minimum time of creep, the lower the strains registered in the life of the material, and therefore it will have a minimum rate of creep and presents a highly non-linear behavior in relation to the type of cement and silica contents.

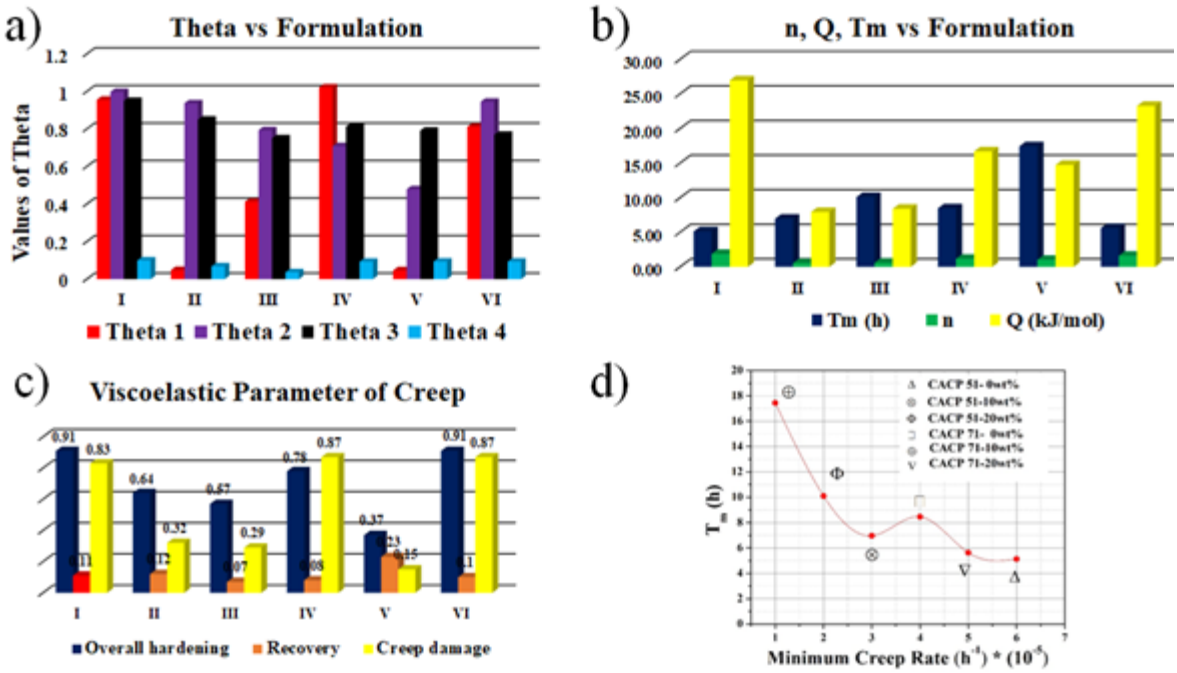

Figure 51. Graphs of calculated values: a) Magnitude of the Theta values with respect the material formulation; b) tm: Magnitude of the minimum time values of creep, n: exponent of stress and Q: activation energy vs formulation; c) Magnitude of the values of the internal variables in each formulation; d) minimum time vs minimum creep rate.

The values of the constant A and p are determined with the phenomenological equation (35) [288]; which is equivalent to equation (22) [288] and the letters denote the same meaning,

with an approximate grain size of $d \sim 4\ \mu m$ (see Table 42) and the values of $(n), \dot{\epsilon}$ and Q already calculated, (see Figure 51).

$$\dot{\epsilon} = A * \frac{\sigma^n}{d^p} * Exp\left(-\frac{Q}{RT}\right) \tag{35}$$

The calculated values for A, n and p are shown in Table 42.

Table 42. Calculated parameter values: Values of stress exponent (n), inverse size grain exponent (p), and constant (A), 800°C, σ = 0.3MPa.

	CACP 51wt%			CACP 71wt%		
Parameter	0wt%	10wt%	20wt%	0wt%	10wt%	20wt%
A	1	1	9	1	34	1
n	1.9	0.6	0.6	1.2	1.01	1.6
p	1	1	1	1	1	1

With the experimental values found for n y p, and with the help results reported by other researchers, it can be conjectured that the part of the damage caused by creep is governed by the mechanisms of Rachinger sliding. Sliding accommodated by formation of grain boundary cavities, in all the formulations.

8.4 ANALYSIS OF CREEP AND CALCULATION OF ACTIVATION ENERGIES

Figure 52a and 53b show images of SEM tests. You can see the cracks generated by the damage due to the effect of the temperature and the applied stress. The failure of ceramic materials operating in the creep range may be the result of growth of a dominant crack or by the accumulation of damage in the material [85]. In this way, the cracks observed are the result of damage caused by various factors such as the microcrack propagation, residual stress and creep. Figure 52c, 53d, 532e and 53f shows triple points where cracks are generated.

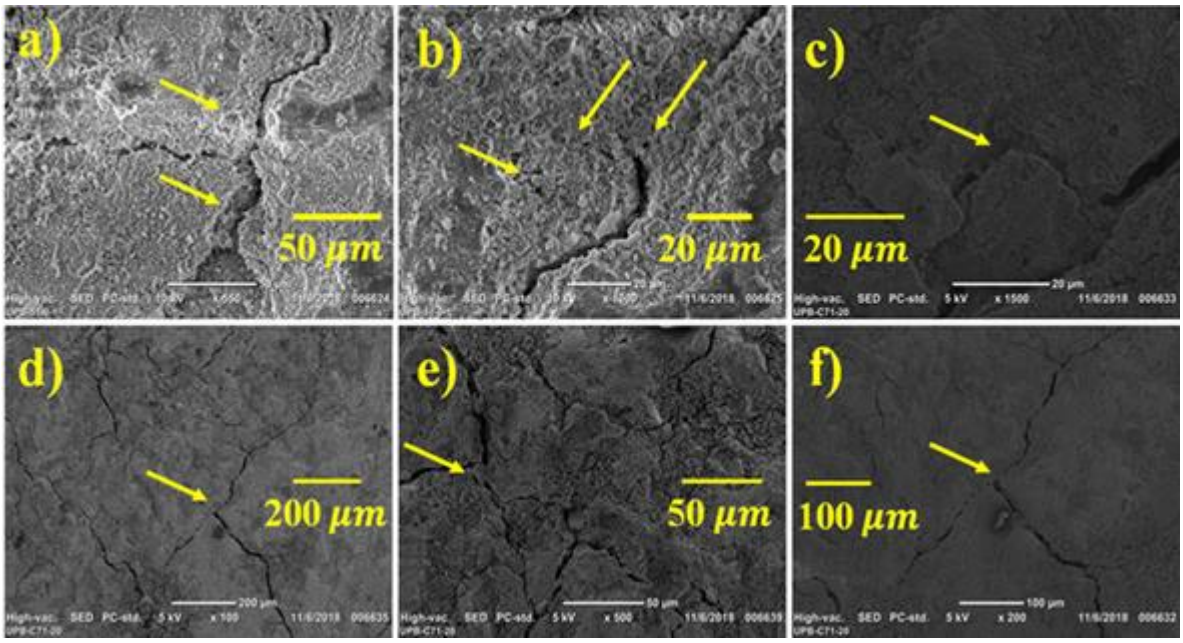

Figure 52. SEM images for CACP exposed to creep at 800°C, 0.3MPa, W/C=0.4:
a) CACP 51wt%, 50μm; b) CACP 51wt% , 20μm; c) CACP 71- 20wt%, 20μm; d) CACP 71- 20 wt% , 200μm; e) CACP 71- 20 wt%, 50μm; f) CACP 71- 20 wt%, 100μm.

While slow crack growth is a direct extension of a crack by diffusion of atoms through the tip of the crack, creep fracture is a process of nucleation, growth and coalescence of cavities along the grain boundary of a non-homogeneous localized way [289].

Observations of the creep fracture process have revealed that the cavities are nucleated mainly in the grain boundaries that are normal to the stress load. These cavities grow under the influence of high temperature mechanisms such as the diffusion of the grain limit, the sliding of the grain limit, and creep [86]. Then they join together to form micro grain boundary cracks, and finally an intergranular fracture occurs when these micro fissures join to form a macroscopic crack. It should be noted that because cavitation occurs in a non-homogeneous and localized manner, it would induce localized stresses that, in turn, would modify the stress field [175,289–291] and the analysis of stress during creep fracture is a very complex problem.

The activation energy was calculated in the absence of stress (see Table 39) and with stress (ECHTCT), see Figure 50c. Activation energy that is generated from the creep speed measurement is apparent, because it is associated with total strain, both the strain generated by creep and other factors, are included.

Therefore, in the first stage of creep or transient creep, the stress dependence of the strain rate must occur at low stresses at high temperatures and since the propagation of localized cracks has been invoked, which allows increased strains rates. If the temperature were restricted to this transition regime, and a straight line relationship was assumed, a measured activation energy value would be observed higher than that of a diffusion controlled process [292].

The thermal analysis for samples CACP 71wt% and CACP 71-20wt% at 800°C revealed activation energies of 13.71 and 16.23 kJ/mol respectively, see Table 38. The energies

provided by the modeling of the creep curves at 800°C for CACP 71wt% and CACP 71-20wt%, are 16.69 and 23.27 kJ/mol respectively, see Figure 50. Therefore, Q (activation energy of creep for CACP 71wt% (800°C)) minus Q (activation energy by temperature effect of CAC 71wt% (800°C)) = (16.69 – 13.71) kJ/mol = 2.98 kJ/mol. This implies that the damage generated exclusively by creep is associated with 2.98 kJ/mol. Similarly, Q (activation energy of creep for CACP 71-20wt% (800°C)) minus Q (activation energy by temperature effect of CACP 71-20wt% (800°C)) = (23.27 - 16.23) kJ mol = 7.04 kJ/ mol. This implies that the damage generated exclusively by creep has an energy of 7.04 kJ/mol associated with CACP 71-20wt% formulations, which implies that silica increases the resistance to creep damage.

8.5 DISCUSSION

Grain boundary sliding is a mechanism of strain of materials that includes the displacement of the grains with each other at high homologous temperature and low deformation rate [293]. This relative movement increases the stress at the points where there are restrictions for the movement, particularly in the triple points, resulting in a posterior diffusion or fracture strain. This mechanism is the main reason for the failure of the ceramic at high temperatures due to the formation of the vitreous phase at its grain boundary [293] as can be seen in this work. Grain boundary sliding is a mechanism of strain of creep, not described in polycrystalline materials with a single sliding mechanism, and in which grain movement must be accommodated by cavities formation, diffusion, and in the case of metallic materials, by the movement of dislocations [294].

It has been demonstrated according to the values given by n and p, that all the formulations have a Rachinger sliding creep mechanism. This is because there is no evidence of a change in the size of the grains, which implies that the silica content does not change the proper sliding mechanism, but the samples without silica content (Figure 52a and 53b) show formation of cavities near the grain boundary. It is known that silica favors the decrease of pore in CACP [197,245], which could be the reason because the formulations without silica show cavity formation, while for samples containing silica, no cavities were formed. It is observed (see Figure 52c, 53d, 53e and 53f) that sliding with a continuous glassy phase at the boundary does not show the formation of cavities, which implies that the energy released in the strain is transmitted through the cracks formed, which establishes another reason to conclude that silica content improves creep resistance. Also, for three formulations with silica content, the strain rates are much lower than for the formulations without silica content, which suggest that silica increases the resistance in CACP.

The obtained low values of the stress exponent were associated to the fact that the creep of a ceramic material hardly involves intra-granular mechanisms, since for overcoming its activation is required a very high stress that would produce breakage beforehand. Because of this fragile nature of ceramic materials, at high temperature, diffusive processes dominate.

A creep strain of 0.03 was obtained for CACP 71-20wt% by integrating equation (27) and using the minimum time value, tm = 5.62 hours (see Figure 50a), a temperature of 800°C and an activation energy for creep of 7.04 kJ/mol. The total strain was about 0.045 for the same material (see Figure 49f), which implies that a strain of the order of 0.015 (0.045-0.03) is due to factors other than creep, possibly due to crack propagation. A similar calculation for CACP 71-0wt%, with a value for the exclusive activation energy for creep of 2.98 kJ/mol, tm of

8.46 hours and temperature of 800°C, results in a creep strain of 0.02. Total strain of the order of 0.04 (see Figure 49d), this implies that a strain of 0.02 (0.04 -0.02) is due to factors other than creep, which may be crack propagation or residual thermal stress effects.

Therefore, for CACP 71-20wt%, approximately 75% of the strain is due to creep and the remaining 25% is due to cracking; while for CACP 71-0wt%, approximately 50% of the strain is due to creep and the remaining 50% is due to cracking. These results are summarized in Figure 53, where the silica contents is associated to decrease the propagation of cracks and channels the energy to propagation and thus to increase the creep contribution [197,245].

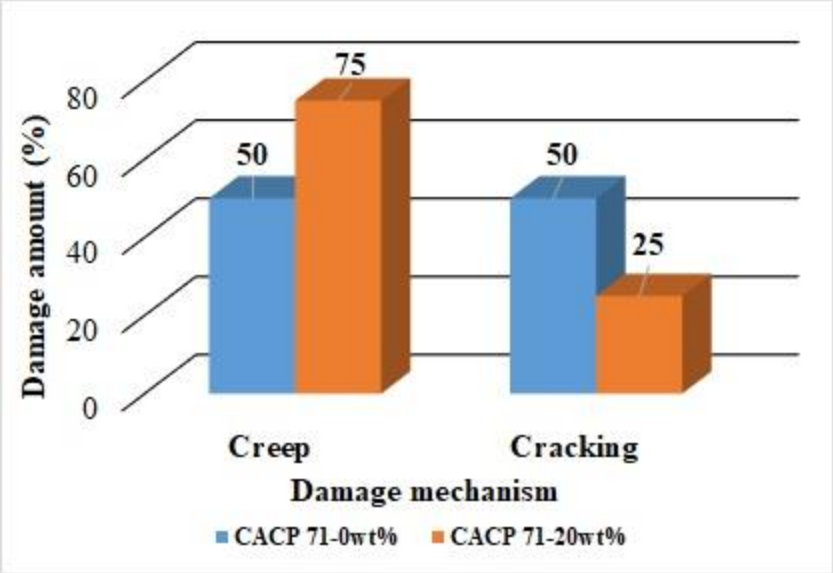

Figure 53. Damage mechanism by weight.

8.6 CONCLUSIONS

The main conclusions of this investigation are:

a) When CACP are under high temperature compression tests, cracking and creep damages appeared, which has been analyzed in this investigation.
b) Formulations with silica content have greater resistance to creep than those that do not have silica.
c) Via non-isothermal thermal and theta projection methods was estimated how much damage is due exclusively to creep when the samples are subjected to high temperature compression tests. It was found that for CACP 71-20wt%, approximately 75% of the damage is due to creep and the remaining 25% due to other mechanisms, possibly crack propagation for CACP 71-0wt%, approximately 50% of the damage is due to creep and the remaining 50% due to other mechanisms, possibly crack propagation. This implies that although silica favors creep strain, it decreases the amount of damage caused by total thermal strain as can be achieved see Figure 53.
d) Using TPM were calculated all the creep parameters. It was found that all the studied formulations present a precarious phase III of creep, this is due to the fragile nature of the CACPs, the minimum strain rate decreases with increasing the minimum time of

creep and present an almost zero recovery. Formulations with silica content have greater strength to creep than those that do not have silica.

e) Using TPM can reveal the creep micro mechanisms that govern the strain, supported by the literature and the calculation of the exponent of stress (n) and inverse size grain exponent (p). It could be concluded that all the formulations studied have a sliding creep mechanism Rachinger, that is, the silica does not change the sliding mechanism.

9. CHAPTER 9. GENERAL CONCLUSIONS AND SOME RECOMMENDATIONS

9.1 GENERAL CONCLUSIONS

The characteristics of the microstructure, mechanical properties and chemical composition were determined to know the initial conditions of the calcium aluminate cement. The results obtained are shown in chapter 4. This represents the fulfillment of the first specific objective proposed in this work.

It was evaluated the effect of temperatures (500, 800 and 1000 °C) on CACP and CACP added with silica, for different water/cement ratios, on the microstructure and the damage occurred was quantified.

It was observed that the samples with higher alumina content and higher W/C, show a greater number of cracks. The fact that higher W/C favors the conversion process, explains why the samples with higher W/C show a greater number of cracks in relation to the samples with lower W/C. It was also observed that at higher temperatures and low W/C, there is a greater probability of cracks of greater length and the alumina content also favors the formation of cracks of greater lengths. It could be established that silica restricts the formation of the mineral phases of C_2AH_8 and Gibbsite (AH_3) in the hydration process and favors the formation of stratlingite (C_2ASH_8), which implies that it avoids the conversion process and therefore improves mechanical strength and the values of the activation energies obtained for the formulation of CACP 71-0wt% for different phases, were in the range of 12.02 to 16.41 kJ/mol and for the formulation of CACP 71-20wt%, in the range of 7.7 to 16.23 kJ/mol.

This represents the fulfillment of the second and third specific objective.

A phenomenological mathematical model is proposed, which describes the behavior at temperatures (500, 800 and 1000°C) in CACP in relation to the microstructure, type of cement and the water/cement ratio.

This model is given by the following expression

$$\delta_j^i = 8\omega k_R 10^{-5} T^2 - 0.1364\omega k_R T + 66.28\omega k_R$$

where

T : Temperature °C
δ : Amount of damage (mm)
i : Index that indicates the type of cement paste, takes values of 1 and 2. When $i = 1$, it refers to CACP51 and $i = 2$, it refers to CACP71.
j : Index that labels each formulation, takes values of 1,2 and 3.
ω: Water/Cement ratio. It takes values of 0.25, 0.3 and 0.4.
k_R: It is an adjustment factor. It takes values depending on the values of the pair of indices i, j, as follows:

i	j	R
1	*1*	*1,2 and 3*
1	*2*	*4, 5 and 6*
1	*3*	*7, 8 and 9*
2	*1*	*10, 11 and 12*
2	*2*	*13, 14 and 15*
2	*3*	*16, 17 and 18*

where

$k_1 = k_2 = k_3 = k_{10} = 1;\ k_4 = 0.42; k_5 = 0.46;, k_6 = 0.62;\ k_7 = 0.94; k_8 = 1.23; k_9 = 1.37; k_{11} = 1.4;\ k_{12} = 1.62; k_{13} = 1.25; k_{14} = 1.39; k_{15} = 1.33; k_{16} = k_7 = 0.94;\ k_{17} = 0.89$.

Additionally, a creep damage analysis was made, the phenomenological models for creep found with the theta projection method for the different formulations are:

CACP51-0wt% silica

$$\epsilon = 0.9558(1 - e^{-0.9980t}) + 0.9503(e^{0.0998t} - 1)$$

CACP51-10wt% silica

$$\epsilon = 0.0490(1 - e^{-0.9371t}) + 0.8505\ (e^{0.0685t} - 1)$$

CACP51-20wt% silica

$$\epsilon = 0.4131(1 - e^{-0.7936t}) + 0.7508\ (e^{0.0373t} - 1)$$

CACP71-0wt% silica

$$\epsilon = 1.0221(1 - e^{-0.7090t}) + 0.814031(e^{0.0931t} - 1)$$

CACP71-10wt% silica

$$\epsilon = 0.0473(1 - e^{-0.4791t}) + 0.7917(e^{0.0939t} - 1)$$

CACP71-20wt% silica

$$\epsilon = 0.8119(1 - e^{-0.9458t}) + 0.7693(e^{0.0940t} - 1)$$

It was found that for CACP 71-20wt% silica content, approximately 75% of the damage is due to creep and the remaining 25% of damage is due to other mechanisms, possibly to crack propagation. For CACP 71-0wt%, that is, samples without silica, approximately 50% of the damage is due to creep and the remaining 50% due to other mechanisms, possibly crack propagation. This implies that, although silica favors creep deformation, it decreases the amount of damage caused by total thermal strain, as can be seen in Figure 53.

It was found that all the studied formulations present a very precarious creep tertiary phase, this is reflected by the low values obtained for θ_3 and θ_4, and is due to the fragile nature of the CACP, the minimum deformation rate decreases with increasing minimum time. of creep and has almost no recovery.

The micro-mechanisms that govern creep strain, estimated from the estimated values of θ_s was found that all the studied formulations present a type of Rachinger slip-type creep micro-mechanism, this implies that the silica content does not influence the type of creep micro-mechanism.

This represents the fulfillment of the fourth specific objective. In this way, the general objective of this thesis is fully accomplished.

9.2 SOME FINAL COMMENTS AND RECOMMENDATIONS

CACs are the raw material to create high performance materials in many industry sectors, such as pharmaceuticals, cosmetics, cement and construction, ceramics (traditional, decorative, refractory, new composite materials, smart ceramics, nanostructured, with gradients)., among many others), the electronic device industry. CACs mixed with other cements serve as the basis for creating refractory paints, varnishes, and other materials to meet specific demands.

CACs are exceptional cements, with high mechanical, thermal, strong resistance to chemical attack, early resistance, high thermal stability, resistance to abrasion. The applications of the CAC are multiple, but to be the beneficiary of all their strengths, it is recommended to take into account 4 fundamental aspects:

1. Know the conditions of application of materials manufactured from CAC, because these conditions of use define the conditions of manufacture; the adequate alumina content, the W/C ratio, the curing temperatures, and avoid problems such as conversion, aluminosis or cracking.
2. Know the kinetics, to understand its behavior when mixed with other cements or minerals. When subjected to heating between 20 and 1000 °C, knowing the kinetics is essential to unveil the micro-mechanisms that govern the formation of phases, therefore, the residence times at a certain temperature and the channels in which they are can be established. they form certain specific phases that are required for a specific purpose. For these reasons, knowledge of the behavior and processes related to heating is essential for the creation of refractory ceramics and new materials based on CAC.
3. Knowledge of kinetics is also essential to direct phase formation from the manufacturing of CACs from their raw materials. It is another fundamental reason to motivate the research of kinetics in the manufacturing of CAC and to have control in the design of new materials based on CAC for any of its potential applications.
4. Micro silica is a good additive to CACs for phase formation with potential refractory applications.

9.3 FUTURE WORKS

Thermal analysis is essential in the design and manufacture of advanced materials. The studies carried out in this thesis can be applied, according to the review of the state of the art, in 5 complementary areas, which are shown in the Figure 54.

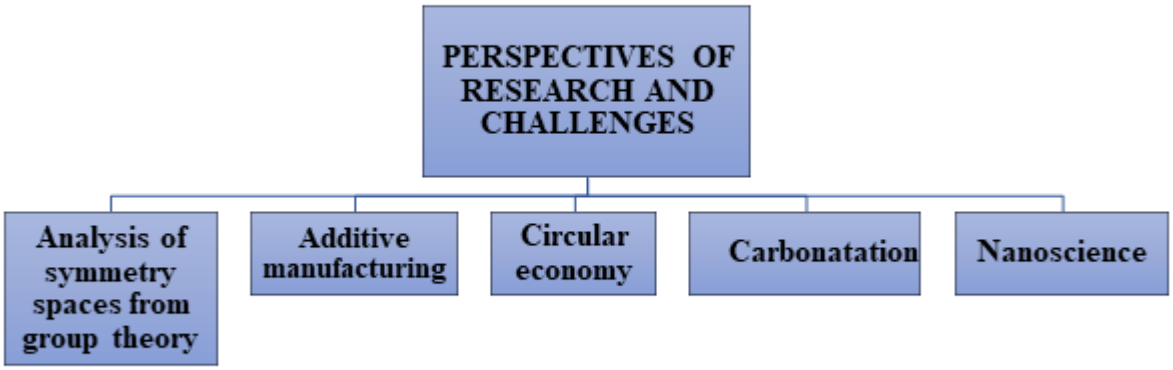

Figure 54. Perspectives of research and challenges with CAC

Analysis of symmetry spaces from group theory - Nanoscience

The fundamental chemical interactions that control the structure and performance of cements have been intensively investigated, but the complex and crystallographic nature of the phases that form in hardened cements poses difficulties in obtaining detailed information on the local structure, reaction mechanisms and kinetics [295–298]. Solid state nuclear magnetic resonance spectroscopy can solve the key atomic structural details within these materials and the proper use of X-ray diffraction-generated diffractograms used with the focus of unveiling crystalline symmetry spaces sets out all promising lines of research. to generate models that will allow highly advanced designs of new materials generated from the knowledge of their quantum behavior and their adhesion with various suitable nano materials suggested by the same theoretical analyzes.

Additive manufacturing

Additive manufacturing technologies (also known as 3D-3DP printing) have advanced rapidly in various industrial sectors, including aerospace, automotive, medical, architecture, arts and design, food and construction. Transition from visualization and prototyping stages to functional and real part replacement opens up more design possibilities. Among the various AM applications, construction applications. There are obvious challenges and risks to integrating AM into large-scale construction. Thus, progress in commercialization appears to be advancing at a slow pace since only a few large-scale 3DP trials for construction can be found in the literature [299–301]. The use of CACs to generate AM-friendly mixtures makes this a whole virgin and unexplored research area with great prospects for success and applications.

Circular economy

The search in the Scopus database (June -2020) with the keywords calcium aluminate cement + circular economy, did not show results. This shows the few works that have been carried out in the management of solid waste generated from manufactured products based on CAC, for these reasons, new processes on CAC-based waste and the circular economy become an area of great projection for the industry. modern and great environmental impact.

Carbonatation process

CAC paste is known to react with atmospheric carbon dioxide. Carbonation causes numerous chemical-mechanical changes in the cement paste. Carbonation under certain conditions improves certain properties of the cement material [219,302–304] . For these reasons, the active use of carbonation as a tool to manipulate certain properties of CAC-based materials is a very prospective research area, because it includes possible applications in fields such as: improvement of fiber-reinforced cementitious compounds, concrete recycling and immobilization of waste.

It is recommended to make a more exhaustive study of the carbonation of calcium aluminate cement pastes without the presence of alkalis, taking into account the exposure time to CO_2, the alumina content, the relative humidity, the CO_2 concentration and of course the temperature. of exposition.

It is also strongly recommended to do a more exhaustive study of creep damage. According to the review of the state of the art, creep research in calcium aluminate cement pastes is very incipient, and this knowledge is important when using these cements to make refractory ceramics or construction materials. In this way, studying creep for calcium aluminate cements, at 500, 800 and 1000 ° C, with various alumina contents, for different water to cement ratios, becomes very relevant.

10. REFERENCES

1. K. Scrivener, Calcium aluminate, *Adv. Concr. Technol. Set* (2003) 1.
2. V. V Skurikhin et al., High-alumina cembor cements for low-cement refractory concretes, *Refract. Ind. Ceram.* 53 (1) (2012) 4–8.
3. K.L. Scrivener, J.-L. Cabiron, and R. Letourneux, High-performance concretes from calcium aluminate cements, *Cem. Concr. Res.* 29 (8) (1999) 1215–1223.
4. K.L. Scrivener, Advanced concrete technology: constituent materials, *Butterworth-Heinemann* (2003).
5. E. Nonnet et al., In Situ X-ray Diffraction and Young's Modulus Measurement during Heat Treatment of High-Alumina Cement Castables, *J. Am. Ceram. Soc.* 84 (3) (2001) 583–587.
6. J. Loof et al., Mechanical properties of a permanent dental restorative material based on calcium aluminate, *J. Mater. Sci. Mater. Med.* 14 (12) (2003) 1033–1037.
7. S.J. Kalita et al., Porous calcium aluminate ceramics for bone-graft applications, *J. Mater. Res.* 17 (12) (2002) 3042–3049.
8. C. Zhao and D. Chen, Synthesis of CaAl2O4: Eu, Nd long persistent phosphor by combustion processes and its optical properties, *Mater. Lett.* 61 (17) (2007) 3673–3675.
9. S.-W. Choi and S.-H. Hong, Size and morphology control by planetary ball milling in CaAl2O4: Eu2+ phosphors prepared by Pechini method and their luminescence properties, *Mater. Sci. Eng. B* 171 (1–3) (2010) 69–72.
10. K.L. Scrivener and A. Capmas, Calcium aluminate cements in Lea's Chemistry of cement and concrete ed PC Hewlelt, (1998).
11. S. Banerjee, *Monolithic refractories: a comprehensive handbook*, *World Scientific*, (1998).
12. C. Parr et al., The advantages of calcium aluminate cement containing castables for steel ladle applications, *Proc. ALAFAR* 2004 (2004) 10–15.
13. J.P. Coughlin, Heats of formation of crystalline CaO· Al2O3, 12CaO· 7Al2O3, and 3CaO· Al2O3, *J. Am. Chem. Soc.* 78 (21) (1956) 5479–5482.
14. B.S. Hemingway, Comment on" Thermodynamic properties of calcium aluminates", *J. Phys. Chem.* 86 (14) (1982) 2802–2803.
15. H.G. Midgley and A. Midgley, The conversion of high alumina cement, *Mag. Concr. Res.* 27 (91) (1975) 59–77.
16. T.W. Song, S.H. Choi, and K.S. Han, Activation of hydraulic properties of the compound CaOÁ2Al2O3, *in* Proc. Int. Symp. Calcium Aluminate Cem. E&FN Spon, London, (1990): pp. 372–377.
17. C.H. Fentiman et al., The effect of curing conditions on the hydration and strength development in fondu: slag, *Calcium Aluminate Cem.* (1990) 272–281.
18. R.J. Mangabhai and F.P. Glasser, *Calcium Aluminate Cements 2001*, *IOM communications London*, (2001).
19. N. Ukrainczyk et al., Dehydration of a layered double hydroxide—C2AH8, *Thermochim. Acta* 464 (1–2) (2007) 7–15.
20. N. Ukrainczyk, T. Matusinović, and J. Šipušić, Microstructural Model of Calcium Aluminate Cement Hydration, *in* Miner. To Mater. Conf. Bridg. Gap between Miner.

Mater., (2008).
21. K.L. Scrivener and H.F.W. Taylor, Microstructural development in pastes of a calcium aluminate cement, *Calcium Aluminate Cem.* (2014) 41–51.
22. H.F.W. Taylor, *Cement chemistry*, *Thomas Telford*, (1997).
23. W.E. Lee et al., Castable refractory concretes, *Int. Mater. Rev.* 46 (3) (2001) 145–167.
24. A. Capmas, D. Menetrier-Sorrentino, and D. Damidot, Effect of temperature on setting time of calcium aluminate cements, *Calcium Aluminate Cem.* (1990) 65–80.
25. J.H. Sharp et al., The effect of admixtures on the hydration of refractory calcium aluminate cements, *Calcium Aluminate Cem.* (1990) 127–141.
26. A.-M. Azad, L.L.W. Shyan, and M.A. Alim, The AC electrical characterization of the solid-state reaction derived CaSnO3, *J. Mater. Sci.* 34 (14) (1999) 3375–3396.
27. C. Parr et al., Effect of formulation parameters upon the strength development of calcium aluminate cement containing castables, *Refractories(Tokyo)* 56 (5) (2004) 238–247.
28. L. Wang et al., Enhancing the green mechanical strength of colloidal silica-bonded alumina castables using a silane coupling agent, *Ceram. Int.* 42 (9) (2016) 11496–11499.
29. A.P. Shrimali, Studies on phase formation in high alumina cement by varying manufacturing parameter and effect of those phases in refractory castable, (2013).
30. F.A. Cardoso et al., Effect of curing time on the properties of CAC bonded refractory castables, *J. Eur. Ceram. Soc.* 24 (7) (2004) 2073–2078.
31. J.F. Zapata, M. Gomez, and H.A. Colorado, Structure-property relation and Weibull analysis of calcium aluminate cement pastes, *Mater. Charact.* 134 (2017) 9–17.
32. S.M. Bushnell-Watson and J.H. Sharp, On the cause of the anomalous setting behaviour with respect to temperature of calcium aluminate cements, *Cem. Concr. Res.* 20 (5) (1990) 677–686.
33. P. Barnes and J. Bensted, *Structure and performance of cements*, *CRC Press*, (2014).
34. A.P. Da Luz, M. de A.L. Braulio, and V.C. Pandolfelli, *Refractory castable engineering*, *FIRE, Federation for International Refractory Research and Education*, (2015).
35. J.M.R. Mercury et al., Hidratación de los cementos de aluminatos de calcio (Parte I), *Boletín La Soc. Española Cerámica y Vidr.* 42 (5) (2003) 269–276.
36. M.C. Alonso et al., Calcium aluminate based cement for concrete to be used as thermal energy storage in solar thermal electricity plants, *Cem. Concr. Res.* 82 (2016) 74–86.
37. L. Xu et al., Influence of curing temperatures on the hydration of calcium aluminate cement/Portland cement/calcium sulfate blends, *Cem. Concr. Compos.* 80 (2017) 298–306.
38. V. Antonovič et al., The effect of temperature on the formation of the hydrated calcium aluminate cement structure, *Procedia Eng.* 57 (2013) 99–106.
39. F. Guirado, S. Galı, and J.S. Chinchon, Thermal decomposition of hydrated alumina cement (CAH10), *Cem. Concr. Res.* 28 (3) (1998) 381–390.
40. A.P. Luz and V.C. Pandolfelli, CaCO3 addition effect on the hydration and mechanical strength evolution of calcium aluminate cement for endodontic applications, *Ceram. Int.* 38 (2) (2012) 1417–1425.
41. M. Pérez, T. Vázquez, and F. Triviño, Study of stabilized phases in high alumina cement mortars Part I Hydration at elevated temperatures followed by carbonation, *Cem. Concr. Res.* 13 (6) (1983) 759–770.

42. F. Sorrentino, Mechanisms of hydration of calcium aluminate cements, *Mater. Sci. Concr.* 6 (1995) 41–90.
43. J. SULIKOWSKI and J. SAWKOW, INFLUENCE OF THE CA-TO-CA 2 RATIO ON THE PROPERTIES OF ALUMINOUS CEMENTS AND REFRACTORY CONCRETE CONTAINING CORUNDUM, *SILIKATTECHNIK Silikattechnik* 29 (6) (1978) 165.
44. S. Chatterjiand and A.J. Majumdar, Studies of the early stages of paste hydration of high alumina cements I: Hydration of individual aluminate, *Ind. Concr. Jour* (1966) 51–55.
45. M. Jung, Hydraulic properties of high-alumina cements, *Bull. La Soc. Fr. Ceram.* (98) (1973) 11–20.
46. H.R. Chudak et al., Zum Einsatz der differentialkalorimetrischen Analyse (DCA) bei der Überwachung der Tonerdezement produktion, *Silikattechnik* 33 (7) (1982) 197–199.
47. A. Negro, L. Montanaro, and A. Bachiorrini, On the reactivity of the cement clinkers components by means of laser granulometer, *Cem. Concr. Res.* 15 (2) (1985) 315–319.
48. R.N. Edmonds and A.J. Majumdar, The hydration of Secar 71 aluminous cement at different temperatures, *Cem. Concr. Res.* 19 (2) (1989) 289–294.
49. A.M. Neville, A STUDY OF DETERIORATION OF STRUCTURAL CONCRETE MADE WITH HIGH-ALUMINA CEMENT, *Proc. Inst. Civ. Eng.* 25 (3) (1963) 287–324.
50. S.F.M. LEA, C.H. Desch, and S.F.M. LEA, *The Chemistry of Cement and Concrete Revised Edition. by FM Lea, Edward Arnold*, (1956).
51. H.G. Midgley, Quantitative determination of phases in high alumina cement clinkers by X-ray diffraction, *Cem. Concr. Res.* 6 (2) (1976) 217–223.
52. B. Lothenbach et al., Thermodynamic modelling of the effect of temperature on the hydration and porosity of Portland cement, *Cem. Concr. Res.* 38 (1) (2008) 1–18.
53. T. Matschei, B. Lothenbach, and F.P. Glasser, Thermodynamic properties of Portland cement hydrates in the system CaO–Al2O3–SiO2–CaSO4–CaCO3–H2O, *Cem. Concr. Res.* 37 (10) (2007) 1379–1410.
54. A.C.C. Tseung and T.G. Carruthers, Refractory Concretes Based on Pure Calcium Aluminates Cements, *Trans. Brit. Ceram. Soc* 62 (1963) 305–320.
55. S. Mohmel et al., Investigations on the hydration behaviour of clinker phases of high alumina cements, *in* Unitecr'91. Second Unified Int. Tech. Conf. Refract. Glob. Adv. Refract. Prepr. Aachen, (1991).
56. S.R. Klaus, J. Neubauer, and F. Goetz-Neunhoeffer, How to increase the hydration degree of CA—The influence of CA particle fineness, *Cem. Concr. Res.* 67 (2015) 11–20.
57. S.R. Klaus, J. Neubauer, and F. Goetz-Neunhoeffer, Hydration kinetics of CA2 and CA—investigations performed on a synthetic calcium aluminate cement, *Cem. Concr. Res.* 43 (2013) 62–69.
58. F. Hueller et al., Influence of crystallinity and surface area on the hydration kinetics of CA2, *Cem. Concr. Res.* 89 (2016) 136–144.
59. C.M.M. Freitas, R.P. Rettore, and P.R.G. Brandao, Hydration and microstructure of CA sub 2 in the presence and in the absence of microsilica, *Third Euro-Ceram.*, 3 (1993) 277–282.

60. A.J. Majumdar et al., Blended high-alumina cements, *Ceram. Trans.* 16 (1990) 661–678.
61. A.J. Majumdar and B. Singh, Properties of some blended high-alumina cements, *Cem. Concr. Res.* 22 (6) (1992) 1101–1114.
62. P.K. Mehta and G. Lesnikoff, Conversion of CaO· Al2O3· 10H2O to 3CaO· Al2O3· 6H2O, *J. Am. Ceram. Soc.* 54 (4) (1971) 210–212.
63. C.M. George, Hydration kinetics of refractory aluminous cements and their influence on concrete properties, *Trans. J. Br. Ceram. Soc.* 79 (3) (1980) 82–90.
64. J. d'Ans and H. Eick, The system CaO–Al2O3–H2O at 20 C and the hardening of aluminous cements, *ZKG* 6 (1953) 197–210.
65. N.Y. Mostafa, Z.I. Zaki, and O.H.A. Elkader, Chemical activation of calcium aluminate cement composites cured at elevated temperature, *Cem. Concr. Compos.* 34 (10) (2012) 1187–1193.
66. I. of C.E. (Great B.S.A. Committee, S.F.M. Lea, and C.M. Watkins, *The Durability of Reinforced Concrete in Sea Water: Twentieth Report of the Sea Action Committee of the Institution of Civil Engineers, HM Stationery Office*, (1960).
67. H.G. Midgley, The use of thermal analysis methods in assessing the quality of high alumina cement concrete, *J. Therm. Anal.* 13 (3) (1978) 515–524.
68. Y. Li et al., Melting and solidification of Pb nanoparticles embedded in an Al matrix as studied by temperature-modulated differential scanning calorimetry, *Philos. Mag. Lett.* 78 (1) (1998) 37–44.
69. A. Mitra, S. Palit, and I. Chattoraj, Crystallization and magnetic behaviour of Fe-Nb-Cu-Si-B alloys, *Philos. Mag. B* 77 (6) (1998) 1681–1691.
70. J.M. Papazian, Effects of SiC whiskers and particles on precipitation in aluminum matrix composites, *Metall. Trans. A* 19 (12) (1988) 2945–2953.
71. P.N. Adler and R. DeIasi, Calorimetric studies of 7000 series aluminum alloys: II Comparison of 7075, 7050 and RX720 alloys, *Metall. Trans. A* 8 (7) (1977) 1185–1190.
72. D.A.N. Li et al., A novel technique to prepare ultrafine Fe2O3 via hydrated iron (III) nitrate, *J. Mater. Sci. Lett.* 16 (6) (1997) 493–495.
73. L.C. Chen and F. Spaepen, Calorimetric evidence for the micro-quasicrystalline structure of'amorphous' Al/transition metal alloys, *Nature* 336 (6197) (1988) 366.
74. X. Cao et al., Controlling the particle size of amorphous iron nanoparticles, *J. Mater. Res.* 10 (11) (1995) 2952–2957.
75. S. Vyazovkin, *Isoconversional kinetics of thermally stimulated processes*, *Springer*, (2015).
76. M.E. Brown, D. Dollimore, and A.K. Galway, Comprehensive Chemical Kinetics, edited by RG Compton, CH Bamford & CFH Tipper, (1980).
77. S. Vyazovkin and C.A. Wight, Kinetics in solids, *Annu. Rev. Phys. Chem.* 48 (1) (1997) 125–149.
78. P. Holba and J. Šesták, Heat inertia and its role in thermal analysis, *J. Therm. Anal. Calorim.* 121 (1) (2015) 303–307.
79. P.J. Haines, *Thermal methods of analysis: principles, applications and problems*, *Springer Science & Business Media*, (2012).
80. A. Khawam and D.R. Flanagan, Solid-state kinetic models: basics and mathematical fundamentals, *J. Phys. Chem. B* 110 (35) (2006) 17315–17328.
81. J. Cai et al., New temperature integral approximation for nonisothermal kinetics,

AIChE J. 52 (4) (2006) 1554–1557.
82. J.M. Criado and A. Ortega, Modification of the hancock and sharp "lnln method" in order to perform the kinetic analysis of non-isothermal data, *Thermochim. Acta* 46 (2) (1981) 209–211.
83. J. Szczerba et al., The application of DTA and TG methods to investigate the non-crystalline hydration products of CaAl2O4 and Ca7ZrAl6O18 compounds, *Thermochim. Acta* 567 (2013) 40–45.
84. L. Scheinherrová and A. Trník, Hydration of calcium aluminate cement determined by thermal analysis, *in* AIP Conf. Proc., *AIP Publishing*, (2017): p. 40034.
85. M.I. Pope, Differential Thermal Analysis--A Guide to Technique and its Applications, (1977).
86. J. Baets, J. Devaux, and I. Verpoest, Toughening of basalt fiber-reinforced composites with a cyclic butylene terephthalate matrix by a nonisothermal production method, *Adv. Polym. Technol.* 29 (2) (2010) 70–79.
87. R.M.R. Wellen and E.L. Canedo, On the Kissinger equation and the estimate of activation energies for non-isothermal cold crystallization of PET, *Polym. Test.* 40 (2014) 33–38.
88. F. Noel, RC Mackenzie (Ed), Differential thermal analysis, Vol 1: Academic Press, London, 1970, xv+ 771 pp, price£ 1200, (1971).
89. E.S. Freeman and B. Carroll, The application of thermoanalytical techniques to reaction kinetics: the thermogravimetric evaluation of the kinetics of the decomposition of calcium oxalate monohydrate, *J. Phys. Chem.* 62 (4) (1958) 394–397.
90. E.S. Freeman and B. Carroll, Interpretation of the kinetics of thermogravimetric analysis, *J. Phys. Chem.* 73 (3) (1969) 751–752.
91. S. Vyazovkin, Kinetic concepts of thermally stimulated reactions in solids: a view from a historical perspective, *Int. Rev. Phys. Chem.* 19 (1) (2000) 45–60.
92. J.P. Redfern, Recent trends in thermal analysis, *Pure Appl. Chem.* 25 (4) (1971) 849–869.
93. A.P. Rollet and R. Bouaziz, L'Analyse Thermique (tome 1), *Paris* (1972).
94. J. Šesták, Errors of kinetic data obtained from thermogravimetric curves at increasing temperature, *Talanta* 13 (4) (1966) 567–579.
95. V.M. Gorbachev, Some aspects of Šestak's generalized kinetic equation in thermal analysis, *J. Therm. Anal. Calorim.* 18 (1) (1980) 193–197.
96. H. Schmalzried, *Chemical kinetics of solids*, *John Wiley & Sons*, (2008).
97. A.K. Galwey, Solid state decompositions: the interpretation of kinetic and microscopic data and the formulation of a reaction mechanism, *Thermochim. Acta* 96 (2) (1985) 259–273.
98. A.K. Galwey, Chemistry of solids, (1967).
99. W.W. Wendlandt, *Thermal methods of analysis*, (1974).
100. R.C. MacKenzie, *Differential thermal analysis*, (1970).
101. M.F. Zawrah et al., Synthesis, hydration and sintering of calcium aluminate nanopowder for advanced applications, *Comptes Rendus Chim.* 14 (6) (2011) 611–618.
102. M.F. Zawrah and N.M. Khalil, Synthesis and characterization of calcium aluminate nanoceramics for new applications, *Ceram. Int.* 33 (8) (2007) 1419–1425.
103. H. Boess, *Zementarme Feuerbetone: ihre Eigenschaften und ihr*

Trocknungsverhalten, *na*, (1985).
104. A. López-Delgado et al., *Study by DTA/TG of the formation of calcium aluminate obtained from an aluminium hazardous waste*, (2010).
105. C. Gosselin, E. Gallucci, and K. Scrivener, Influence of self heating and Li2SO4 addition on the microstructural development of calcium aluminate cement, *Cem. Concr. Res.* 40 (10) (2010) 1555–1570.
106. A.B. Tchamba et al., Formulation of calcium dialuminate (CaO· 2Al2O3) refractory cement from local bauxite, *J. Asian Ceram. Soc.* 3 (2) (2015) 164–172.
107. J. Soro, A. Smith, and C. Gault, Thermomechanical characteristics of calcium aluminate cement and sand tapes prepared by tape casting, *J. Eur. Ceram. Soc.* 26 (16) (2006) 3799–3807.
108. T. Chotard et al., Application of ultrasonic testing to describe the hydration of calcium aluminate cement at the early age, *Cem. Concr. Res.* 31 (3) (2001) 405–412.
109. Y. El Hafiane et al., Calcium aluminate cement tapes–Part II: Physical properties, *J. Eur. Ceram. Soc.* 34 (4) (2014) 1025–1033.
110. A. Carriço, J.A. Bogas, and M. Guedes, Thermoactivated cementitious materials–A review, *Constr. Build. Mater.* 250 (2020) 118873.
111. S. Klaus, Quantification of CA hydration and influence of its particle fineness during early hydration of calcium aluminate cement, 2015.
112. J.D.H. Donnay and H.M. Ondik, *Crystal Data: Determinative Tables Inorganic Compounds, US Department of Commerce, National Bureau of Standards*, (1973).
113. D. Müller et al., Solid-state 27Al NMR studies on polycrystalline aluminates of the system CaO-Al2O3, *Polyhedron* 5 (3) (1986) 779–785.
114. P. Tarte, Infra-red spectra of inorganic aluminates and characteristic vibrational frequencies of AlO4 tetrahedra and AlO6 octahedra, *Spectrochim. Acta Part A Mol. Spectrosc.* 23 (7) (1967) 2127–2143.
115. L. Fernández Carrasco et al., *Infrared spectroscopy in the analysis of building and construction materials*, *InTech*, (2012).
116. G.I. Zhmoidin, A.K. Chatterdzhi, and I.I. Plyusnina, Coordination of aluminum in calcium aluminates and oxyfluoroaluminates according to IR data, *J. Appl. Spectrosc.* 16 (6) (1972) 789–793.
117. R.I. Barnhisel and C.I. Rich, Gibbsite, Bayerite, and Nordstrandite formation as affected by anions, pH, and mineral surfaces 1, *Soil Sci. Soc. Am. J.* 29 (5) (1965) 531–534.
118. C. Pastor et al., Calcium aluminate cement hydration in a high alkalinity environment, *Mater. Construcción* 59 (293) (2009) 21–34.
119. L. Fernández-Carrasco and E. Vázquez, Reactions of fly ash with calcium aluminate cement and calcium sulphate, *Fuel* 88 (9) (2009) 1533–1538.
120. H.W. Van der Marel and H. Beutelspacher, *Atlas of infrared spectroscopy of clay minerals and their admixtures*, *Elsevier Publishing Company.*, (1976).
121. L. Reig et al., Influence of calcium aluminate cement (CAC) on alkaline activation of red clay brick waste (RCBW), *Cem. Concr. Compos.* 65 (2016) 177–185.
122. L.D. Frederickson, Characterization of hydrated aluminas by infrared spectroscopy, *Anal. Chem.* 26 (12) (1954) 1883–1885.
123. A. Gaki, T. Perraki, and G. Kakali, Wet chemical synthesis of monocalcium aluminate, *J. Eur. Ceram. Soc.* 27 (2–3) (2007) 1785–1789.
124. A.M. Brandt, Materials, Mechanical Properties and Performance, (2009).

125. R. Barborak, Calcium Aluminate Cement Concrete (Class CAC Concrete) TxDOT Special Specification SS-4497 Tip Sheet, *Constr. Bridg. Div. Texas Deparment Transp. Austin, TX, USA* (2010).
126. S.C. Yepes and M.Á.S. Barbudo, *El cemento de aluminato de calcio y sus prefabricados, Universidad de Alicante*, (2008).
127. E. Gartner, Are there any practical alternatives to the manufacture of Portland cement clinker?, *Struct. Concr. (Excluding Steel)* 2 (1.11) (2009) 16.
128. W. Khaliq and H.A. Khan, High temperature material properties of calcium aluminate cement concrete, *Constr. Build. Mater.* 94 (2015) 475–487.
129. N.P. Padture, M. Gell, and E.H. Jordan, Thermal barrier coatings for gas-turbine engine applications, *Science (80-.).* 296 (5566) (2002) 280–284.
130. W.D. Kingery, Factors affecting thermal stress resistance of ceramic materials, *J. Am. Ceram. Soc.* 38 (1) (1955) 3–15.
131. D.P.H. Hasselman, Elastic energy at fracture and surface energy as design criteria for thermal shock, *J. Am. Ceram. Soc.* 46 (11) (1963) 535–540.
132. D.P.H. Hasselman, Unified theory of thermal shock fracture initiation and crack propagation in brittle ceramics, *J. Am. Ceram. Soc.* 52 (11) (1969) 600–604.
133. J. Nakayama and M. Ishizuka, Experimental evidence for thermal shock damage resistance, *Am. Ceram. Soc. Bull.* 45 (7) (1966) 666.
134. T.J. Lu and N.A. Fleck, The thermal shock resistance of solids, *Acta Mater.* 46 (13) (1998) 4755–4768.
135. M.I.K. Collin and D.J. Rowcliffe, Influence of Thermal Conductivity and Fracture Toughness on the Thermal Shock Resistance of Alumina—Silicon–Carbide–Whisker Composites, *J. Am. Ceram. Soc.* 84 (6) (2001) 1334–1340.
136. H.-A. Bahr, G. Fischer, and H.-J. Weiss, Thermal-shock crack patterns explained by single and multiple crack propagation, *J. Mater. Sci.* 21 (8) (1986) 2716–2720.
137. H.-A. Bahr et al., Fracture analysis of a single edge cracked strip under thermal shock, *Theor. Appl. Fract. Mech.* 8 (1) (1987) 33–39.
138. D.R. Jenkins, Optimal spacing and penetration of cracks in a shrinking slab, *Phys. Rev. E* 71 (5) (2005) 56117.
139. B. Bourdin, G.A. Francfort, and J.-J. Marigo, The variational approach to fracture, *J. Elast.* 91 (1–3) (2008) 5–148.
140. A. Combescure, R. de Borst, and T. Belytschko, Symposium on Discretization Methods for Evolving Discontinuities, (n.d.).
141. H. Le Doussal et al., Comportement des produits refractaires soumis a des solicitations thermomechanique severes, *Bull. Soc. Fr. Ceram* (124) (1979) 29–55.
142. M.J. Heap et al., The influence of thermal-stressing (up to 1000 C) on the physical, mechanical, and chemical properties of siliceous-aggregate, high-strength concrete, *Constr. Build. Mater.* 42 (2013) 248–265.
143. K. Sakr and E. El-Hakim, Effect of high temperature or fire on heavy weight concrete properties, *Cem. Concr. Res.* 35 (3) (2005) 590–596.
144. M.H.B. Nasseri, A. Schubnel, and R.P. Young, Coupled evolutions of fracture toughness and elastic wave velocities at high crack density in thermally treated Westerly granite, *Int. J. Rock Mech. Min. Sci.* 44 (4) (2007) 601–616.
145. X.-T. Feng, S. Chen, and H. Zhou, Real-time computerized tomography (CT) experiments on sandstone damage evolution during triaxial compression with chemical corrosion, *Int. J. Rock Mech. Min. Sci.* 41 (2) (2004) 181–192.

146. S. Huang and K. Xia, Effect of heat-treatment on the dynamic compressive strength of Longyou sandstone, *Eng. Geol.* 191 (2015) 1–7.
147. J. Otani, T. Mukunoki, and Y. Obara, Application of X-ray CT method for characterization of failure in soils, *Soils Found.* 40 (2) (2000) 111–118.
148. S. Huang, K. Xia, and H. Zheng, Observation of microscopic damage accumulation in brittle solids subjected to dynamic compressive loading, *Rev. Sci. Instrum.* 84 (9) (2013) 93903.
149. S. Huang et al., An experimental study of the rate dependence of tensile strength softening of Longyou sandstone, *Rock Mech. Rock Eng.* 43 (6) (2010) 677–683.
150. Y. Xu et al., Influence of PFA on cracking of concrete and cement paste after exposure to high temperatures, *Cem. Concr. Res.* 33 (12) (2003) 2009–2016.
151. M.S. Morsy et al., Behavior of blended cement mortars containing nano-metakaolin at elevated temperatures, *Constr. Build. Mater.* 35 (2012) 900–905.
152. C.F. Revelo and H.A. Colorado, 3D printing of kaolinite clay ceramics using the Direct Ink Writing (DIW) technique, *Ceram. Int.* (2017).
153. M.C.A. Teles et al., Fique Fiber Tensile Elastic Modulus Dependence with Diameter Using the Weibull Statistical Analysis, *Mater. Res.* 18 (2015) 193–199.
154. M.F. Gazulla et al., Physico-chemical characterisation of silicon carbide refractories, *J. Eur. Ceram. Soc.* 26 (15) (2006) 3451–3458.
155. L. Fernández-Carrasco and T. Vázquez, Aplicación de la espectroscopia infrarroja al estudio de cemento aluminoso, *Mater. Construcción* 46 (241) (1996) 39–51.
156. H.A. Colorado, H.T. Hahn, and C. Hiel, Pultruded glass fiber-and pultruded carbon fiber-reinforced chemically bonded phosphate ceramics, *J. Compos. Mater.* 45 (23) (2011) 2391–2399.
157. H.A. Colorado, C. Hiel, and J. Yang, Different Fibers Exposed to Temperatures Up to 1000° C, *Mech. Prop. Perform. Eng. Ceram. Compos. VIII* (2014) 123–135.
158. M.R. Nilforoushan and N. Talebiaan, The hydration products of a refractory calcium aluminate cement at low temperatures, (2007).
159. C.M. George, Industrial Aluminous Cements in: Structure and performance of cements, S 415 ff; edited by P Barnes, (1983).
160. B. Singh and A.J. Majumdar, The hydration of calcium dialuminate and its mixtures containing slag, *Cem. Concr. Res.* 22 (6) (1992) 1019–1026.
161. S. Fujita et al., Synthesis of hydrogarnet from molten slag and its hydrogen chloride fixation performance at high temperature, *J. Mater. Cycles Waste Manag.* 4 (1) (2002) 70–76.
162. G. Le Saoût et al., Hydration of calcium aluminate cement blended with anhydrite, *Adv. Cem. Res.* 30 (1) (2018) 24–36.
163. C. Gosselin, Microstructural development of calcium aluminate cement based systems with and without supplementary cementitious materials, (2009).
164. T. Matusinović, N. Vrbos, and J. Šipušić, Rapid setting and hardening calcium aluminate cement materials, *Zement-Kalk-Gips Int.* 58 (5) (2005) 72–79.
165. B. Pacewska and M. Nowacka, Studies of conversion progress of calcium aluminate cement hydrates by thermal analysis method, *J. Therm. Anal. Calorim.* 117 (2) (2014) 653–660.
166. N. Ukrainczyk, Effect of polycarboxylate superplasticiser on properties of calcium aluminate cement mortar, *Adv. Cem. Res.* 27 (7) (2015) 388.
167. E. Sakai et al., Mechanical properties and micro-structures of calcium aluminate based

ultra high strength cement, *Cem. Concr. Res.* 40 (6) (2010) 966–970.
168. M.A. Rodríguez et al., Estudio por difracción de rayos X de la hidratación de mezclas de CaAl2O4-Humo de silice, *Boletín La Soc. Española Cerámica y Vidr.* 46 (6) (2007) 280–288.
169. J.M.R. Mercury et al., Calcium aluminates hydration in presence of amorphous SiO2 at temperatures below 90 C, *J. Solid State Chem.* 179 (10) (2006) 2988–2997.
170. A. Hidalgo López et al., Microstructural Evolution of Calcium Aluminate Cements Hydration with Silica Fume and Fly Ash Additions by Scanning Electron Microscopy, and Mid and Near-Infrared Spectroscopy, *J. Am. Ceram. Soc.* 91 (4) (2008) 1258–1265.
171. A. Hidalgo et al., Microstructure of the system calcium aluminate cement-silica fume: application in waste immobilization, *in* Stud. Surf. Sci. Catal., *Elsevier*, (2007): pp. 1617–1628.
172. A.J. Majumdar, R.N. Edmonds, and B. Singh, Hydration of Secar 71 aluminous cement in presence of granulated blast furnace slag, *Cem. Concr. Res.* 20 (1) (1990) 7–14.
173. M. Collepardi, S. Monosi, and P. Piccioli, The influence of pozzolanic materials on the mechanical stability of aluminous cement, *Cem. Concr. Res.* 25 (5) (1995) 961–968.
174. H.M. Son et al., Effect of nano-silica on hydration and conversion of calcium aluminate cement, *Constr. Build. Mater.* 169 (2018) 819–825.
175. J.F. Zapata, M. Gomez, and H.A. Colorado, High Temperature Cracking Damage of Calcium Aluminate Cements, *in* TMS Annu. Meet. Exhib., *Springer*, (2018): pp. 553–563.
176. J.F. Zapata, M. Gomez, and H.A. Colorado, Calcium Aluminate Cements Subject to High Temperature, *Adv. Mater. Sci. Environ. Energy Technol. VI* 262 (2017) 97.
177. K.D. Hertz, Concrete strength for fire safety design, *Mag. Concr. Res.* 57 (8) (2005) 445–453.
178. L. Bodnarova et al., Effect of high temperatures on cement composite materials in concrete structures, *Acta Geodyn. Geomater.* 10 (2) (2013) 173–180.
179. et al. K. Baltakys, The influence of different additives on the early-stage hydration of calcium aluminate cement, *J. Therm. Anal. Calorim.* 134 (2018) 89.
180. M.U. Okoronkwo and F.P. Glasser, Stability of strätlingite in the CASH system, *Mater. Struct.* 49 (10) (2016) 4305–4318.
181. B. Pacewska et al., Studies on the influence of spent FCC catalyst on hydration of calcium aluminate cements at ambient temperature, *J. Therm. Anal. Calorim.* 105 (1) (2011) 129–140.
182. D.E. Cox and R.J. Papoular, Structure Refinement with Synchrtron Data: R-Factors, Errors and Significance Tests, *in* Mater. Sci. Forum, *Trans Tech Publ*, (1996): pp. 233–238.
183. Ş. Marincea et al., Gehlenite from three occurrences of high-temperature skarns, Romania: new mineralogical data, *Can. Mineral.* 49 (4) (2011) 1001–1014.
184. M.U. Okoronkwo and F.P. Glasser, Strätlingite: compatibility with sulfate and carbonate cement phases, *Mater. Struct.* 49 (9) (2016) 3569–3577.
185. V.C. Farmer, *Infrared spectra of minerals*, *Mineralogical society*, (1974).
186. J.A. Gadsden, *Infrared spectra of minerals and related inorganic c ompounds*, *Butterworths*, (1975).

187. R.L. Frost et al., Dehydroxylation and structure of alumina gels prepared from trisecbutoxyaluminium, *Thermochim. Acta* 329 (1) (1999) 47–56.
188. A. Hidalgo et al., Microstructural changes induced in Portland cement-based materials due to natural and supercritical carbonation, *J. Mater. Sci.* 43 (9) (2008) 3101–3111.
189. G. Renaudin, M. Francois, and O. Evrard, Order and disorder in the lamellar hydrated tetracalcium monocarboaluminate compound, *Cem. Concr. Res.* 29 (1) (1999) 63–69.
190. M.A. Trezza and A.E. Lavat, Analysis of the system 3CaO· Al2O3–CaSO4· 2H2O–CaCO3–H2O by FT-IR spectroscopy, *Cem. Concr. Res.* 31 (6) (2001) 869–872.
191. J.F. Zapata, M. Gomezc, and H.A. Colorado, Characterization of two calcium aluminate cement pastes, *Adv. High Temp. Ceram. Matrix Compo Sites Mater. Sustain. Dev. Ceram. Trans. Vol. CCLXIII* 263 (2017) 491–503.
192. D.M. Joseph, M. Devi, and S. Senthilkumar, Experimental Investigation of concrete with combined high alumina cement, silica fume and M-sand, *Int. J. Eng. Res. Appl.* 3 (2013) 425–428.
193. F. Wang et al., Effect of Colloidal Silica on the Hydration Behavior of Calcium Aluminate Cement, *Materials (Basel).* 11 (10) (2018) 1849.
194. H.L. Thi et al., Effects of silicafume and fly ash on properties of alumina cement, *in* MATEC Web Conf., *EDP Sciences*, (2018): p. 1015.
195. M. Zahedi, A.K. Ray, and D.S. Barratt, Preparation and crystallization of sol–gel C12A7 thin films, *J. Phys. D. Appl. Phys.* 41 (3) (2008) 35404.
196. D. Fumo, Effect of silica fume additions on the hydration behaviour of calcium aluminates, *in* UNITECR'97. Proc. Unified Int. Tech. Conf. Refract. 5 Th Bienn. Worldw. Congr. Refract. A Worldw. Technol., (1997): pp. 1325–1333.
197. C. Parr et al., Interactions between Silica Fume and CAC and Methods to Optimise Castable Placing Properties, *Refractories(Tokyo)* 58 (11) (2006) 622–623.
198. A. Authier, Dynamical theory of X-ray diffraction, *Int. Tables Crystallogr.* (2006) 626–646.
199. C. Suryanarayana and M.G. Norton, *X-ray diffraction: a practical approach*, *Springer Science & Business Media*, (2013).
200. B. Rajesh Kumar and B. Hymavathi, X-ray peak profile analysis of solid-state sintered alumina doped zinc oxide ceramics by Williamson–Hall and size-strain plot methods, *J. Asian Ceram. Soc.* 5 (2) (2017) 94–103.
201. S.J. Schneider, Effect of Heat-Treatment on the Constitution and Mechanical Properties of Some Hydrated Aluminous Cements, *J. Am. Ceram. Soc.* 42 (4) (1959) 184–193.
202. M. Heikal, M.M. Radwan, and H.H.M. Darweesh, Hydration characteristics and durability of calcium aluminate cement containing some blended systems, *Silic. Ind. Ceram. Sci. Technol.* 70 (2005) 3–4.
203. V.S. Ramachandran, *Applications of differential thermal analysis in cement chemistry*, *Chemical Publishing Company New York*, (1969).
204. P.A. Barnes and J.H. Baxter, A critical analysis of the application of derivative thermogravimetry to the determination of the degree of conversion of high alumina cement, *Thermochim. Acta* 24 (2) (1978) 427–431.
205. D.E. Day and G. Lewis, Quantitative thermogravimetry of calcium aluminate compounds and cements after hydrothermal treatment, (1979).
206. H.G. Midgley, Measurement of high-alumina cement-calcium carbonate reactions using DTA, *Clay Miner.* 19 (5) (1984) 857–864.

207. S.M. Bushnell-Watson and J.H. Sharp, The detection of the carboaluminate phase in hydrated high alumina cements by differential thermal analysis, *Thermochim. Acta* 93 (1985) 613–616.
208. S.K. Das, A. Mitra, and P.K. Das Poddar, Thermal analysis of hydrated calcium aluminates, *J. Therm. Anal. Calorim.* 47 (3) (1996) 765–774.
209. N. Schmitt et al., Coupling between kinetics of dehydration, physical and mechanical behaviour for high alumina castable, *Cem. Concr. Res.* 30 (10) (2000) 1597–1607.
210. H. Fryda et al., Relevance of laboratory tests to field applications of calcium aluminate cement concretes, *in* Int. Conf. Calcium Aluminate Cem., (2001): pp. 227–246.
211. N.C. Collier, Transition and decomposition temperatures of cement phases–a collection of thermal analysis data, *Ceramics-Silikaty* 60 (4) (2016).
212. S.M. Bushnell-Watson and J.H. Sharp, The application of thermal analysis to the hydration and conversion reactions of calcium aluminate cements, *Mater. Construcción* 42 (228) (1992) 13–32.
213. S. Kwan, J. LaRosa, and M.W. Grutzeck, 29Si and 27Al MASNMR study of stratlingite, *J. Am. Ceram. Soc.* 78 (7) (1995) 1921–1926.
214. G.L. Kalousek, C.W. Davis, and W.E. Schmertz, An investigation of hydrating cements and related hydrous solids by differential thermal analysis, *in* J. Proc., (1949): pp. 693–712.
215. E. Passaglia and R. Rinaldi, Katoite, a new member of the Ca3Al2 (SiO4) 3-Ca3Al2 (OH) 12 series and a new nomenclature for the hydrogrossular group of minerals, *Bull. Minéralogie* 107 (5) (1984) 605–618.
216. R.S. Alwitt, Oxides and oxide films, *New York* 4 (1976) 169–254.
217. R.C. Mackenzie, The oxides of iron, aluminium, and manganese: p 299-328 in The differential thermal investigation of clays, *Miner. Soc., London* (1957).
218. B. Lothenbach, L. Pelletier-Chaignat, and F. Winnefeld, Stability in the system CaO–Al2O3–H2O, *Cem. Concr. Res.* 42 (12) (2012) 1621–1634.
219. S.M. Park et al., Stable conversion of metastable hydrates in calcium aluminate cement by early carbonation curing, *J. CO2 Util.* 21 (2017) 224–226.
220. A.B. Tchamba et al., Use of bauxite from Cameroon for solid state sintering and characterization of calcium dialuminate (CaO· 2Al2O3) refractory cement, *Ceram. Int.* 40 (1) (2014) 1961–1970.
221. D.A.S. Rambo et al., Calcium-aluminate mortars at high temperatures: Overcoming adverse conversion effects using clinker aggregates, *Cem. Concr. Compos.* 96 (2019) 212–224.
222. S. Maitra et al., Dehydration kinetics of calcium aluminate cement hydrate under non-isothermal conditions, *Ceram. Int.* 31 (3) (2005) 371–374.
223. B. Zhu, B. Fang, and X. Li, Dehydration reactions and kinetic parameters of gibbsite, *Ceram. Int.* 36 (8) (2010) 2493–2498.
224. D. Madej et al., Hydration of Ca7ZrAl6O18 phase, *Ceram. Int.* 38 (5) (2012) 3821–3827.
225. J.G. Griffin and K.E. Daugherty, The effect of temperature on the hydration of the calcium aluminates at high water-solid ratios, *Thermochim. Acta* 91 (1985) 53–60.
226. F.A. Cardoso et al., Drying behavior of hydratable alumina-bonded refractory castables, *J. Eur. Ceram. Soc.* 24 (5) (2004) 797–802.
227. A.M. Huntz et al., Thermal expansion coefficient of alumina films developed by oxidation of a FeCrAl alloy determined by a deflection technique, *Appl. Surf. Sci.* 252

(22) (2006) 7781–7787.
228. Y. Okada and Y. Tokumaru, Precise determination of lattice parameter and thermal expansion coefficient of silicon between 300 and 1500 K, *J. Appl. Phys.* 56 (2) (1984) 314–320.
229. R. Salomão et al., Mechanism of pore generation in calcium hexaluminate (CA6) ceramics formed in situ from calcined alumina and calcium carbonate aggregates, *J. Eur. Ceram. Soc.* 36 (16) (2016) 4225–4235.
230. D.A. Jerebtsov and G.G. Mikhailov, Phase diagram of CaO–Al2O3 system, *Ceram. Int.* 27 (1) (2001) 25–28.
231. B. Hallstedl, Assessment of the CaO-Al2O3 system, *J. Am. Ceram. Soc.* 73 (1) (1990) 15–23.
232. M.A. Chavda, H. Kinoshita, and J.L. Provis, Modification of a calcium aluminate cement system to prevent conversion to cubic hydrates and minimise corrosion of encapsulated aluminium metal, *in* 32nd Cem. Concr. Sci. Conf., (2012).
233. M. Duriez and J. Arrambide, Nouveau traité de matériaux de construction, (1961).
234. E.F. Osborn and A. Muan, Al2O3-CaO-SiO2 system revised and redrawn, *Phase Equilib. Diagrams Oxides Syst. LD Hart Ed. (Ed), Plate* 1 (1960).
235. M.-A. Maaroufi et al., Thermo-hydrous behavior of hardened cement paste based on calcium aluminate cement, *J. Eur. Ceram. Soc.* 35 (5) (2015) 1637–1646.
236. S. Quesnel, S. Afshar, and C. Allaire, *Corrosion of refractories at the bellyband of aluminum melting and holding furnaces, Minerals, Metals and Materials Society, Warrendale, PA (United States)*, (1996).
237. A. CAPMAS and T.A. BIER, Possibilities of special cements in ceramic applications, *Le J. Phys. IV* 03 (C7) (1993) C7-1341-C7-1346.
238. N.D. Chatterjee, W. Johannes, and H. Leistner, The system CaO-Al 2 O 3-SiO 2-H 2 O: new phase equilibria data, some calculated phase relations, and their petrological applications, *Contrib. to Mineral. Petrol.* 88 (1–2) (1984) 1–13.
239. H. Marzagui and T. Cutard, Characterisation of microstructural evolutions in refractory castables by in situ high temperature ESEM, *J. Mater. Process. Technol.* 155–156 (2004) 1474–1481.
240. H.L. Friedman, New methods for evaluating kinetic parameters from thermal analysis data, *J. Polym. Sci. Part B Polym. Lett.* 7 (1) (1969) 41–46.
241. M.S. Doulah, Determination of kinetic parameters by thermoanalytical techniques, *Thermochim. Acta* 35 (2) (1980) 263–265.
242. M.S. Doulah, A method for the determination of kinetic parameters by DTA, *Thermochim. Acta* 42 (3) (1980) 373–375.
243. J.F. Zapata, M. Gomez, and H.A. Colorado, Cracking in Calcium Aluminate Cement Pastes Induced at Different Exposure Temperatures, *J. Mater. Eng. Perform.* 28 (12) (2019) 7502–7513.
244. S. Bentsen, Effect of microsilica on conversion of high alumina cement, *Calcium Aluminate Cem.* (1990).
245. S. Moehmel et al., The influence of microsilica on the course of hydration of monocalcium aluminate, *in* Int. Conf. Calcium Aluminate Cem., (2001): pp. 319–330.
246. T.A. Bier et al., The roles of fine silica and reactive alumina and their interactions with calcium aluminates in refractory castables, *TARJ, Japan* (1998).
247. J. Ding, Y. Fu, and J.J. Beaudoin, Strätlingite formation in high alumina cement-silica fume systems: significance of sodium ions, *Cem. Concr. Res.* 25 (6) (1995) 1311–

1319.
248. Y. Fu, F. Ding, and J.J. Beaudoin, Temperature dependence of compressive strength of conversion-inhibited high alumina cement concrete, *Mater. J.* 94 (6) (1997) 540–545.
249. F.R. Larson, A time temperature relationship for rupture and creep stress, *Trans. ASME* (1952) 765–775.
250. J.E. Dorn, Some fundamental experiments on high temperature creep, *J. Mech. Phys. Solids* 3 (2) (1955) 85–116.
251. S.S. Manson and A.M. Haferd, A linear time-temperature relation for extrapolation of creep and stress-rupture data, (1953).
252. R.W. Evans, J.D. Parker, and B. Wilshire, Recent advances in creep and fracture of engineering materials and structures, *Pineridge Press. Swansea, 1982) P* 135 (1982).
253. R.W. Evans and B. Wilshire, Creep of metals and alloys, (1985).
254. A.G.T. Martinez et al., Creep behavior modeling of silica fume containing Al2O3–MgO refractory castables, *Ceram. Int.* 38 (1) (2012) 327–332.
255. R.W. Evans, T. Murakami, and B. Wilshire, Rate controlling processes during creep of silicon nitride ceramics, *Br. Ceram. Trans. J.* 87 (2) (1988) 54–57.
256. R.W. Evans, P.J. Scharning, and B. Wilshire, Constitutive equations for creep of a fired doloma refractory, *Br. Ceram. Trans. J.* 85 (2) (1986) 63–65.
257. R.W. Evans and B. Wilshire, The theta approach to creep of structural ceramics, *Rev. Powder Metall. Phys. Ceram.* 5 (2) (1992) 111–168.
258. A.H. Chokshi and T.G. Langdon, Characteristics of creep deformation in ceramics, *Mater. Sci. Technol.* 7 (7) (1991) 577–584.
259. R. Raj and C.K. Chyung, Solution-precipitation creep in glass ceramics, *Acta Metall.* 29 (1) (1981) 159–166.
260. S.M. WIEDERHORN et al., Damage-enhanced creep in a siliconized silicon carbide: phenomenology, *J. Am. Ceram. Soc.* 71 (7) (1988) 602–608.
261. A. Crosby and P.E. Evans, Creep in non-ductile ceramics, *J. Mater. Sci.* 8 (12) (1973) 1759–1764.
262. A.H. Chokshi, An analysis of creep deformation in nanocrystalline materials, *Scr. Mater.* 34 (12) (1996) 1905–1910.
263. F.R.N. Nabarro, Report of a Conference on the Strength of Solids, *Phys. Soc. London* 75 (1948).
264. C. Herring, Diffusional viscosity of a polycrystalline solid, *J. Appl. Phys.* 21 (5) (1950) 437–445.
265. R.L. Coble, A model for boundary diffusion controlled creep in polycrystalline materials, *J. Appl. Phys.* 34 (6) (1963) 1679–1682.
266. T.G. Langdon, A unified approach to grain boundary sliding in creep and superplasticity, *Acta Metall. Mater.* 42 (7) (1994) 2437–2443.
267. T.G. Langdon, Identifiying creep mechanisms at low stresses, *Mater. Sci. Eng. A* 283 (1–2) (2000) 266–273.
268. A.H. Chokshi, Diffusion creep in oxide ceramics, *J. Eur. Ceram. Soc.* 22 (14–15) (2002) 2469–2478.
269. I.M. Lifshitz, On the theory of diffusion-viscous flow of polycrystalline bodies, *Sov. Phys. JETP* 17 (1963) 909–920.
270. W.A. Rachinger, Relative grain translations in the plastic flow of aluminium, *J. Inst. Met.* 81 (1952).

271. K.A. Padmanabhan and H. Gleiter, Optimal structural superplasticity in metals and ceramics of microcrystalline-and nanocrystalline-grain sizes, *Mater. Sci. Eng. A* 381 (1–2) (2004) 28–38.
272. H. Conrad and J. Narayan, On the grain size softening in nanocrystalline materials, *Scr. Mater.* 11 (42) (2000) 1025–1030.
273. D. Gómez-García et al., Diffusion-driven superplasticity in ceramics: modeling and comparison with available data, *Phys. Rev. B* 80 (21) (2009) 214107.
274. T.G. Langdon, Grain boundary sliding as a deformation mechanism during creep, *Philos. Mag.* 22 (178) (1970) 689–700.
275. B. Burton, Interface reaction controlled diffusional creep: a consideration of grain boundary dislocation climb sources, *Mater. Sci. Eng.* 10 (1972) 9–14.
276. A.H. Heuer, N.J. Tighe, and R.M. Cannon, Plastic Deformation of Fine-Grained Alumina (Al2O3): II, Basal Slip and Nonaccommodated Grain-Boundary Sliding, *J. Am. Ceram. Soc.* 63 (1-2) (1980) 53–58.
277. A. Ball and M.M. Hutchison, Superplasticity in the aluminium–zinc eutectoid, *Met. Sci. J.* 3 (1) (1969) 1–7.
278. Y.T. Zhu and T.G. Langdon, Influence of grain size on deformation mechanisms: An extension to nanocrystalline materials, *Mater. Sci. Eng. A* 409 (1–2) (2005) 234–242.
279. S. Ghosh and A.H. Chokshi, Creep in nanocrystalline zirconia, *Scr. Mater.* 86 (2014) 13–16.
280. R. Korla and A.H. Chokshi, A constitutive equation for grain boundary sliding: an experimental approach, *Metall. Mater. Trans. A* 45 (2) (2014) 698–708.
281. H.S. Kim, Y. Estrin, and M.B. Bush, Plastic deformation behaviour of fine-grained materials, *Acta Mater.* 48 (2) (2000) 493–504.
282. V.W. Nehring, J.R. Smyth, and T.D. McGEE, Compressive creep of CoO single crystals, *J. Am. Ceram. Soc.* 60 (7-8) (1977) 328–332.
283. A.K. Mukherjee, The rate controlling mechanism in superplasticity, *Mater. Sci. Eng.* 8 (2) (1971) 83–89.
284. P.S. Roodposhti et al., Grain boundary sliding mechanism during high temperature deformation of AZ31 Magnesium alloy, *Mater. Sci. Eng. A* 669 (2016) 171–177.
285. R.W. Evans and B. Wilshire, Power law creep of polycrystalline copper, *Creep Fract. Eng. Mater. Struct.* (1987) 59–70.
286. R.W. Evans, A constitutive model for the high-temperature creep of particle-hardened alloys based on the? projection method, *in* Proc. R. Soc. London A Math. Phys. Eng. Sci., *The Royal Society*, (2000): pp. 835–868.
287. A. Baldan and E. Tascioglu, Assessment of θ-projection concept and fracture cavitation, *J. Mater. Sci.* 43 (13) (2008) 4592–4606.
288. J. Pelleg, Creep in Ceramics, *in* Creep Ceram., *Springer*, (2017): pp. 41–61.
289. C.H. Hsueh and A.G. Evans, Creep fracture in ceramic polycrystals—II Effects of inhomogeneity on creep rupture, *in* Perspect. Creep Fract., *Elsevier*, (1983): pp. 133–143.
290. J.R. Porter, W. Blumenthal, and A.G. Evans, Creep Fracture in Ceramic Polycrystals—I Creep Cavitation Effects in Polycrystalline Alumina, *in* Perspect. Creep Fract., *Elsevier*, (1983): pp. 125–132.
291. M.D. Thouless, C.H. Hsueh, and A.G. Evans, A damage model of creep crack growth in polycrystals, *Acta Metall.* 31 (10) (1983) 1675–1687.
292. S.I. Warshaw and F.H. NORTON, Deformation behavior of polycrystalline aluminum

oxide, *J. Am. Ceram. Soc.* 45 (10) (1962) 479–486.
293. J. Rösler, H. Harders, and M. Bäker, *Mechanical behaviour of engineering materials: metals, ceramics, polymers, and composites, Springer Science & Business Media*, (2007).
294. R. Raj and M.F. Ashby, On grain boundary sliding and diffusional creep, *Metall. Trans.* 2 (4) (1971) 1113–1127.
295. B. Walkley and J.L. Provis, Solid-state nuclear magnetic resonance spectroscopy of cements, *Mater. Today Adv.* 1 (2019) 100007.
296. D. Redaoui et al., Mechanism and kinetic parameters of the thermal decomposition of gibbsite Al (OH) 3 by thermogravimetric analysis, *Acta Phys. Pol. A* 131 (2017) 562–565.
297. J. Šesták, Ignoring heat inertia impairs accuracy of determination of activation energy in thermal analysis, *Int. J. Chem. Kinet.* 51 (1) (2019) 74–80.
298. T. Ondro, T. Húlan, and I. Vitázek, Non-isothermal kinetic analysis of the dehydroxylation of kaolinite in dynamic air atmosphere, *Acta Technol. Agric.* 20 (2) (2017) 52–56.
299. A. Al Rashid et al., Additive manufacturing: Technology, applications, markets, and opportunities for the built environment, *Autom. Constr.* 118 (2020) 103268.
300. J. Savolainen and M. Collan, How Additive Manufacturing Technology Changes Business Models?–Review of Literature, *Addit. Manuf.* 32 (2020) 101070.
301. J.P. Oliveira, T.G. Santos, and R.M. Miranda, Revisiting fundamental welding concepts to improve additive manufacturing: From theory to practice, *Prog. Mater. Sci.* 107 (2020) 100590.
302. B. Šavija and M. Luković, Carbonation of cement paste: Understanding, challenges, and opportunities, *Constr. Build. Mater.* 117 (2016) 285–301.
303. W. Ashraf, Carbonation of cement-based materials: challenges and opportunities, *Constr. Build. Mater.* 120 (2016) 558–570.
304. G.H.D. Tonoli et al., Effect of accelerated carbonation on cementitious roofing tiles reinforced with lignocellulosic fibre, *Constr. Build. Mater.* 24 (2) (2010) 193–201.